Behrouz Adibimanesh, M.Sc. Eng.

Institute of Fluid-Flow Machinery
Polish Academy of Sciences

Mathematical and data-driven modeling of biomass conversion for energy optimization

A dissertation submitted to the Scientific Board
of the Institute of Fluid-Flow Machinery, Polish Academy of Sciences
in partial fulfillment of the requirements
for the Degree of Doctor of Philosophy

Supervisor:
Sylwia Polesek-Karczewska, D.Sc. Ph.D. Eng.

Gdańsk, September 2025

Dedication to my family

I would like to dedicate this work to my family, whose love, support, and guidance have always been my greatest source of strength.

First and foremost, to my father, whose recent passing has left the deepest pain in my life. His constant support and the joy he found in my achievements were my strongest motivations. I carry his advice and encouragement with me in every step of this journey.

To my mother, the kindest and most loving person I know, whose pride in me has always been a quiet but powerful force. Her care and kindness have been my comfort through every challenge.

To my brothers, who have looked after my family during my time abroad, allowing me to focus on my work with peace of mind. Your help and responsibility have been invaluable.

To my wife's family, whose support and kindness have always surrounded us, giving strength to our family in so many ways.

To my son **Adrian**, who has been a true source of energy and strength, helping me overcome the challenges of this journey, and to my soon-to-arrive daughter, the sweetest part of this educational path. You both inspire me to give my best in every part of life.

And above all, to my beloved wife **Bahar**, whose love, patience, and strength have carried me through this journey. Without her, it would not have been possible to reach this point.

Acknowledgements

I would like to express my deepest gratitude to my supervisor, **Professor Sylwia Polesek-Karczewska**, for her guidance, support, and patience throughout this research. She was not only a supervisor but also a source of encouragement in many aspects of my life.

I am grateful to the **Institute of Fluid-Flow Machinery** for providing excellent research facilities and support. I would especially like to thank **Prof. Dariusz Kardaś**, Head of the Flow and Combustion Centre, and the Renewable Energy Department, for his support and hospitality during my studies. I am also very thankful to **Dr. Izabela Wardach-Święcicka** for her guidance and valuable comments on my pyrolysis simulations, which greatly improved my thesis. My sincere thanks also go to my friend **Paulina Hercel**, our daily discussions were not only helpful for my research but also made this journey more enjoyable. I would also like to extend my thanks to all my colleagues in the department for their support.

I would like to acknowledge the **SYDSEN group at the Karlsruhe Institute of Technology**, where I was supported by the **Helmholtz Visiting Researcher Grant** to conduct part of my research in Germany. I am especially thankful to **Prof. Dr. Sanja Lazarova-Molnar**, Head of the group, for her guidance in dynamic system modeling and for her generous support during my stay at KIT.

Finally, I would like to thank the **Doctoral School of Gdańsk University of Technology** for giving me the opportunity to attend courses and for partially supporting my research through the **STER Project** funded by the **National Science Centre**.

Contents

List of Symbols

AFR	air-to-fuel ratio
A	pre-exponential factor, 1/s
c_p	specific heat, J/(kg K)
E_a	activation energy J/mol
h	specific enthalpy J/kg
$\vec{F}$	force kg m/s^2
HHV	higher heating value J/kg
K	permeability, m^2
L	length, m
$\dot{m}$	mass flow rate, kg/s
m_p	particle mass, kg
MAE	mean absolute error
MSE	mean squared error
n	number of moles
p	pressure, Pa
$\dot{Q}$	thermal energy, W
$\dot{q}$	heat flux, W/m^2
t	time, s
T	temperature, K
$\dot{W}$	volumetric mass source, W/(m^3 s)
v	velocity, m/s
V	volume, m^3
v_0	particle feed velocity, mm/s
r_p	particle radius, m
d_p	particle diameter, m
V_p	particle volume, m^3
Y_j	mass fraction of j-th specie (H_2O, H_2, CH_4, CO, CO_2)
k_p	pyrolysis rate constant, 1/s
Z	mass loss rate, $Z = m_s/m_{s,0}$

Greek symbols

ε	volume fraction
η	learning rate
λ	thermal conductivity, W/(m K); excess-air ratio
μ	dynamic viscosity, kg/(m s)
σ	Stefan-Boltzmann constant, 5.67×10^{-8} W/(m^2 K^4)
$\langle \sigma_{ex} \rangle$	effective emissivity
ρ	density, kg/m^3

Subscripts/Superscripts

a	air
amb	ambient
ch	chemical
cond	conduction
d	dry
fg	flue gas
g	gas
i	i-th particle
in	inlet
mix	mixed
out	outlet
ox	oxidizer
r	recirculated
rad	radiation
s	solid
sg	solid to gas (devolatilization)
ss	sewage sludge
st	steam

Acronyms

AFE3	air flowrate (HEX2), m^3/hr
AFR	air-to-fuel ratio
ANN	artificial neural network
CFD	computational fluid dynamics
DCEL	dynamic coupled Eulerian-Lagrangian method
DEM	discrete element method
DRT	dryer residence time, hr
DT	digital twin

FC	fixed carbon
FT	feed temperature, °C
FTE1	fume temperature (HEX1), °C
GBM	gradient boosting machine
HEX	heat exchanger
ML	machine learning
RF	random forest
SS	sewage sludge
STD	steam inlet temperature to dryer
TFB	temperature in fluidized bed
VM	volatile matter
WHR	waste heat recovery
WWTP	wastewater treatment plant
XDEM	extended discrete element method

Abstract

The global transition towards sustainable energy systems necessitates the efficient thermal conversion of biomass and biogenic waste resources. Thermochemical processes like gasification and incineration are central to this effort, yet their inherent complexity, arising from coupled physical and chemical phenomena and their multiscale nature, presents a significant challenge for optimization. Mathematical modeling remains the primary support for the development of innovative, efficient technologies, complementing often costly and time-consuming experimental research. Traditional modeling approaches focus either on detailed component-level analysis or on system-level performance, creating a gap between fundamental understanding and operational application. This thesis thus aims to develop and demonstrate a holistic, multi-scale framework for the analysis, monitoring, and optimization of thermochemical conversion systems. This involves numerical modeling of particular heat and mass transfer processes in a reactive medium and machine learning algorithms for system performance predictions.

The research is structured around three interconnected pillars. First, to advance fundamental understanding at the component level, a novel in-house Dynamic Coupled Eulerian-Lagrangian (DCEL) method is developed to model particle-scale phenomena, including fuel grain shrinkage, heat transfer and gas release within a gasifier. Producer gas can serve as a fuel for direct use in thermal and power generation systems, and as a raw material for chemicals or other energy carriers, such as hydrogen or synthetic fuels. One of the crucial factors for the feedstock conversion degree and thereby the quality and yield of syngas is the fuel movement speed. Unlike one-dimensional Eulerian-type approaches usually applied to model small-scale fixed-bed reactors, the proposed DCEL model allows for determining the fuel bed movement variable along the reactor that results from the volume change of the devolatilizing particles. Thus, the investigation focuses on the dynamics of biomass decomposition, which is critical while considering the optimal technology pathway for the specific feedstock. The DCEL model's predictive capabilities and computational efficiency are qualitatively evaluated against the advanced eXtended Discrete Element Method (XDEM), and the predictions of both are compared with experimental data. Second, the scope is expanded to system-level analysis through the application of machine learning (ML) methods. A data-driven model of an industrial sewage sludge incineration plant is elaborated, integrating Aspen Plus simulations with ML algorithms, including Gradient Boosting

Machines and a novel chained-regression technique, to predict key performance indicators and identify optimal operating conditions for enhanced energy efficiency. Third, continuing the analysis of the incineration plant in terms of energy consumption optimization, the thesis culminates in the implementation of a real-time digital twin. This approach integrates physical models, analytical calculations, and operational data within a dynamic simulation environment (AnyLogic). This digital twin enables closed-loop energy optimization through smart scenario analysis, demonstrating a validated strategy that reduces the consumption of biogas serving as an auxiliary fuel by 40% while maintaining operational compliance.

The research work carried out provides a comprehensive framework that integrates advanced numerical modeling of complex transport processes in a solid fuel bed with data-driven analytics and digital twin technology. The findings demonstrate that such a multi-faceted approach is paramount for unlocking the full potential of complex energy systems, dedicated to the rational management of available biogenic fuel resources, which are difficult due to their physicochemical characteristics and diversity.

Streszczenie

Globalne przejście na zrównoważone systemy energetyczne wymaga efektywnej konwersji biomasy i zasobów odpadów biodegradowlanych. Procesy termochemiczne, takie jak zgazowanie i spalanie, są kluczowe dla tych działań, jednak ich inherentna złożoność, wynikająca ze sprzężonych zjawisk fizycznych i chemicznych oraz ich wieloskalowości, stanowi poważne wyzwanie dla optymalizacji. Modelowanie matematyczne pozostaje podstawowym wsparciem w zakresie rozwoju innowacyjnych efektywnych technologii, jako komplementarne do nierzadko kosztownych i czasochłonnych badań eksperymentalnych. Tradycyjne podejścia modelowe często koncentrują się albo na szczegółowej analizie samego urządzenia, albo na wydajności układu, tworząc lukę między fundamentalnym zrozumieniem a zastosowaniem operacyjnym. Celem pracy badawczej było opracowanie i przedstawienie holistycznych, wieloskalowych ram do analizy, monitorowania i optymalizacji systemów konwersji termochemicznej. Obejmują one numeryczne modelowanie szczegółowych zagadnień wymiany ciepła i masy w ośrodku reaktywnym oraz zastosowanie algorytmów uczenia maszynowego do przewidywania charakterystyki systemu.

Badania opierają się na trzech połączonych ze sobą filarach. Po pierwsze, aby poszerzyć fundamentalne rozumienie zjawisk na poziomie urządzenia jako komponentu systemu, opracowano nowatorską, własną sprzężoną metodę eulerowsko-lagranżowską (z ang. Dynamic Coupled Eulerian-Lagrangian (DCEL), do modelowania zjawisk fizykochemicznych w skali zbioru cząstek paliwa, z uwzględnieniem ich kurczenia się, wymiany ciepła i uwalniania gazu, wewnątrz zgazowarki. Syngas może być wykorzystywany bezpośrednio jako paliwo w układach produkcji ciepła i energii elektrycznej, jako surowiec do produkcji innych nosników energii, takich jak wodór oraz paliwa syntetyczne, jak również chemikaliów. Jednym z czynników istotnych dla stopnia konwersji paliwa, a zatem jakości i ilości generowanego gazu jest szybkość przesuwu paliwa. Zaproponowany model DCEL, w przeciwieństwie do jednowymiarowych modeli bazujących na podejściu eulerowskim, powszechniej stosowanych do modelowania małoskalowych reaktorów zgazowujących ze złożem paliwa, umożliwia określenie zmiennej wzdłuż reaktora prędkości przemieszczania się paliwa, powiązanej ze zmienną objętością odgazowujących cząstek. Tym samym, badania koncentrują się na dynamice rozkładu biomasy, która ma kluczowe znaczenie przy rozważaniu optymalnej ścieżki technologicznej dla konkretnego surowca. Zdolności predykcyjne i wydajność obliczeniową metody porównano jakościowo z bardziej zaawansowaną metodą, tak zwaną eXtended Discrete Element

Method (XDEM), a ich przewidywania porównano z rezultatmi badań eksperymentalnych. Po drugie, zakres analizy poszerzono na poziom systemowy poprzez zastosowanie metod uczenia maszynowego (ML). Opracowano, oparty na danych, model przemysłowej instalacji spalania osadów ściekowych. Integruje on symulacje Aspen Plus z algorytmami ML, w tym algorytm wzmacniania gradientowego (z ang. Gradient Boosting) oraz nowatorską technikę regresji łańcuchowej, w celu przewidywania kluczowych wskaźników wydajności i identyfikacji optymalnych warunków pracy dla poprawy efektywności energetycznej instalacji. Po trzecie, kontynuując analizę spalarni osadu ściekowego pod kątem optymalizacji zużycia energii, praca obejmuje także wdrożenie cyfrowego bliźniaka (ang. digital twin), działającego w czasie rzeczywistym. Integruje on modele fizyczne, obliczenia analityczne oraz dane operacyjne w środowisku symulacji dynamicznej (AnyLogic). Cyfrowy bliźniak umożliwił optymalizację energetyczną układu w pętli zamkniętej poprzez analizę scenariuszy, pokazując zweryfikowaną strategię, która pozwala redukować zużycie paliwa wspomagającego w postaci biogazu o 40%, przy jednoczesnym utrzymaniu zgodności operacyjnej.

Niniejsza praca dostarcza kompleksowych ram, które integrują zaawansowane modelowanie numeryczne skomplikowanych procesów transportu w złożu paliwa stałego, z analityką opartą na danych oraz technologią cyfrowych bliźniaków. Uzyskane wyniki pokazują, że takie wieloaspektowe podejście jest niezbędne dla pełnego wykorzystania potencjału złożonych systemów energetycznych, dedykowanych do racjonalnego zagospodarowania dostępnych zasobów paliw biogenicznych, trudnych z uwagi na charakterystykę fizykochemiczną i jej zróżnicowanie.

Chapter 1

Introduction

1.1 Background and motivation

The global pursuit of renewable energy and carbon reduction has intensified the focus on efficient biomass conversion technologies. Heat and power production systems based on renewable solid fuels, including biogenic fuels, despite the rapid development of wind and solar energy systems, remain indispensable for stable energy generation and supply. Along with the adaptation of existing combined heat and power units to new generation, or lower quality, fuels, of interest are innovations in gasification and pyrolysis technologies, particularly in terms of enhancing producer gas purity and yield, and its targeted composition (e.g. hydrogen content). Gasification stands out as a pivotal process for transforming solid renewable feedstocks and waste materials into usable energy, offering a sustainable alternative to fossil fuels. However, the inherent complexity of thermochemical conversion systems, characterized by intricate multi-phase interactions and non-linear dynamics, presents significant challenges for design, optimization and control, particularly when upscaling the technology. Traditional modeling approaches often operate in isolation, either focusing on detailed internal reactor phenomena or on broader system-level efficiency, creating a gap between fundamental understanding and practical implementation. Intensively developed, more advanced, predictive methods, incorporating artificial intelligence and machine learning techniques, offer key support in modeling and forecasting conversion systems' performance. Given the potential of such approaches, this dissertation focuses on developing and applying a comprehensive framework that integrates advanced component modeling with system-wide simulation and data-driven optimization. By combining novel computational methods, machine learning, and real-time digital twin technology, this work provides new insights into biomass and waste conversion processes and delivers practical tools for enhancing the performance, efficiency, and sustainability of complex energy systems.

The urgent need to improve the efficiency and sustainability of energy systems is a primary driver of this research. Biomass and waste-derived fuels are crucial components of

the renewable energy mix, but their conversion in devices like gasifiers and incinerators is highly complex. These systems involve coupled heat, mass, and momentum transfer alongside complex chemical reactions, making them difficult to design, optimize, and control using conventional methods. The motivation for this work stems from the critical need to deepen our understanding of these internal processes while also developing intelligent tools for system-level operation. This dual challenge is addressed by advancing modeling techniques for reactive porous beds and by introducing innovative simulation and optimization frameworks. The goal is to move beyond traditional, often static, analysis and towards dynamic, intelligent systems that can adapt in real-time, thereby maximizing energy recovery from renewable resources, minimizing operational costs, and reducing environmental impact, ultimately contributing to a more circular and sustainable economy.

1.2 Thermal conversion – computational methods in process and system analysis

1.2.1 Numerical modeling of biomass gasification

Gasification is recognised as one of the most promising thermochemical conversion methods to replace fossil fuels, owing to its flexibility in terms of the technology itself, as well as the products to be obtained [1]. Offering conversion of available resources into useful solid, gaseous or liquid products [2], gasification is considered a vital component of combined modern energy generation systems, providing a good alternative to widely applied but less efficient direct combustion.

This process involves several key stages: drying to remove moisture, pyrolysis to decompose the biomass into volatiles, tar, and char, and subsequent gasification reactions where the char reacts with air or steam. Pyrolysis is the critical initial thermal decomposition step, as it dictates the release rate of volatiles and the properties of the remaining char, which in turn governs the efficiency of the entire downstream conversion process. Accurately modeling this intricate sequence, especially the dynamic pyrolysis front propagation and its interaction with the gas flow, is therefore fundamental to predicting overall gasifier performance and syngas composition.

Rising demand for sustainable energy solutions, involving the utilization of locally available biomass, and bringing additional benefits from reducing costs of transport and collection of biomass, drives interest in small-scale gasification systems, as well as other types of thermochemical conversion units, with the preferable capacity of up to 200 kW [3]. The efficiency of gasification, including the yield and quality of products, depends on several factors, such as raw material composition, its pretreatment, particle size, residence time, gasifying agent type, operating parameters (i.e. temperature and pressure) and the type of reactor [4]. The major factor to be accounted for in the technology performance, of crucial

importance for the end-use of generated syngas, is, besides the heating value, its purity in terms of undesired tar and particulate matter contents [5]. The impact of the aforementioned factors, along with others like biomass-to-catalyst ratios, has been under study in terms of optimizing gasification to obtain hydrogen-rich syngas, aiming at supporting the development of green hydrogen generation. Such technology still requires a comprehensive examination to become a sustainable biomass valorization pathway, facing the associated technical challenges, including ensuring its reliability while scaling up the systems from the pilot- to industrial-scale [6]. The key issue to be solved viewed here is the tar processing, involving the determination of biomass and catalytic gasification mechanisms and the development of efficient and low-cost catalysts [7]. Tending towards economically beneficial solutions, attention is also paid to waste heat recovery from industrial processes that can help in reducing high energy consumption and improving yield and hydrogen content of the syngas [8].

A wide range of gasifiers are available for biomass gasification, each differing in operating conditions and design. The fundamental gasifier technology employed in a slow-moving system is a fixed bed gasifier [9]. Covering both the downdraft and updraft types, it is said to be suitable for small-scale applications [10, 11], basically due to relatively simple construction and operation as compared, for instance, to the fluidized bed technology.

Despite all the advantages and benefits biomass gasification offers, the process analysis and development of an efficient gasifier is challenging due to the process complexity that comprises a number of interconnected physical and chemical phenomena. Experimental multi-parameter and multi-variate research on gasification would involve a great deal of time and expense. Thus, computer-aided process modeling remains the critical step in gaining in-depth knowledge about the phenomena occurring within the reactor and, ultimately, in technology development for reliable and cost-effective design and optimization [12]. It should, however, be noted that the accuracy of the predictions on the complex thermochemical conversion characteristics is always a question of model simplifications to be made to simulate physicochemical phenomena involved [13]. Therefore, given the outstanding process complexity and a large number of interconnected parameters to be accounted for, researchers always face the challenging decision of what factor may be neglected or roughly estimated, and which should be definitely included in the simulation to obtain reliable results [14].

Numerous researchers have investigated the intricate computer modeling of the gasification process in fixed-bed gasifiers. Apart from modeling approaches based on reaction kinetics that focus on the conversion mechanisms and others based on thermodynamic equilibrium focusing on operational parameters and independent of the reactor design [15], the commonly used technique is computational fluid dynamics (CFD). This type of numerical modeling solves a system of simultaneous equations for the conservation of mass, momentum, energy, and species within a discrete region of the gasifier, employing an Eulerian approach [16]. Through coupling heat and species transfer with the detailed hydrodynam-

ics in the granular-type medium along the gasifier, it is able to provide a picture of the dynamics of the conversion process and more accurate predictions of syngas generation rate and quality. Many examples of Euler-Lagrange modeling are reported to date in the literature. Amongst them a considerable number concern dense granular flows, such as in the fluidized beds. For instance, Oevermann et al. [17] simulated wood gasification in a bubbling fluidized bed reactor, solving two-dimensional Navier-Stokes equations for the gas phase as a continuum and incorporating Discrete Element Method (DEM) for modeling solid phase movement. The issue is that the tracking of individual particles, either by implementing Discrete Phase Model (DPM) or DEM, is computationally expensive. An alternative is a multiphase particle-in-cell (MP-PIC) method. It involves the tracking of a group of particles of similar properties, called the computational particle, instead of single particles, thereby allowing for a reduction in computing requirements. Simultaneously, it improves the accuracy of interparticle interactions in high-volume fraction flows, eliminating numerical diffusion and enabling the modeling of particle distributions with various sizes and densities. The method was first developed to simulate dense particle flow in one-dimensional (1D) approach [18], and later extended to to two-dimensional (2D) multiphase flow case [19] and a three-dimensional (3D) case [20], including fluidized bed coal gasification [21]. The method was also utilized in a 3D Eulerian–Lagrangian model for predicting the performance of the fluidized bed biomass gasification [22]. These extensions improved the ability to handle dense particle flows by mapping particle properties to an Eulerian grid and incorporating a subgrid particle normal stress model. However, a limitation of the approach is that it assumes the particle size remains constant throughout the process. More recently, Aziz et al. [23] performed CFD simulation using the particle-in-cell (PIC) approach to include interactions of mass, momentum and energy between the gas and solid particles, while investigating co-firing of biomass (palm kernel shell) and coal. In their study, particles were modeled separately as two discrete phase models. Following the proven reliability and acceptable level of simulation cost-efficiency of MP-PIC technique, recently, Sun et al. [24] developed a comprehensive reactive MP-PIC model to analyze biomass gasification in an air-blown bubbling fluidized bed gasifier, aiming at providing guidelines for design optimization of such devices.

Another option for simulating dense particle flow with multiple solid phases of specified particle size distributions is the hybrid Euler-Lagrange approach, proposed by Adamczyk et al. [25], who applied it for predicting the granular flow in a large-scale circulating fluidized bed boiler. The Euler-Lagrange technique served in this case to provide the data on flow characteristics to a 3D CFD simulation of the boiler with possibly low computational effort.

Relatively few works considering CFD Eulerian-Lagrangian type approaches are devoted to small-scale gasifiers. Hu et al. [26] carried out a CFD analysis of wood chip gasification inside a small gasifier incorporating a Lagrangian dispersed phase model to track each particle. Janajreh and Shrah [27] used a CFD tool with the discrete solid particle phase solved in a Lagrangian frame of reference to investigate wood chips gasification in a commercial

downdraft gasifier scaled for 10–20 kW, obtaining good agreement between simulation results and measurement data. Similarly, Kumar and Paul [28] developed a 2D numerical model for simulating gasification of rubber wood in a 20 kW downdraft reactor using the Eulerian-Lagrange approach, coupling CFD with DPM to model the flow of biomass particles. A comprehensive 2D numerical study based on the CFD-DPM was performed by Rodriguez-Alejandro et al. [29] for a pilot-scale downdraft fixed bed reactor fed by pine wood, and operated as a pyrolyzer, gasifier and combustor.

However, it should be noted that the aforementioned CFD-based Eulerian-Lagrangian simulation methods do not take into account the change in particle volume resulting from its thermal decomposition. CFD-DEM simulations of cold flow simulations may serve as effective tools for optimizing device geometry to enhance thermal efficiency, as demonstrated by Li et al. [30] and Gao et al. [31]. From a practical point of view, more interesting are simulations that take into account heat transfer between the phases. Wang et al. [32] investigated spherical particles undergoing chemical reactions using CFD-DEM approach to predict the pyrolysis process of various dry solid fuels in a fixed-bed reactor, employing the open-source code MFix [33]. While particles experienced mass loss during heating, radiative heat transfer was not accounted for in this study.

Rosser et al. [34] utilized STAR-CCM+ software for CFD-DEM simulations to analyze the impact of ore pellet moisture, heating, and ice formation on jamming events in a hopper above the furnace. Although unrelated to combustion processes, the authors incorporated an additional energy equation to calculate particle temperature changes due to external conditions. The four-way coupling method of CFD with DEM, known as the eXtended Discrete Element Method (XDEM), was developed by Peters et al. [35]. This in-house software predicts the behavior of solid fuel particles during thermal treatment, employing a mixed Lagrangian-Eulerian approach to model the movement of granular materials in an external fluid field. CFD, using the OpenFOAM source [36], combined with DEM, enables the prediction of solid fuel particle positions in the flow field, while the extended classic DEM, i.e. XDEM module, provides information about their thermal conversion and related structural changes. In this approach, each particle undergoes various thermodynamic transformations due to heat transfer from the surrounding gas, described by a set of transient 1D balance equations for mass, momentum, and energy, solved within the XDEM module [37, 38].

Despite their proven suitability and reliability, numerical modelling of transport phenomena within a real-scale unit, including fixed bed gasifier, by means of discrete methods, may appear non-attractive as a design and optimization computing tool, owing to its high computational cost. Homogeneous-type models that consider the bed as a multiphase continuous medium, wherein solid and fluid (gas and liquid) phases coexist, represent a competitive option for this purpose, satisfactory in terms of prediction accuracy and calculation efficiency. Due to the simplified description, they are required to be supplemented by empirical correlations [39] but have been successfully used to simulate biomass gasification in downdraft reactors [40, 41] and updraft reactors [42, 43].

The literature overview carried out shows that within the group of thermal and flow models in reactive granular beds with regard to small-scale fixed-bed reactors, developed to date, the majority are 1D Euler-type models. They are considered useful as computationally efficient methods amongst the integrated models incorporating transport phenomena and chemical kinetics. The quite recent studies provide comprehensive 1D mathematical descriptions under non-stationary conditions. These include the unsteady model for a downdraft biomass gasifier proposed by Patra et al. [44], developed to predict the variations of solid and gas temperature, gas velocity, wood and char density, gas generation rate and composition along the reactor. The performance of a reactor with a focus on the impact of equivalence ratio on the producer gas yield and composition, and the temperature distribution, under air-steam biomass gasification was studied by Sharma et al. [45]. Perez et al. [46] carried out a detailed numerical analysis of the co-current gasifier, e.g. heat transfer mechanisms and rates, depending on the model parameters and operating conditions. Their study showed that the most significant parameter affecting the process, basically the reaction front propagation, the feedstock consumption rate and the solid temperature, is the fuel particle size.

1.2.2 Machine learning methods in process optimization

Biomass is a popular fuel nowadays, particularly for heating and cooking uses in most developing countries. In many industrialized countries, the use of biomass fuels for electricity production and transportation is rising as a strategy to reduce carbon dioxide emissions from burning fossil fuels [47, 48]. The possible benefits from biomass utilization should however be assessed not only in terms of environmental impacts but also from the view of its local sustainability [49]. Rational and ecologically sound waste management is one of the key objectives of the European Green Deal targeted toward the full use of available renewable sources, including biodegradable waste materials, and reducing greenhouse gas emissions through, *inter alia*, decreasing the energy consumption of technological processes [50]. The choice of optimum route for thermochemical conversion of the specific biomass, as well as the optimization of the existing conversion systems, is, however, challenging due to the significant diversity of available biogenic resources and variability of their physicochemical properties. Amongst the troublesome aspects of the conversion of such materials in terms of energy consumption is the moisture content. One example is sewage sludge (SS). It is a biologically active wastewater processing residue made up of water (over 90% by weight), organic materials, e.g. dead and living microorganisms, and organic and inorganic pollutants such as polycyclic aromatic hydrocarbons (PAHs) and heavy metals [51]. With this, SS belongs to a subcategory of bio-waste, alongside organic by-products from industry and agriculture, such as poultry litter [52] and meat-and-bone meal [53], which require safe management. Since they have been recognized as alternative fuels that may contribute to sustainable development, a lot of efforts have been undertaken to improve their suitability

for energy generation [54, 55]. Of concern are mainly high contents of moisture and/or ash, but what is even more crucial is to assess in a systematic manner the possible risk of the presence of harmful organic pollutants and pathogens [56] that may eventually lead to air and soil contamination as a consequence of inappropriate disposal of these organic materials. Crucially, a global increasing tendency in the volumes of generated SS is observed. For instance, a maximum of over 50 million tonnes of SS produced annually with an expected 10% rise each year has been reported for China [57], whereas the projections for European Union (EU) have shown an increase in SS amounts up to 13 million tonnes (dry mass) in 2020 [58]. Poland is among those EU countries that generate the highest quantities of SS [59], with an amount exceeding 580 thousand tonnes (dry mass) per year (years 2017-2018) [60]. This leads to increasing concerns about taking care of SS management within the design process. The same applies to municipal solid waste that has been increasingly generated worldwide over the past decades. Its safe and sustainable management is also a question of conversion technology sustainability as regards the environmental impacts, and thereby the possible risk to the health of humans, as well as the economic and social aspects [61].

Large amounts of urban waste all around the world, which has been produced by human activities, have raised serious threats to healthcare and environmentally friendly organizations. Correspondingly, the treatment of wastewater has become a matter of concern for developed countries, such that high-income countries treated 70% of the generated wastewater on average according to the last available data [62]. The significance of the treatment process is highlighted since governmental and regional policies have been developed for wastewater treatment in various applications such as agriculture, industry, and aquaculture [63].

SS features considerable diversity of physicochemical properties [64], dependent on the area of generation, and amongst others, on the degree of its industrialization and the type of discharged industrial waste. Additionally, these properties also depend on the technological processes used in a wastewater treatment plant [65].

Gasification, featuring high flexibility as regards the feedstock properties, is considered, besides pyrolysis, one of the promising alternatives for effective SS conversion [66]. The majority of installations, both pilot and commercial scale, are based on fixed bed and fluidized bed reactors, supporting the self-sufficiency of wastewater treatment plants through combined heat and power production, including covering the energy consumption for sludge drying [67].

Still, incineration, although less sensitive to the feedstock composition change, is the most commonly used protocol for utilization of SS in Poland and other countries, even though proven to be the most expensive one [68]. As a possible option to be implemented, incineration was also thoroughly analyzed, including the technical and economic appraisal, for the case study of Italy for which far lower amounts of incinerated sludge (about 2% of the total sludge generated) compared to other EU countries (e.g. an average of several percent

of the total sludge generated) are reported [69]. The major benefits of this technology are the reduction of waste volume while eliminating pathogens and organic pollutants, as well as the possibility of heat and power generation [70] that may contribute to the self-sufficiency of a wastewater treatment plant. However, the efficiency of the SS thermal treatment process is to a large extent determined by dewatering, specifically the drying of dewatered sludge.

Like in the case of pyrolysis or gasification, sewage sludge requires pre-drying to reduce the water content to ensure the autothermal combustion without additional support. In the case of fluidized bed burning, which is the most preferable way for wet SS [71], the moisture content should be at the maximum level of 60%wt. Thus, drying as an energy-intensive process, along with flue gas cleaning, accounts for a significant part of the high costs of SS incineration. Therefore, it should be considered while optimizing sludge treatment.

The lack of sufficient and accurate information on the energy performance of various feedstock impedes more extensive scale implementations of the SS incineration systems. Therefore, the need for new intelligent technologies is inevitable to compensate for the insufficient information for data analysis purposes. Applications of several emerging technologies have gotten more widespread as information technologies advance at a rapid pace [72, 73]. Among those techniques, machine learning (ML) has shown its potential for various industrial applications [74, 75]. By employing reliable data-rich frameworks, ML models could learn hidden patterns while uncovering covert knowledge in order to make a decision, in terms of process optimization and system progression in different fields. ML models have also been applied to overcome the challenges in SS treatment plants in an extensive number of research studies. For instance, a comparative study was carried out to predict the long-term energy consumption of the Melbourne East wastewater treatment plants with artificial neural network (ANN), Gradient Boosting Regression (GBM), and RF algorithms. It is revealed that the GBM technique provided the most accurate prediction among others [76, 77]. The feed-forward neural network was elsewhere employed to predict the mass loss for the various blends and study the thermodynamic and kinetic behavior of SS with the data collected from the wastewater treatment plant in Islamabad, Pakistan [78].

There are other examples, which seek to predict the performance of SS treatment systems and investigate the parameters affecting the target variables. In Beijing, China, generalized regression neural network models and back-propagation algorithms appeared successful in predicting heat and mass transfer through hot air forced convection in municipal SS from a water recycling facility. The first method ended in higher accuracy for a few samples, whereas the second had greater accuracy for the majority of the data [79]. Still, a need for highly precise and accurate models was felt, which was pertinent to the integration and sophistication of hybrid ML techniques.

In a leading work, the performance of a wastewater treatment plant was foreseen by different ML techniques, including traditional feed-forward, deep feed-forward backpropagation, deep cascade-forward backpropagation, and deep learning time series forecasting with a Long Short-Term Memory network. It was shown that the first and last models pro-

vided the most accurate solutions for predicting the performance of the system [80]. A deep neural network was elsewhere implemented to predict energy consumption using the data previously collected in a wastewater treatment plant in Boumerdes, Algeria, designed to treat urban SS [81]. An overview of the competitiveness, predictability, and performance of different ML algorithms used for SS treatment was summarized and discussed in previous work [82]. It revealed that several studies have already explored the application of different ML algorithms in sewage sludge (SS) treatment and energy recovery, highlighting their potential for accurate prediction of key parameters. For instance, Bagheri et al. [83] compared Gene Expression Programming, Support Vector Machines, and Feed-Forward Neural Networks to estimate the higher heating value of mixed wastes, achieving strong accuracy. Sharafati et al. [84] successfully employed ensemble models such as Adaptive Boosted Regression, Gradient Boosting, and Random Forests to predict chemical and biochemical oxygen demand from wastewater quality indicators. Deep learning methods, such as LSTM networks, have also been applied to forecast removal efficiencies in wastewater treatment, with promising results [85]. In addition, ANN-based approaches have been implemented to study the thermodynamic and kinetic behavior of sewage sludge pyrolysis [86], to monitor moisture content in biomass processing [87], and to predict hydrochar properties in hydrothermal carbonization processes [88]. Collectively, these works illustrate that ML methods—ranging from classical regression models to advanced deep learning architectures—provide competitive and reliable tools for modeling complex physicochemical and thermal behaviors of SS treatment systems.

Notwithstanding the numerous studies carried out based on the chemical composition of SS for the prediction purpose, limited research has been conducted for the prediction of the kinetic/thermodynamic part of SS treatment so far. Moreover, utilizing hybrid ML algorithms was rarely reported in the literature.

1.2.3 Advanced simulation frameworks for thermal treatment systems

Population and economic growth are driving a rapid surge in global energy demand. Worldwide energy consumption in the industrial sector is projected to grow at an average annual rate of 1.4% [89]. Uncertainty over fossil fuel reserves and rising energy costs have raised energy security concerns [90]. At the same time, adopting green energy and reducing waste are vital for sustainability [91]. Consequently, improving energy efficiency is now a key strategy to cut emissions, boost security, and enhance production performance [90]. In response, the Fourth Industrial Revolution emphasizes smart systems that enable energy sustainability through the full digitization and integration of industrial value chains [92]. Energy efficiency in industrial systems is a critical aspect of modern manufacturing and production processes, aiming to reduce energy consumption while maintaining or enhancing productivity [93]. The drive towards energy-efficient industrial systems encompasses a wide range of practices, in-

cluding the optimization of manufacturing processes [94], the adoption of energy-efficient technologies [95], and the implementation of energy management systems [96]. However, achieving higher levels of energy efficiency in industrial systems is not without its challenges. These challenges include the high initial cost of implementing energy-efficient technologies, the changes in existing systems, and a lack of understanding of the long-term benefits of energy efficiency. To effectively address these challenges, researchers recommend adopting a data-driven approach [97].

Among the various energy-intensive processes in wastewater treatment, sludge management remains a significant contributor to overall energy consumption. One very often used method for reducing the volume and hazardous nature of sewage sludge is incineration. This process particularly popular in regions where land availability is limited, environmental regulations are strict, and energy recovery is prioritized. The primary reasons for sludge incineration include substantial volume reduction, elimination of pathogens and harmful organic compounds, and the minimization of landfill use. Incineration facilitates more efficient waste utilization and offers potential for energy recovery by further combustion process. However, this process also poses challenges, such as high operational costs, stringent emission regulations, and the need for careful handling of residual ash.

With regard to wastewater treatment systems, there are a few works suggesting solutions for lowering energy consumption. These include traditional approaches such as statistical analysis and numerical modeling, as well as advanced methodologies incorporating artificial intelligence (AI) and machine learning (ML) techniques. The work of Sun et al. [98] gathers the technologies and methods used for energy saving in wastewater treatment plants. It highlights the challenges of the wastewater treatment industry and the benefits of energy recovery technologies, especially those based on green energy. The authors discuss various solutions. One of them is renewable sources applications, e.g. solar and wind energy, heat pumps, biomass, etc. in order to support the wastewater treatment plant (WWTP) energetic demands. Another widely discussed aspect in this article is the WWTP processes evaluation, control, and optimisation. Sludge treatment is a process of sludge stabilisation, reduction, and harmless treatment. Next, the disposal includes sludge landfill, land use, composting, and thermochemical treatment technologies. This paper summaries the methods for energy consumption reduction at almost every step of the whole wastewater utilisation process. Another work of Di Fraia et al. [99] developed a method to define energy performance indicators, related to the overall energy consumption, and then couple the indicators with removal efficiency. The analysis is based on the assumption that in order to improve pollutants removal, additional, more sophisticated processes are needed, and therefore energy consumption might increase. Therefore, the authors decided to analyse not only energy consumption but its consumption in relation to the efficiency of the WWTP in terms of water cleaning. A large database of data from about 300 wastewater treatment plants, gathered from various sources, was used for the analysis. The authors tested their models with the existing wastewater plant in Italy and demonstrated that their approach

can be useful for assessing potential energy-saving solutions.

The work of Al-Dahidi et al. [100] presents a comprehensive approach for assessing the feasibility of waste heat recovery (WHR) in wastewater treatment plants (WWTPs) with two main objectives. First, an Artificial Neural Network (ANN) model is developed to predict WHR potential based on operational data. Second, an economic analysis is conducted, focusing on the integration of Organic Rankine Cycle (ORC) and Seasonal Thermal Energy Storage systems. While the study highlights the benefits of WHR systems in WWTPs, including energy efficiency, cost savings, and environmental improvements, it does not address the integration of advanced control strategies for optimizing ORC performance under varying operating conditions. Yu et al. [101] use statistical regression methods for analysing the possibilities of controlling and reducing energy consumption of municipal wastewater treatment plants. The authors based on a dataset of daily records gathered within one year, including the energy consumption of unit chemical oxygen demand, which was a measure of energy consumption for pollutants removal. Using Bayesian semi-parametic quantile regression, the authors concluded that the most influential parameters in terms of energy consumption are chromium concentration and wastewater temperature. Ding et al. [102] presented a controlled object model for Municipal Solid Waste Incineration (MSWI). The model details the MSWI process flow, dividing the incinerator into distinct regions and constructing material and energy balance equations for each subsystem. It consists of three main parts: the analysis of the MSWI process based on a grate incinerator, the division of solid and gas phases to develop material balance equations, and the deduction of energy transfer processes using thermodynamic principles. The model was validated using data from an MSWI plant in Beijing, China. Although the model provides a solid foundation for MSWI process control, it does not address the system's optimal performance or operating point.

Although many approaches have been developed to enhance energy efficiency in wastewater treatment plants, issues such as optimizing complex processes, forecasting system behavior under varying conditions, and applying advanced control strategies continue to pose significant challenges. This is where Digital Twin (DT) technology offers a transformative approach by providing real-time virtual representations of physical systems. The term "Digital Twin" was originally introduced by Grieves in 2002 at the University of Michigan [103]. As we illustrated in Fig. 1.1, a DT comprises three essential components. Firstly, DT involves a real-world entity, which could be anything from a single machine to a complete factory. Secondly, DT contains a data-driven simulation model, which includes algorithms that define the simulation, along with machine learning and data mining techniques to extract the model from data, and the software that implements these algorithms. Additionally, DT encompasses connectivity elements such as IoT (Internet of Things) systems. Lastly, the DT incorporates data that the real-world entity has produced or is producing. Data is a critical aspect that significantly affects the achievement of the digital modeling goal effectiveness [97].

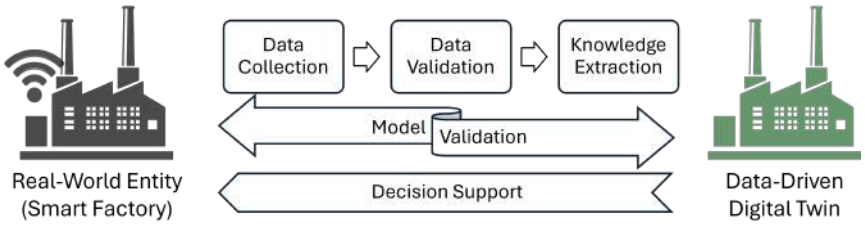

Figure 1.1: Constituent parts of a Digital Twin in a manufacturing system [104]

DT can be also utilized for monitoring and improving energy efficiency in industrial systems, offering significant potential for optimization. DTs actively assist industries in understanding and modeling the energy consumption behavior of systems, analyzing the system regarding different scenarios, optimizing processes to reduce energy consumption, and predicting and comparing the impacts of each change before implementation in the real system. Although DTs are extensively utilized in numerous fields, research specifically addressing their role in energy management within different industrial systems is still not widespread. As a result, we undertook a comprehensive literature review centered on the application of simulation techniques for improving energy efficiency in industrial systems. Generally, simulation models can be constructed following one of these approaches: discrete event simulation (DES), agent-based simulation (ABS), continuous or system dynamics (SD), and hybrid simulation (HS). Among these approaches, System Dynamics (SD), contrary to DES technique, stands out for its ability to model continuous processes and dynamic behaviors over time, making it particularly effective for analyzing complex, evolving industrial systems [105].

These models are often used to simulate and enhance the energy efficiency of the processes that evolve continuously, such as chemical reactions in a plant or the flow of materials in a manufacturing process. A recent review by Wang et al. [106] synthesizes the current state of digital twin applications in wastewater treatment technology, highlighting their potential to enhance operational efficiency, predictive maintenance, and decision-making across various facets of WWTPs and sewage networks. Their work underscores the growing interest in integrating digital twins into wastewater infrastructure, providing a comprehensive overview of existing research and applications. In a related study, numerical modeling combined with real-time monitoring was applied to optimize the aeration system in a wastewater treatment plant, achieving an estimated 20% improvement in energy efficiency. The study demonstrated that predictive modeling and dynamic adjustment strategies can significantly enhance energy management and support more effective plant operation planning [107]. Harrou et al. [108] conducted a study focused on developing short-term forecasting models for energy consumption in wastewater treatment plants using data-driven soft sensors. They compared traditional time-series methods with deep learning approaches. The results showed that adaptive models enhance the accuracy of energy consumption forecasts. This

improvement supports more effective operational and environmental planning. Canete et al. [109] proposed an adaptive neural-network-based soft sensor to predict effluent characteristics in wastewater treatment, coupled with a genetic algorithm for optimized control. The approach was tested on a large-scale activated sludge simulation model. It demonstrated reduced operational costs, compliance with legal effluent constraints, and potential for real-time implementation with improved control over biological processes.

The SD has also been applied to model and manage waste treatment systems, focusing on the interaction of economic, social, and environmental variables. For example, a hybrid framework combining SD with multi-objective optimization has been developed to enhance decision-making in waste-to-energy management [110]. It achieved significant environmental and financial improvements over traditional simulation approaches. Cheng et al. [111] proposed a SD model to evaluate the economic potential of using landfill gas for waste leachate evaporation at a regional incineration plant in Chengdu, China. By comparing two scenarios with varying leachate evaporation and landfill gas utilization ratios, they identified an optimal scenario that improved economic performance by 35%. This scenario offered a promising alternative treatment method with potential environmental benefits. However, the model's limitations, such as unaddressed environmental impacts and economic assumptions, were acknowledged. Another work developed an SD model to optimize municipal solid waste management by analyzing resource use, waste treatment options, and cost structures [112]. The findings suggest that increasing waste sorting efforts and operational productivity can lead to improved financial outcomes. This adaptable model offers valuable insights for decision-making in diverse regions, as demonstrated through a case study in Brazil, where it helped reduce reliance on landfills.

Digital Twin technology has been applied to simulate energy consumption and flow in simplified systems. However, its potential extends to modeling energy flow in closed-loop control systems, offering substantial opportunities for advancement. With this, it can support the optimization of wastewater sludge management through thermal treatment methods. These involve the sludge incineration, which is a well-established technology. With its major advantages as the significant reduction in the input sludge volume, and the destruction of toxic organic compounds and pathogens due to high process temperature, as well as odour minimization [113, 114] is considered a good option, despite the high costs it entails to ensure an effective and environmentally safe combustion process. These consist of the energy-expensive costs of dewatering, drying and auxiliary fuel [115] and high costs that have to be incurred for the efficient exhaust gas purification systems [116]. Since sewage sludge management and processing is said to contribute up to 50% of the total cost of wastewater treatment [116], an increased drive has been observed to reduce the energy consumption through sludge energy recovery within the system for its drying or for generating electricity [117, 118]. Chang et al. [119] reported that, as far as the incineration of dried sludge is considered, the recovered energy is close to the amount of energy used in the process, although the authors pointed out that available data on energy consumption

and recovery are limited.

Guided by the comprehensive overview of the state of the art, to our best knowledge, sludge incineration as a widespread technology, but demanding in terms of specific process requirements, has not lived up to the DT based optimization models. Recently, Song et al. [120] considered smoldering as a potential technology for high-water content sewage sludge treatment due to low energy consumption and cost, as well as simple operation. They developed a digital twin system based on the back propagation neural network model to predict the characteristics of sewage sludge smoldering, while aiming at improving process velocity, and reducing the concentrations of CO/NOx emissions. Though the authors obtained a satisfactory agreement between predictions and experimental data, they pointed out to the method limitations. These include the necessity of developing a hybrid modeling approach, integrating a universal smoldering mechanism with the data-driven method to preserve data training efficiency, as well as the need for adjustment and optimization of the parameters when scaling up the system.

1.3 Thesis objectives and outline

The overarching objective of this thesis is to develop and demonstrate a holistic framework for the analysis and optimization of thermochemical energy conversion systems. This is achieved through three interconnected pillars of research, which structure the dissertation:

I. To advance fundamental modeling of biomass conversion within gasifiers by developing novel numerical methods. This includes the creation of an in-house Dynamic Coupled Eulerian-Lagrangian (DCEL) method to capture particle shrinkage and dynamics, and its comparison against the advanced eXtended Discrete Element Method (XDEM) to evaluate the trade-off between computational cost and predictive accuracy.

II. To extend the scope to system-level analysis and optimization by applying machine learning (ML) techniques. This involves creating a data-driven model of a sewage sludge incineration plant to predict key performance indicators (e.g., furnace temperature, heat transfer rates) and identify optimal operating conditions for enhanced energy efficiency.

III. To implement a real-time digital twin for closed-loop energy optimization. This final objective integrates physical models, analytical calculations, and real operational data within a dynamic simulation environment (AnyLogic) to create a virtual replica of the incineration system, enabling scenario analysis and identifying significant energy-saving strategies.

An overview of the up-to-date research in the field of numerical modeling of thermal and flow processes related to biomass thermal conversion, as well as the utilization of data-

driven techniques for system analysis and optimization, presented in **Chapter 1**, discusses the general trends, yet highlighting the importance of computer-aided methods in the design and performance predictions of modern energy systems.

Chapter 2 focuses on the dynamics of biomass conversion in a gasifier. In this chapter, the presentation of the general characteristics of the gasification process in terms of physical and chemical phenomena involved is followed by the details of the developed in-house two-dimensional (2D) code that implements the Euler-Lagrange approach, referred to as Dynamic Coupled Eulerian-Lagrangian (DCEL). It simulates heat and mass transfer phenomena while taking account of variable particle shape-related bed movement. The goal in view was to propose an in-house computing tool, able to mimic the dynamics of conversion in a fixed-bed with good accuracy and, just as importantly, competitive with more advanced CFD techniques in terms of computational time. For this purpose, the study carried out is limited to the upper part of the reactor, wherein the feedstock thermal decomposition takes place. To demonstrate the potential and benefits of the developed model, the obtained results were qualitatively compared with the results of simulations via the extended discrete element method (XDEM) coupled with 3D CFD, a more advanced method that also makes use of particles' volume change histories. The predictions of both methods were also confronted with the measurement data of a laboratory-scale downdraft gasifier regarding the decomposition progress. Through such validation, attention was drawn to the effect of the level of detail in a modeling approach on the time-variable process characteristics predictions and the computing efficiency.

Computationally efficient numerical modeling is a fundamental support in gaining an in-depth knowledge about the characteristics of complex physicochemical phenomena at the macro- and meso-scale levels, offering a supplement to time-consuming measurement campaigns. Direct use of such knowledge for the design and optimization of real-scale units and systems of gasification or combustion requires multi-parameter analyses. These, either way, may be tedious and computationally intensive due to the large feedstock diversity and number of parameters affecting the treatment process and its outputs. Of interest are thus the data-driven approaches, which are addressed in the following **Chapters 3** and **4**. In **Chapter 3**, a real-scale sewage sludge incineration system served as a case study for energy optimization. The case represents one of the common pathways in sewage sludge treatment, based on fluidized bed technology. The system considered is integrated with the sludge drying installation. The optimization of the system performance thus focuses on three output parameters, such as temperature in a fluidized bed (TFB), steam heat transfer rate (SHTR) and dryer residence time (DRT). Three multi-output individual machine learning (ML) algorithms were employed to predict the target values. For this purpose, ASPEN PLUS simulations were performed for different incineration system characteristics to generate the data-rich framework.

As a considered system of sewage sludge incineration is a type of closed-loop system, it has been the subject of optimization using the digital twin (DT) method. One of the

key challenges when simulating a real-time closed-loop system is accounting for circular dependencies to avoid system lock-ups. Addressing this issue, **Chapter 4** presents an application of a Digital Twin (DT) integrated with analytical solutions developed using in-house codes, aimed at simulating energy consumption in the sewage sludge incineration installation. Given that the system is continuous, system dynamics (SD) was implemented using AnyLogic simulations. Unlike traditional modeling, the developed digital twin framework allows for continuous interaction between the virtual model and the physical system. By using real-time data and simulating various operational scenarios, the DT method shows how different parameters, including biogas flow as auxiliary fuel, moisture content in the sludge, combustion air temperature and flow rate, influence sludge incineration system performance. This information helps with guiding decision-making toward optimal, sustainable configurations, higher efficiency and cost savings.

Chapter 5 provides conclusions from the research carried out, summarizing the key findings and goals accomplished, and outlines the perspectives for future work.

Chapter 2

Dynamics of biomass conversion in a fixed bed

2.1 Fundamentals of biomass gasification

2.1.1 Biomass characteristics

The performance of a biomass gasifier is significantly influenced by the properties of the biomass. To ensure the reliability of a biomass gasifier's design, it is crucial to have a thorough understanding of the physical and chemical characteristics of the feedstock. Any organic components that come from plants or animals are referred to as biomass [121]. Typical sources of biomass include:

- Biological: biological waste, aquatic species and animal waste
- Municipal: yard clippings, paper waste, food waste, refuse-derived fuel and sewage sludge
- Agricultural materials: cattle manure, seed hulls, straw, corn stalks, bagasse and food grain

Ligno-cellulose is a significant component of plant biomass. The fibrous, non-starch portion of plant materials is known as ligno-cellulosic material. Contrasting starches or carbohydrates, ligno-cellulose is difficult for humans to digest and does not pose a danger to the global food provision. The three basic polymers cellulose, hemicellulose, and lignin make up the majority of the polymeric compositions of cell walls and other biomass components [122]. The most prevalent organic substance on Earth is cellulose, which serves as the main structural element of biomass's cell walls. Its percentage varies from 90% (by weight) in cotton to 33% for the majority of other plants. Cellulose is a long-chain polymer with a high degree of composition polymerization and a large molecular weight, and it is represented

by the generic formula $(C_6H_{10}O_5)_n$. Numerous glucose molecules make up its crystalline structure, which is made up of thousands of individual units. Due to its strong structural makeup, it can serve as the skeleton framework for the majority of terrestrial biomass. Another component of a plant's cell walls is hemicellulose. Hemicellulose has a random, amorphous structure with minimal strength, in contrast to cellulose's crystalline, robust, and hydrolysis-resistant structure. It is a class of carbohydrates that can be represented by the general formula $(C_5H_8O_4)_n$ and has a branched chain structure and a lower degree of polymerization [123]. Compared to cellulose, hemicellulose often produces more gases and less tar [124]. Lignin, a complex and heavily branched polymer of phenylpropane, is a critical component of plants' secondary cell walls. Only cellulose is more prevalent among organic polymers on Earth. It is the third crucial component of woody biomass's cell walls. Lignin serves as the glue that holds cellulose fibres between neighboring cells. Benzene rings are the predominant monomeric components in the polymers [125].

In addition to moisture and a tiny amount of ash-like inorganic contaminants, biomass contains a significant number of complex organic molecules. The four main components of organic substances are carbon, hydrogen, oxygen, and nitrogen. Additionally, chlorine and sulfur may be present in trace amounts in biomass (such as municipal solid waste (MSW) and animal waste). The composition of the fuel as well as its energy content are essential for the design of a biomass utilization system, whether it is a gasifier or a combustor. Its composition and energy content are described by the first three attributes listed below: ultimate analysis, proximate analysis and thermogravimetric analysis.

- **Ultimate analysis:** With the exception of moisture and inorganic components, the composition of the hydrocarbon fuel is described here in terms of its constituent fundamental elements. A common final analysis is:

$$C + H + O + N + S + ASH + M = 100\%. \tag{2.1}$$

  The weight percentages of carbon, hydrogen, oxygen, nitrogen, and sulfur in the fuel are represented here by the letters C, H, O, N, and S, respectively. The fuel's moisture content is denoted individually as M. Thus, in the final analysis, only the hydrogen and oxygen found in the organic fuel components are considered to be hydrogen and oxygen, not the hydrogen and oxygen found in moisture [125]. In comparison to proximate analysis, ultimate analysis is more complex and expensive.

- **Proximate analysis:** The composition of the biomass is determined by proximate analysis in terms of its gross components, including moisture (M), volatile matter (VM), ash (ASH), and fixed carbon (FC). The moisture and ash identified in the proximate analysis correspond to those identified in the ultimate analysis. The fixed carbon in the proximate analysis, however, is distinct from the carbon in the ultimate

analysis. It is frequently referred to as the char yield after devolatilization since it excludes the carbon in the volatile matter. The condensable and noncondensable gas components that are released when fuel is heated are referred to as volatile matter. Fixed carbon is the solid carbon of the biomass that remains in the charcoal after biomass devolatilization during thermal decomposition (pyrolysis).

Because the conversion of fixed carbon into gases in the majority of gasifiers dictates the pace of gasification and the yields of process products, it is a crucial metric for gasification analysis. It occurs more slowly than any other conversion reaction, therefore it determines the size of a gasifier.

- **Thermogravimetric analysis:** Due to the time and cost associated with proximate analysis, thermogravimetry (TG) or differential thermogravimetry (DTG) was offered as a substitute by Klass [123]. These methods involve heating a small sample of fuel in an electronic microbalance at the desired pace in a particular environment. This provides a continuous record of the fuel sample's weight change in a TG device. As a result, the fuel's moisture, volatile matter, and ash contents can be determined from the recorded weight loss vs. time (or temperature) graphs.

Depending on the circumstance, the composition of fuel is frequently expressed on multiple bases. Four bases of analysis frequently employed are: as received, air dry, total dry, dry and ash-free (Fig. 2.1).

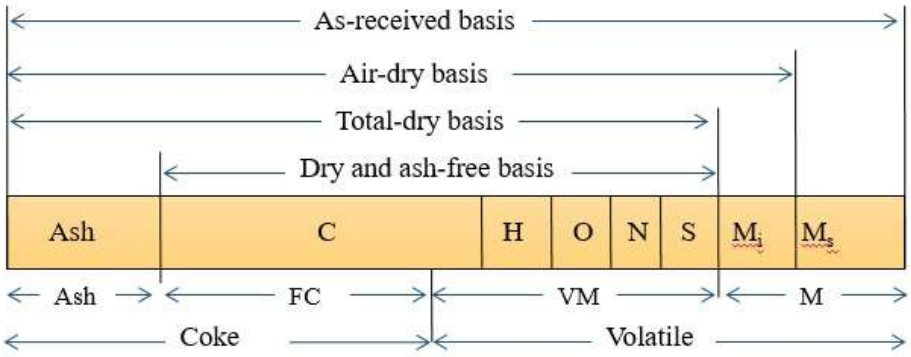

Figure 2.1: Bases for representing the fuel composition (M_i: inherent moisture, M_s: surface moisture).

2.1.2 Biomass gasifier types

There are an extensive variety of gasifiers that can be utilized for biomass gasification which have some contrast in operating condition and design [126]. Fixed bed, fluidized bed, entrained flow bed, rotary kiln, and plasma gasification are the five most typical types of gasifiers. The simplest gasifier technology used by a slow-moving system is a fixed bed

gasifier. It uses oxidizing chemicals and maintains a high pressure for a residence time duration of 900-1800 seconds [127]. Updraft and downdraft reactors are two types of fixed bed gasifiers that differ in their reactor configuration. In both types, biomass feeding location is at the top and ash is discharged at the bottom. Synthesis gas is distributed at the lower level of the fuel bed in downdraft gasifiers, while updraft gasifiers raise it up via the reactor and distribute it at the upper level of the bed. When employed with various waste types, fixed bed reactors have a high conversion rate and negligible ash production. Although, they need a certain kind of feedstock with a low moisture content, which is a problem for the most of feedstocks [128, 129]. In fluidized bed procedures, feedstocks are delivered into the reactor, and then air and more sand are injected to initiate the reaction at an operating temperature of roughly 800-900°C. In order to decompose different types of biomass quickly and maintain a constant temperature inside the reactor, fluidized bed reactors are used in biomass gasification. They can also be upgraded to become large-scale power plants [130]. A new technology called plasma gasification converts municipal solid waste (MSW) into synthesis gas and slag by heating electrically ionized gas to temperatures of up to 10,000 °C in plasma torches with pressures ranging from 1 to 30 bar [131]. In particular for waste incineration, rotary kiln reactors are frequently utilized in industry [132]. Commercially, integrated gasification cycle (IGCC) plants and the chemical industry use entrained flow bed gasifiers [133].

Among all of the gasifiers, fixed bed biomass gasifiers are the most preferred configuration for small- to medium-scale heat and power production [134]. Especially, research and development are quite interested in downdraft gasifier because it is easy to assemble and operate. In fact, downdraft gasifiers accounted for 75% of the manufactured gasifiers in Europe [135]. Moreover, the syngas produced in the downdraft gasifier has a low tar content, so it can be used in gas turbines and engines with less effort in gas purification as compared to updraft gasification. Nevertheless, it usually requires drying of the feed and is not appropriate for biomass with high moisture content; in addition, channelling and blocking of the grate are other disadvantages [136].

2.1.3 Gasification process in a downdraft reactor

The biomass moisture content is decreased in the drying stage. The typical range of moisture content for biomass is 5% to 35%. At a temperature of between 100 and 200°C, drying takes place, resulting in a 5% reduction in the biomass moisture content [134,137]. In most cases, the maximum fuel water content for commercially available gasifiers is 18%, if no pre-drying device is fitted [138]. The lowest fuel water content without additional measures determined using the current gasifier configuration was 8%. [139]. Moisture content has an impact on the calorific value of biomass, which affects flame stability in the combustion zone [140]. When the pyrolysis reactor is heated to 400 K, the moisture content (MC), which is represented by Eq. (2.2), is expected to evaporate.

$$\mathrm{MC} = \frac{m_w}{m_B}. \tag{2.2}$$

Equation (2.3) describes the mass of dry biomass chips, which move downwards to the pyrolysis zone [141]:

$$m_{Dried\,biomass} = (1 - \mathrm{MC})\, m_B = m_{Cell} + m_{Hemi} + m_{Lig}. \tag{2.3}$$

In the pyrolysis stage, the thermal decomposition of biomass occurs in the absence of oxygen or air and volatile matter is released as a consequence of the thermal breakdown of biomass. As a result, the mixture of gases containing carbon monoxide, hydrogen, carbon dioxide and hydrocarbon gases from the biomass is released and biomass is reduced to solid charcoal. The heavier hydrocarbon gases condense at a low temperature to generate liquid tars. Depending upon the type of gasifier, the gases released from drying and pyrolysis zones may or may not pass through the oxidation zone.

In the case of biomass, the pyrolysis process can be presented in Eq. (2.4) in which fuel, composed primarily of carbon, hydrogen, and oxygen atoms under the influence of supplied heat, undergoes conversion into liquid, gaseous and solid products [125,142].

$$\mathrm{C}_n\mathrm{H}_m\mathrm{O}_m \rightarrow \sum_{liquid} \mathrm{C}_x\mathrm{H}_y\mathrm{O}_z + \sum_{gas} \mathrm{C}_a\mathrm{H}_b\mathrm{O}_c + \mathrm{C}_{fix} + \mathrm{H}_2\mathrm{O}. \tag{2.4}$$

The liquid product of pyrolysis is the fraction consisting of the organic part with a very complex chemical composition and water. The gaseous product is a mixture of gases, consisting mainly of carbon mono- and dioxide, methane, hydrogen and higher order hydrocarbons $\mathrm{C_nH_m}$. Carbon, which is a coal concentrate, is a permanent residue of the pyrolysis process [125,143].

The composition and quantity of individual pyrolysis products are influenced by many factors [144]. One of the most important is related to the heating rate of the fuel molecule. If the time needed to heat the molecule to the pyrolysis temperature is much longer than the characteristic pyrolysis reaction time ($t_{heating} \geq t_{reaction}$), pyrolysis is defined as slow.

When the opposite is true, the process is defined as fast pyrolysis. Generally, fast pyrolysis is employed to maximize the liquid product yield, while slow pyrolysis is employed to maximize the gas and solid products yield [143]. Other parameters, which have a significant effect on the amounts of pyrolysis products are the residence time of primary decomposition products in the conversion zone and the maximum process temperature [145].

The desire to produce more liquid fraction and less char comes with rising temperatures. The products of pyrolysis also undergo changes in their elemental composition [146]. Similar results of the influence of temperature on the mass fraction of individual pyrolysis products were obtained by Amutio et al. [147]. The authors studied the pyrolysis of pine wood at temperatures of 400–600°C. An increase in the temperature of the process resulted in an increase in the mass fraction of the gaseous fraction from 8% to 20% and a decrease in the fraction of char from 22% to approx. 15%. An increase in the amount of liquid fraction in the products is related to the high values of the heating rate in the reactor and the short residence time of the primary decomposition products in the reactor [125, 143, 148, 149].

Also, the type of biomass has a significant influence on biomass pyrolysis. Biomass components, cellulose, hemicellulose and lignin have different decomposition temperatures and their content in biomass varies depending on its type [150–153]. The decomposition of hemicellulose during the pyrolysis process takes place mainly in the temperature range of 220–315°C, while the pyrolysis of cellulose takes place at temperatures of 315–400°C. Lignin has a very wide temperature range, in which its thermal decomposition takes place. The pyrolysis begins at 150°C and ends at 900°C. In the work of Zakrzewski [150], the aspects of thermal decomposition of lignocellulosic materials were presented. He points to the range from 160°C to 340°C as the temperature range of active pyrolysis of lignocellulosic raw materials and an increased share of solid carbon residue of the pyrolysis process for raw materials with an increased share of lignin. Gani and Naruse [152] investigated the influence of cellulose and lignin content on the speed of the pyrolysis process. In the case of biomass with a high cellulose content, the pyrolysis process is faster than in the case of biomass with high lignin content. Yang et al. [153] presented the characteristics of cellulose, hemicellulose and lignin pyrolysis. The authors point out that the different content of cellulose, hemicellulose and lignin in the biomass significantly affects the composition of the pyrolysis gases obtained. Hemicellulose with a high content of carboxyl groups contributes to a higher proportion of CO_2. Cellulose pyrolysis shows a higher CO yield, which is related to the degradation of carbonyl and carboxyl groups. With a higher content of aromatic rings, the thermal cracking of lignin promotes a higher content of H_2 and CH_4 in pyrolysis gases.

Solid carbonized biomass, combustible gases, and airborne oxygen are all involved in the process of combustion, resulting in the formation of CO_2. Hydrogen present in the biomass is also oxidized to generate water. There will be the highest temperatures [154]. An excessive amount of heat is released with the oxidation of carbon and hydrogen. The heat released is utilized for drying, pyrolysis and gasification reactions. The oxidized components in the product gas are used as the input concentrations for the reduction zone. As they flow

downward through the bed of blazing fuel particles, a part of them is chemically reduced and the temperature drops [155].

2.2 Development of Dynamic Coupled Eulerian-Lagrangian Method (DCEL)

2.2.1 Case study

For the purpose of this study, the INKA reactor is considered [156], a concurrent-type gasifier designed at the Institute of Fluid Flow Machinery PASc (IMP PAN) in Gdańsk (Poland). Figure 2.2 illustrates the processes within INKA gasifier, focusing on the distinct thermochemical zones involved in the biomass conversion. The reactor has a cylindrical shape with no narrowing at the bottom section, a height of 100 cm, and a diameter of 25 cm. The system is equipped with point-based temperature sensors to measure temperatures in the pyrolysis, oxidation, and reduction zones, respectively. A side-channel blower operating in compression mode is used to maintain a pressurized environment while the generated syngas exits through the bottom of the reactor and is directly combusted in a custom-designed burner.

As biomass gasification is a very involved process, it is challenging to establish and simulate precise reaction pathways. Most models include drying, pyrolysis, oxidation, and reduction as discrete sub-models, as well as modeling for reduction reactions. To simplify the model and better explain the behavior of the downdraft gasifier, the total process can be divided into sub-models of the drying, pyrolysis, oxidation, and reduction zones (2.2b). Consequently, the input parameters of each sub-model are determined by the results obtained at the outlet of the previous sub-model. At this stage of gasification model development, it is assumed that the biomass feedstock is dry, thus excluding the issue of moisture release from the analysis.

In the first step, the pyrolysis zone of the downdraft gasifier should be modeled to obtain the demanding data for the oxidation zone. The particle radius was assumed to be 1.25 cm, which is approximately twice the size of the particles used in the experimental setup. This assumption was made to reduce computational cost. It is further assumed that the top reactor, wherein the fuel decomposition takes place, extends over approximately 25 cm of the reactor height from the top. This assumption is based on initial observations and the data collected from temperature sensors monitoring the thermochemical processes within the reactor.

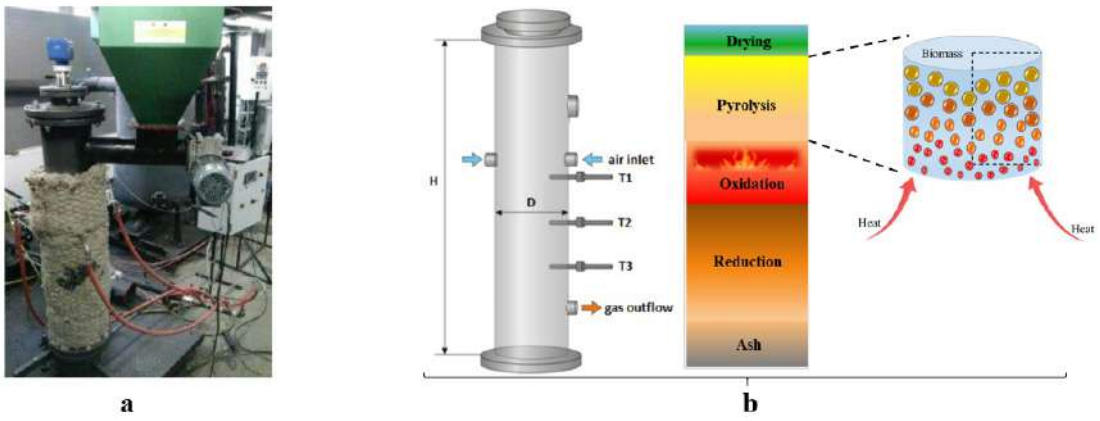

Figure 2.2: Studied case – downdraft gasifier: a) view of laboratory-scale facility with INKA gasifier, b) schematic diagram and process overview in the gasifier, [157].

2.2.2 Model details

To simulate the transport processes during pyrolysis, the dimensions of a laboratory-scale downdraft gasifier developed at IMPPAN Gdańsk, Poland, were adopted. Pyrolysis involves a highly complex interaction between two distinct phases: the solid phase, representing biomass particles undergoing thermal decomposition, and the fluid phase, encompassing the gases released during the devolatilization process. Capturing these interactions mathematically requires a set of governing equations that account for mass, momentum, and energy transfers within and between the phases. The granular layer of the feedstock in the reactor is considered as a porous domain in the Eulerian approach. The analysis begins with the mass balance equations, which form the foundation of the study.

$$\frac{\partial(\varepsilon_s \rho_s)}{\partial t} + \nabla\left(\varepsilon_s \rho_s \vec{v}_s\right) = -\dot{W}_{sg}, \tag{2.5}$$

where ρ_s denotes the density of the solid phase and $\vec{v}_s$ is the velocity of the solid particles. The latter is determined in the Lagrangian framework via determining the particles' positions based on their volume change, which is described in detail in the following section 2.2.3. The parameter ε_s represents the volume fraction of the solid phase in the reactor. In the context of biomass gasification, it describes the fraction of the reactor volume occupied by solid particles, such as biomass and char.

The right-hand side of the equation, $\dot{W}_{sg}$, represents the mass rate of the gas released from the solid phase. Considering the mass of solid phase (biomass) to consist of volatiles (m_v) (part of the solid phase which turns into gas as a result of pyrolysis), and fixed carbon (m_{FC}) and ash (m_a) that do not undergo thermal decomposition, implying that $dm_{FC}/dt = dm_a/dt = 0$, it can be assumed that the mass flow of released volatiles is proportional to the constant pyrolysis rate k_p $[1/s]$ and the difference between the actual volatile mass m_v and the value resulting from slow pyrolysis at a given temperature $m_{v,\infty}$.

Mass rate of released gas is thus defined as a function of solid mass loss rate $Z = m_s/m_{s,0}$, and is given in the form:

$$\dot{W}_{sg} = -\frac{1}{V}\frac{dm_s}{dt} = k_p \frac{m_{s,0}}{V}\left(Z - Z_\infty\right) = k_p \varepsilon_{s_0} \rho_{s_0}\left(Z - Z_\infty\right). \tag{2.6}$$

In the above, V stands for the control volume, and subscript 0 refers to initial values. The reaction rate constant k_p is defined by the Arrhenius equation [158].

The value Z_∞ is determined based on the thermogravimetric analysis (TGA) of the fuel and depends on the temperature and heating rate [156, 158]. There is a maximum degree of fuel degassing at any temperature, in other words, a maximum amount of volatile matter that can be released. The fuel devolatilization that occurs at each temperature under modest heating rates is depicted by a reference curve [159]. A faster heating rate causes a shift of the weight loss curve towards higher temperatures, which means less fuel degassing compared to the reference state. The difference resulting from the shift between the values of mass losses for the given temperature, represented by the term $(Z - Z_\infty)$ in Eq. (2.6), defines the amount of volatile parts that can be released in the further phase of the process. For the purposes of numerical calculations, the quantity Z_∞ is described by a function that approximates the measured data of mass loss.

For the gas phase, the mass balance equation is written:

$$\frac{\partial(\varepsilon_g \rho_g)}{\partial t} + \nabla\left(\varepsilon_g \rho_g \vec{v}_g\right) = \dot{W}_{sg}, \tag{2.7}$$

where ε_g is the volume fraction of the gas phase (porosity), ρ_g is the density of the gas, and $\vec{v}_g$ is the velocity vector of the gas. The solid and gas phase volume fractions are complementary, satisfying the condition:

$$\varepsilon_s + \varepsilon_g = 1. \tag{2.8}$$

The species mass transport equation takes the form:

$$\frac{\partial(\varepsilon_g \rho_g Y_{j,g})}{\partial t} + \nabla\left(\varepsilon_g \rho_g Y_{j,g} \vec{v}_g\right) = \dot{W}_j, \tag{2.9}$$

where $Y_{j,g}$ represents the mass fraction of the j-th gas specie in the gas phase, while $\dot{W}_j$ is the mass generation rate of the j-th specie due to chemical reactions or devolatilization. The term $\dot{W}_{sg}$ in Eqs. (2.5) and (2.7) describes the overall mass rate of gases generated during pyrolysis, which is the summation of $\dot{W}_j$ across all species in the gas phase.

In the case studied, i.e. gas flow through reactive porous media, the Darcy regime may be considered (low Reynolds number flow ($Re < 10$)), where viscous forces dominate over inertial forces, and only the pore-level geometry influences the flow. Under this assumption, the drag force opposing the flow due to the porous structure (Darcy bulk resistance) is introduced as a linear term, corresponding to the second term on the right-hand side of

Eq. (2.10). The governing equations for momentum transfer in the gas phase can thus be expressed as follows [160]:

$$\frac{\partial\left(\varepsilon_g \rho_g \vec{v}_g\right)}{\partial t} + \left(\vec{v}_g \nabla\right)\left(\varepsilon_g \rho_g \vec{v}_g\right) = -\nabla p - \frac{\mu \varepsilon_g \vec{v}_g}{K} - \mu \nabla^2 \vec{v}_g. \tag{2.10}$$

There, μ is the dynamic viscosity of the gas. The second term on the right-hand side, referred to as the Darcy term, represents the stresses at the micro-scale level (within the pores of the medium). Parameter K is the permeability of the material, which is influenced by the structure of the porous (or granular) medium, as well as the density and viscosity of the fluid. As such, K plays a critical role in pressure changes within the bed. In general, it is a tensor. In the case of isotropic material, and this assumption is made for simplicity in this study, this quantity reduces to a scalar. The considered energy equation for the feedstock bed takes the form:

$$\frac{\partial(\rho c T)}{\partial t} + \nabla(\rho c T \vec{v}_s) = \nabla(\lambda \nabla T) - \dot{W}_{sg} h_{sg}, \tag{2.11}$$

where c and λ represent the specific heat capacity and thermal conductivity of the feedstock, respectively. The last term on the right side stands for the heat sink related to the fuel thermal decomposition (pyrolysis), where h_{sg} denotes the process enthalpy.

2.2.3 Methodology and problem solution

An in-house novel dynamic model, referred to as coupled Eulerian-Lagrangian method (DCEL), was developed to address the complexities of biomass pyrolysis in a downdraft gasifier. DCEL integrates the Lagrangian and Eulerian methods through custom-developed code written in FORTRAN and Python. The Lagrangian framework precisely tracks individual biomass particles as they undergo thermal degradation, capturing the intricate dynamics of decomposition and char formation. Meanwhile, the Eulerian method focuses on heat transfer and fluid flow within the gasifier. By coupling these methodologies, the simulation offers a comprehensive view of the pyrolysis process, accounting for both particle-level transformations and the overall fluid behavior. Figure 2.3 illustrates the proposed coupled Lagrangian-Eulerian algorithm, where the Lagrangian approach monitors particle dynamics, including position, temperature, and pyrolysis gas release, and the Eulerian approach manages the continuous phase, emphasizing fluid flow and thermal interactions.

In this method, the simulation starts with a Lagrangian approach to determine the initial and subsequent positions of biomass particles as they move down through the gasifier as their conversion progresses. Conversely, the domain should be meshed using the Eulerian approach. The temperature of each particle is updated during the calculation based on the temperature of the corresponding cells in the Eulerian framework. By knowing the temperature of the particles and using experimental data on the pyrolysis process [161], which describes the volume changes of pine wood as a function of temperature, the reduction

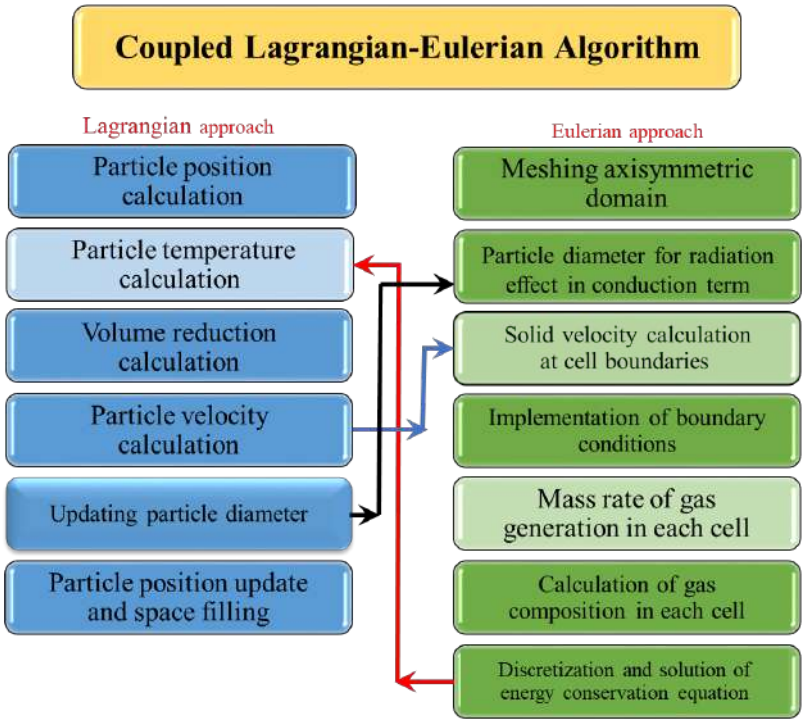

Figure 2.3: Dynamic Coupled Eulerian-Lagrangian (DCEL) algorithm [157].

in particles' volume is calculated. This allows us to determine the radius reduction and the velocity of the particles as they shrink and settle, moving down the reactor. The radius of particles, which is obtained from the Lagrangian approach, is adopted to account for the thermal radiation effect during the Eulerian calculation. Additionally, the velocity of the particles, which directly affects the convection term in the Eulerian approach, is updated through the Lagrangian method. To determine the mass generation in the Eulerian framework, the mass balance equation for the solid fraction is utilized.

In this study, pine wood is chosen as the fuel for the downdraft gasifier, and the experimental data from the TGA measurements were adopted [159, 162].

The mass percentages Y_j for each j-th gaseous component were calculated using experimental data [156], which provided the specific fraction of each species under given conditions. It was assumed that the composition in Eq. (2.9) is solely a function of the temperature of each particle, allowing the model to update the composition dynamically throughout the simulation process. The applied temperature-dependent mass fraction coefficients are summarized in Table 2.1.

To solve the energy equation for the packed bed Eq. (2.11), a volumetric average density (i.e. effective density of packed bed) ρ is taken as:

$$\rho = \varepsilon_s \rho_s + \varepsilon_g \rho_g. \tag{2.12}$$

Similarly, the thermal conductivity was λ assumed as an effective parameter, which

Table 2.1: Temperature-dependent gas mass fraction coefficients, [156]

Temperature range (K)	CO	CO_2	CH_4	H_2
$T < 500$	0.3712	0.6041	0.0232	0.0015
$500 \leq T < 600$	0.4608	0.4666	0.0704	0.0022
$600 \leq T < 700$	0.4938	0.3647	0.1343	0.0071
$700 \leq T < 800$	0.4199	0.2933	0.2245	0.0623
$T \geq 800$	0.4786	0.2256	0.2165	0.0794

accounts for both the conductive and radiative heat transfer. It is given by:

$$\lambda = \varepsilon_s \lambda_s + \varepsilon_g \lambda_g + \lambda_{rad}. \tag{2.13}$$

Here, λ_s and λ_g represent the thermal conductivities of the solid and gas phases, respectively. These values are known based on the material properties of the biomass and the gas composition. The term λ_{rad} accounts for the radiative heat transfer within the packed granular bed that is strongly dependent on the particle diameter d, as it influences the surface area available for radiation. During the pyrolysis process, the particle diameter changes, which, in turn, affects the radiation heat transfer within the bed. The radiative thermal conductivity is described using the Rosseland approximation [163]:

$$\lambda_{rad} r = \frac{16\sigma T^3}{3\left\langle \sigma_{ex} \right\rangle}, \quad \left\langle \sigma_{ex} \right\rangle = f\left(d_p, \varepsilon_g\right), \tag{2.14}$$

where σ is the Stefan-Boltzmann constant and the term $\langle \sigma_{ex} \rangle$ is the effective emissivity, which is a function of the particle diameter d_p and the gas phase volume fraction ε_g. In the DCEL approach, we assume that the particle remains spherical throughout the process. To model particle shrinking, the reduction in particle size is directly governed by the mass loss, following the relationship:

$$\frac{dr_p}{dt} = \frac{dr_p}{dV_p}\frac{dV_p}{dt} = \frac{1}{\rho_s}\frac{dr_p}{dV_p}\frac{dm_p}{dt}. \tag{2.15}$$

where r_p is the particle radius, V_p is the particle volume, ρ_s is the solid density, and m_p represents the particle mass.

Discretization of calculation domain

The finite volume method (FVM) is used for integrating governing equations over a control volume. Thus, the domain should be divided into discrete control volumes around the nodes, i.e. the boundaries are located between nodes. An axisymmetric control volume (Fig. 2.4) is selected to rewrite the equations in cylindrical form.

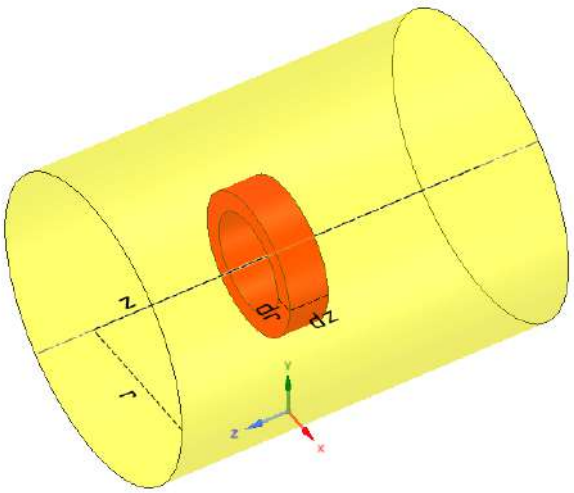

Figure 2.4: An axisymmetric control volume around node

The main point is defined by P and the nodes of W, E, N and S are its neighbours in two-dimensional coordinates, respectively. Each node is surrounded by east, west, north and south side faces, which are identified by w, e, n, and s. Point P and the surrounding control surface are shown in Fig. 2.5.

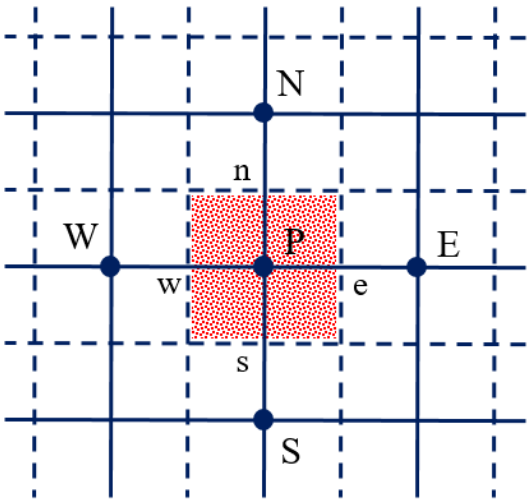

Figure 2.5: Control volume around nodal point.

The conservation law for the transport of a scalar in an unsteady flow has the general form:

$$\frac{\partial}{\partial t}\left(\rho\phi\right) + \nabla\left(\rho u\phi\right) = \nabla(\lambda\nabla T) + S_{\phi}. \tag{2.16}$$

The first term of the equation represents the rate of change term and is zero for steady flows. We must retain this term in the discretisation processes to predict a transient problem. The second contribution describes convection or advection terms. The first and second terms on the left side are called the diffusion term and source term, respectively. In order to make it easier to comprehend how to obtain the coefficient of a tridiagonal matrix, the energy equation is discretized in the following section.

The energy equation in a feedstock bed states a balance between the generation, accumulation and transfer (by diffusion or convection) of thermal energy.

$$\overbrace{\frac{\partial}{\partial t}(\rho cT)}^{transient\,term} + \overbrace{\nabla(\rho cTv_s)}^{convective\,term} = \overbrace{\nabla(\lambda\nabla T)}^{diffusive\,term} - \overbrace{\dot{W}_{sg}h_{sg}}^{source\,term} . \tag{2.17}$$

Unsteady energy equation at an axisymmetric configuration can be expressed as:

$$\begin{aligned}\frac{\partial}{\partial t}(\rho cT) + \frac{1}{r}\frac{\partial}{\partial r}(r\rho cT\,(v_s)_r) + \frac{\partial}{\partial z}(\rho cT\,(v_s)_z) = \\ \frac{1}{r}\frac{\partial}{\partial r}\left(r\lambda\frac{\partial T}{\partial r}\right) + \frac{\partial}{\partial z}(\lambda\frac{\delta T}{\delta z}) - \dot{W}_{sg}h_{sg}.\end{aligned} \tag{2.18}$$

The finite volume integration of Eq. (2.18) over a control volume must be augmented with a further integration over the finite time step Δt. Consider the two-dimensional control volume in Fig. 2.4, integration of the equation over the control volume and over a time from t to $t + \Delta t$ gives [164]:

$$\begin{aligned}\int_t^{t+\Delta t}\int_{CV}\left(\frac{\partial}{\partial t}(\rho cT)\right)dVdt + \int_t^{t+\Delta t}\int_{CV}\left(\frac{1}{r}\frac{\partial}{\partial r}(r\rho cT\,(v_s)_r) + \frac{\partial}{\partial z}(\rho cT\,(v_s)_z)\right)dVdt = \\ \int_t^{t+\Delta t}\int_{CV}\left(\frac{1}{r}\frac{\partial}{\partial r}(r\lambda\frac{\partial T}{\partial r}) + \frac{\partial}{\partial z}(\lambda\frac{\partial T}{\partial z})\right)dVdt + \\ \int_t^{t+\Delta t}\int_{CV}\left(-\dot{W}_{sg}h_{sg}\right)dVdt,\end{aligned} \tag{2.19}$$

where the two left-hand terms represent the transient and convective term and two right-hand terms are the diffusive and source term, respectively. Each term, independently of the other terms, is considered to integrate above equations:

- Transient term:

  If the temperature at a node is assumed to prevail over the whole control volume, the first part of the equation can be written as:

$$\int_{CV}\left[\int_{t}^{t+\Delta t}\frac{\partial}{\partial t}(\rho cT)dt\right]dV=\rho c(T_P-T_P^0)\Delta V, \tag{2.20}$$

where T_P^0 and T_P represent the temperature of node p at time t and $t+\Delta t$, respectively. The first order (backward) differencing scheme has been utilized to substitute $(T_P - T_P^0)/\Delta t$ for $\frac{\partial T}{\partial t}$.

- Convective term

  At the first step, the inner integration over the control volume should be discretized. By replacing the cross-sectional area $A_z = 2\pi r dr$ and $A_r = 2\pi r dz$, the convection term can be divided in two directions, r and z.

$$\begin{aligned}&\int_{t}^{t+\Delta t}\int_{z}^{z+\Delta z}\int_{r}^{r+\Delta r}\left(\frac{1}{r}\frac{\partial}{\partial r}(r\rho cT\left(v_s\right)_r)+\frac{\partial}{\partial z}(\rho cT\left(v_s\right)_z)\right)2\pi r dr dz dt=\\&\int_{t}^{t+\Delta t}\int_{r}^{r+\Delta r}\frac{\partial}{\partial r}(\rho cT\left(v_s\right)_r A_r)dr dt+\int_{t}^{t+\Delta t}\int_{z}^{z+\Delta z}\frac{\partial}{\partial z}(\rho cT\left(v_s\right)_z A_z)dz dt,\end{aligned} \tag{2.21}$$

  where $(v_s)_r$ and $(v_s)_z$ are r and z components of the solid velocity. Integration of equation 2.21 over the control volume face gives:

$$\begin{aligned}&\int_{t}^{t+\Delta t}\int_{r}^{r+\Delta r}\frac{\partial}{\partial r}(\rho cT\left(v_s\right)_r A_r)dr dt+\int_{t}^{t+\Delta t}\int_{z}^{z+\Delta z}\frac{\partial}{\partial z}(\rho cT\left(v_s\right)_z A_z)dz dt=\\&\int_{t}^{t+\Delta t}\left[(\rho cT\left(v_s\right)_r A_r)_e-(\rho cT\left(v_s\right)_r A_r)_w\right]dt-\int_{t}^{t+\Delta t}\left[(\rho cT\left(v_s\right)_z A_z)_n-(\rho cT\left(v_s\right)_z A_z)_s\right]dt\end{aligned} \tag{2.22}$$

  Considering the central differencing approximation, the value of transported temperature at each face can be calculated. For instance, the cell face value of temperature at the east for a uniform grid can be written as:

$$T_e=\left(\frac{T_E+T_P}{2}\right) \tag{2.23}$$

  Equation (2.22) can be arranged by substituting the above expression:

$$\begin{aligned}&\int_{t}^{t+\Delta t}\left[(\rho cT\left(v_s\right)_r A_r)_e-(\rho cT\left(v_s\right)_r A_r)_w\right]dt=\\&\int_{t}^{t+\Delta t}\left[\left((\rho c\left(v_s\right)_r A_r)_e\left(\frac{T_E+T_P}{2}\right)\right)-\left((\rho c\left(v_s\right)_r A_r)_w\left(\frac{T_P+T_W}{2}\right)\right)\right]dt,\end{aligned} \tag{2.24}$$

$$\int_t^{t+\Delta t} \left[\left(\rho c T \left(v_s\right)_z A_z\right)_n - \left(\rho c T \left(v_s\right)_z A_z\right)_s \right] dt = \int_t^{t+\Delta t} \left[\left(\left(\rho c T \left(v_s\right)_z A_z\right)_n \left(\frac{T_N + T_P}{2}\right) \right) - \left(\left(\rho c T \left(v_s\right)_z A_z\right)_s \left(\frac{T_P + T_S}{2}\right) \right) \right] dt. \tag{2.25}$$

Discretizing the right-hand side of this equation needs to make an assumption about the variation of T_n, T_s, T_e, T_w and T_p with time. It can be considered as the temperature at time t or time $t + \Delta t$, as well as the combination of temperature at both times to evaluate the time integral. There is a generalising approach to write the integral of temperature with respect to t by defining a weighting parameter θ between 0 to 1.

$$\int_t^{t+\Delta t} T dt = \left[\theta T + (1-\theta) T^0\right] \times \Delta t. \tag{2.26}$$

In Eq. (2.26), the temperature at old time t is used by considering $\theta = 0$ and the resulting scheme is called explicit. In the implicit scheme, $\theta = 1$ is selected to utilize the temperature at the new time $t + \Delta t$. Finally, $\theta = \frac{1}{2}$ is considered in the Crank-Nicolson scheme, in which the temperature of t and $t + \Delta t$ are equally weighted.

In this study, the implicit scheme is applied to obtain accurate solutions, avoiding convergence problems. Using formula (2.26) for T_w, T_e, T_n, T_s and T_p in the Eqs. (2.24) and (2.25) gives implicit discretization of the convection term:

$$\begin{aligned} &\int_t^{t+\Delta t} \int_{CV} \left(\frac{1}{r} \frac{\partial}{\partial r} \Big(r \rho c T (v_s)_r \Big) + \frac{\partial}{\partial z} \Big(\rho c T (v_s)_z \Big) \right) dV dt \\ &= \Delta t \times \left[\Big(\rho c T (v_s)_z A_z \frac{T_N + T_P}{2} \Big)_n - \Big(\rho c T (v_s)_z A_z \frac{T_P + T_S}{2} \Big)_s \right. \\ &\quad \left. + \Big(\rho c (v_s)_r A_r \frac{T_E + T_P}{2} \Big)_e - \Big(\rho c (v_s)_r A_r \frac{T_P + T_W}{2} \Big)_w \right]. \end{aligned} \tag{2.27}$$

- Diffusive term

  Similar to the convection term, the integration of the diffusive term around the cross-sectional area can be divided into two directions r and z.

$$\int_t^{t+\Delta t} \int_z^{z+\Delta z} \int_r^{r+\Delta r} \left(\frac{1}{r} \frac{\partial}{\partial r} (r \lambda \frac{\partial T}{\partial r}) + \frac{\partial}{\partial z} (\lambda \frac{\partial T}{\partial z}) \right) 2\pi r dr dz dt = \int_t^{t+\Delta t} \int_r^{r+\Delta r} \frac{\partial}{\partial r} (\lambda \frac{\partial T}{\partial r} A_r) dr dt + \int_t^{t+\Delta t} \int_z^{z+\Delta z} \frac{\partial}{\partial z} (\lambda \frac{\partial T}{\partial z} A_z) dz dt. \tag{2.28}$$

Equation (2.28) can be rewritten as the output diffusive flux from the east and north faces minus input diffusive flux from the west and south faces:

$$\int_t^{t+\Delta t}\int_r^{r+\Delta r}\frac{\partial}{\partial r}(\lambda\frac{\partial T}{\partial r}A_r)drdt+\int_t^{t+\Delta t}\int_z^{z+\Delta z}\frac{\partial}{\partial z}(\lambda\frac{\partial T}{\partial z}A_z)dzdt=$$
$$\int_t^{t+\Delta t}\left[\left(\lambda\frac{\partial T}{\partial r}A_r\right)_e-\left(\lambda\frac{\partial T}{\partial r}A_r\right)_w\right]dt-\int_t^{t+\Delta t}\left[\left(\lambda\frac{\partial T}{\partial z}A_z\right)_n-\left(\lambda\frac{\partial T}{\partial z}A_z\right)_s\right]dt. \tag{2.29}$$

The interface diffusion coefficient and the gradient $\frac{\partial T}{\partial r}$ and $\frac{\partial T}{\partial z}$ should be defined at each face of the control volume. Linear approximation is utilized to calculate the interface value of the diffusion coefficient. For example, λ at the east interface in a uniform grid can be obtained by:

$$\lambda_e=\left(\frac{\lambda_E+\lambda_p}{2}\right), \tag{2.30}$$

where λ_E and λ_P are diffusion coefficient at points E and P. Also, the central differencing approximation has been utilized to state $\frac{\partial T}{\partial r}$ and $\frac{\partial T}{\partial z}$. For example, $\frac{\partial T}{\partial r}$ at the east for a uniform grid can be defined:

$$\left(\frac{\partial T}{\partial r}\right)_e=\frac{T_E-T_P}{\delta r_{PE}} \tag{2.31}$$

The distance between nodes E and P is described by δr_{PE}. Substitution of the new definition of diffusive fluxes gives:

$$\int_t^{t+\Delta t}\left[\left(\lambda\frac{\partial T}{\partial r}A_r\right)_e-\left(\lambda\frac{\partial T}{\partial r}A_r\right)_w\right]dt=$$
$$\int_t^{t+\Delta t}\left[\left(\lambda_e\left(A_r\right)_e\left(\frac{T_E-T_P}{\delta r_{PE}}\right)\right)-\left(\lambda_w\left(A_r\right)_w\left(\frac{T_P-T_W}{\delta r_{WP}}\right)\right)\right]dt. \tag{2.32}$$

$$\int_t^{t+\Delta t}\left[\left(\lambda\frac{\partial T}{\partial z}A_z\right)_n-\left(\lambda\frac{\partial T}{\partial z}A_z\right)_s\right]dt=$$
$$\int_t^{t+\Delta t}\left[\left(\lambda_n\left(A_z\right)_n\left(\frac{T_N-T_P}{\delta z_{PN}}\right)\right)-\left(\lambda_s\left(A_z\right)_s\left(\frac{T_P-T_S}{\delta z_{SP}}\right)\right)\right]dt \tag{2.33}$$

In the last step, the diffusive terms are obtained by using the implicit scheme for the integration of the Eqs. (2.32) and (2.33) over the finite time step Δt:

$$\int_t^{t+\Delta t}\int_{CV}\left(\frac{1}{r}\frac{\partial}{\partial r}(r\lambda\frac{\partial T}{\partial r})+\frac{\partial}{\partial z}(\lambda\frac{\partial T}{\partial z})\right)dVdt = \left[\left(\lambda A_r\frac{T_E-T_P}{\delta r_{PE}}\right)_e-\left(\lambda A_r\frac{T_P-T_W}{\delta r_{WP}}\right)_w+\left(\lambda A_z\frac{T_N-T_P}{\delta z_{PN}}\right)_n-\left(\lambda A_z\frac{T_P-T_S}{\delta z_{SP}}\right)_s\right]\times\Delta t \tag{2.34}$$

2.2.4 DCEL simulation - batch reactor mode

The input parameters for DCEL simulation, including physical properties, as well as initial and boundary conditions, are presented in Table 2.2.

At the bottom of the pyrolysis zone, the temperature is primarily influenced by the rate of oxidation occurring in the underlying zone, where the air is supplied. The heat generated from the oxidation reactions drives the pyrolysis process by providing the necessary thermal energy for fuel decomposition. Consequently, the temperature at the interface between the pyrolysis and oxidation zones is modeled as a temperature function, accounting for the heat transfer between these two regions.

The boundary condition at the top of the pyrolysis zone is defined by ambient temperature and pressure, which represent the external conditions of the reactor. Additionally, the walls of the reactor are considered adiabatic, meaning that there is no heat exchange through the side surface. This ensures that the thermal processes occurring within the reactor are not influenced by external heat loss, thus simplifying the model and focusing the heat dynamics within the core of the gasifier itself.

The results presented in Fig. 2.6 illustrate the outcomes of DCEL simulation, showcasing temperature distributions (Eulerian approach) and gas generation profiles (Lagrangian approach) for biomass particles at four distinct time steps: the initial state, 840 s, 1080 s, and 2000 s. These figures elucidate the intricate interplay between heat transfer and gas release during the pyrolysis of pine wood within a downdraft gasifier.

At the onset, the entire computational domain exhibits a uniform temperature of approximately 300 K, and no gas generation occurs. This aligns with the initial conditions where the pyrolysis process has not yet begun. As the temperature in the lower sections of the gasifier reaches approximately 550 K at 840 s, gas generation in the biomass particles becomes noticeable. The shrinking biomass particles and reduced solid domain highlight the progressive mass and volume reduction during pyrolysis.

Particles in the lower layers of the bed experience significant mass loss, reaching the critical threshold for char and ash content, which marks the end of pyrolysis. In contrast, particles in the upper layers actively release gases as they heat up. Biomass particles in a cylindrical arrangement are typically packed more densely at the center due to the bulk behavior of granular materials. This packing effect is accounted for in the model by applying a uniform porosity distribution throughout the domain. Consequently, particles near the

Table 2.2: Input parameters and conditions in DCEL simulation [165–167]

Properties	$\lambda_g = 0.0398$ W/(m K) $c_{p,g} = 1000$ J/(kg K) $d = 0.025$ m $\lambda_s = 0.13 + 0.0003 \times (T - 273)$ $c_{p,s} = 103.1 + 3.867 \times T$ $\rho_s = 550$ kg/m^3 $A = 3000$ 1/s, $E_a = 69000$ J/mol
Initial conditions	$T = 300$ K $\rho_{s0} = \rho_s$ $\varepsilon_{s0}(r) = \begin{cases} 0.6 & r \leq 0.235 \text{ m}, \\ -10.0r + 2.95 & 0.235 \text{ m} < r \leq 0.245 \text{ m}, \\ -20.0r + 5.4 & r > 0.245 \text{ m}. \end{cases}$
Boundary conditions	top: $T(L,t) = T_0$ wall: $\frac{\partial \rho_s}{\partial r} = 0$, $\frac{\partial T}{\partial r} = 0$ bottom: $T(t) = \begin{cases} \frac{10}{18}t + 300 & \text{if } t < 1800 \text{ s}, \\ 1300 & \text{if } t \geq 1800 \text{ s}. \end{cases}$

walls absorb heat more quickly and initiate pyrolysis earlier compared to those at the center. By 1080 s, most of the domain reaches temperatures above the range necessary for active pyrolysis, leading to extensive volatile gas release from the biomass particles. The majority of particles in the lower and middle layers have completed pyrolysis, while the upper layers, now heated to the optimal range (600–700 K), reach their peak gas generation rates. This behavior reflects the intrinsic thermal dynamics of pine wood.

At the final stage of the simulation, the thermal decomposition process approaches completion. Despite further temperature increases within the domain, pyrolysis has ceased for the majority of particles, as the thermal energy is insufficient to break down the stable carbonaceous structures in the char. Residual ash accumulates as a non-reactive byproduct, marking the cessation of mass loss and gas generation.

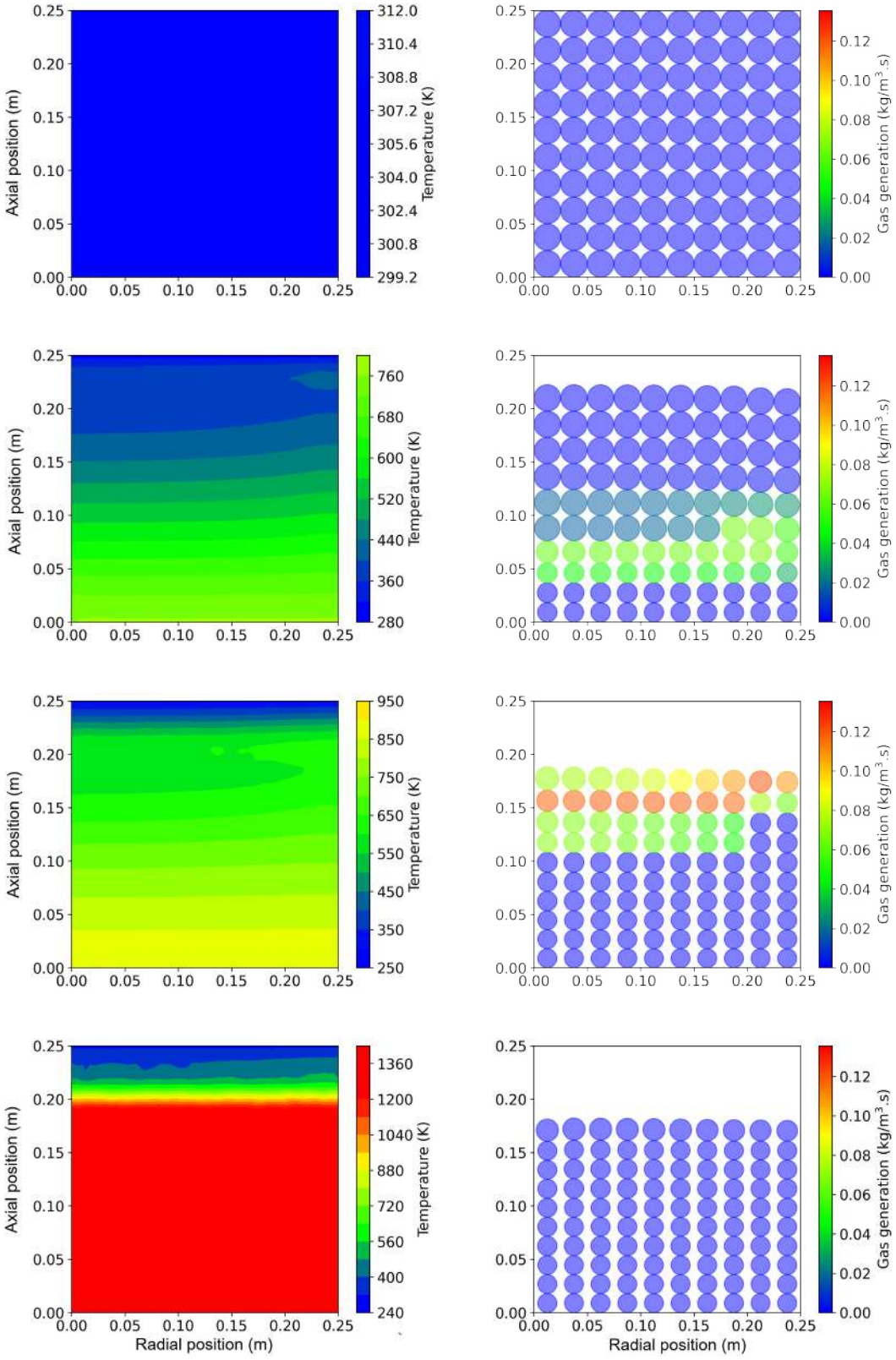

Figure 2.6: Temperature distribution (left) and gas generation profiles (right) during heating at different times. From top to bottom: initial time, 840 s, 1080 s, and 2000 s, [157].

Figure 2.7 illustrates the density distribution within the bed at 840 s and 1080 s, demonstrating the progression of thermal decomposition during the pyrolysis process. At 840 s, the density begins to decrease significantly in the lower layers as the temperature surpasses the pyrolysis initiation range. This reduction in density is attributed to the thermal degradation of biomass into char and volatile gases. The top layers retain higher densities, indicating that they are still undergoing heating and have not fully entered the pyrolysis phase. In contrast, the blue region at the top corresponds to zones where gases, with lower densities, are released as a byproduct of the ongoing decomposition. By 1080 s, the decomposition process is more advanced, with most of the solid particles exhibiting a further reduction in density, particularly in the upper layers as they reach pyrolysis temperatures. The decrease in the bed's overall height reflects the continuous mass and volume loss of the biomass particles, aligning with the shrinking-core model of pyrolysis. The expanded blue zone at the top signifies the accumulation of released gases, consistent with the volatile gas generation observed during pyrolysis. This spatial variation in density highlights the combined effects of thermal decomposition, mass transfer, and gas formation within the gasifier bed.

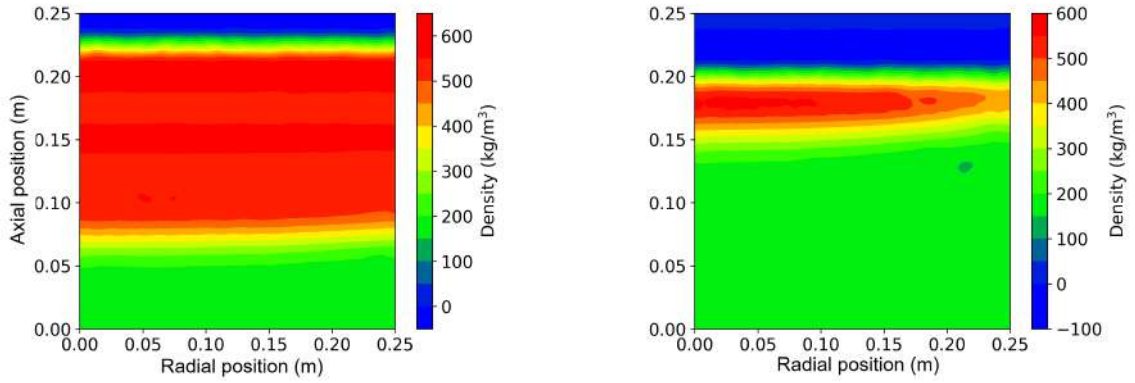

Figure 2.7: Bed density distribution at different times: 840 s (left), 1080 s (right), [157].

Figure 2.8 illustrates the generation rates of various gas components (H_2, CH_4, CO_2 and CO) over time during the pyrolysis process. The trends highlight the sequential release and dominance of different gas species as biomass particles decompose under thermal treatment. Initially, gas generation is negligible, reflecting the lower temperatures that do not yet facilitate significant pyrolysis. As time progresses, temperatures across the gasifier reach the threshold for active pyrolysis, initiating the breakdown of biomass and the release of volatiles. Between approximately 800—1000 s, there is a sharp increase in gas production, corresponding to the peak pyrolysis phase. During this period, the rapid temperature rise accelerates the thermal decomposition of biomass, resulting in the generation of CO_2 and CO as dominant components, with CO_2 reaching higher production rates due to its role in early-stage reactions. CH_4 and H_2 are generated in smaller amounts, with CH_4 primarily emerging from secondary reactions, and H_2 released during high-temperature conditions.

After 1080 s, the gas generation rate sharply declines, coinciding with the depletion of biomass in the reactor as particles reach the critical ash and char content. The distinct behavior of each gas component underscores the heterogeneous and temperature-dependent nature of the pyrolysis process.

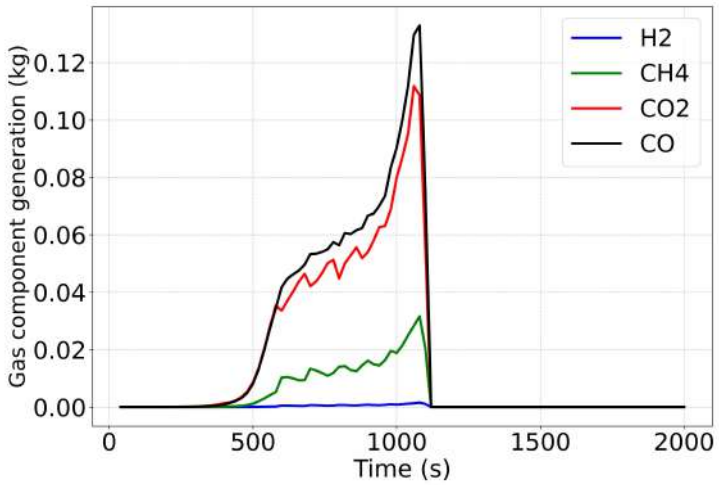

Figure 2.8: Total gas component generation over time in DCEL simulation [157].

2.2.5 DCEL simulation - continuous flow reactor mode

This simulation case aims to recognize the dynamics of feedstock decomposition in a continuous flow configuration, where biomass particles are introduced from the top of the reactor and discharged at the bottom of the calculation domain. A simplified algorithm was applied to determine the placement of newly fed particles, while the velocity of each particle was updated at each time step to calculate its displacement. The removal of the lowest particle occurs once it crosses the bed bottom boundary, ensuring a dynamic balance between feeding and discharge. Particle radii are continuously updated according to local gas generation and mass transfer rates, reflecting progressive shrinkage during pyrolysis. The results presented in Fig. 2.9 show the space-time evolution of temperature (left) and gas generation (right) fields for particle diameter $d_p = 0.005$ m and inlet velocity $v_0 = 0.01$ mm/s. At the beginning of the simulation, the bed remains nearly isothermal at ambient temperature and no volatile release is observed. With time, the heating of the lower section of the reactor (simulating the thermal effect of oxidation reactions) initiates pyrolysis once the local temperature exceeds ~ 550 K, resulting in the first signs of volatile release. As the process advances, the decomposition front gradually migrates upward, driven by heat transfer from the oxidation zone below. The radial distribution of temperature reveals faster heating near the reactor wall compared to the central region, causing earlier initiation of pyrolysis in these zones. This behavior is related to the porosity distribution of the packed

particles, where the bulk material tends to be more densely arranged toward the center, reducing heat penetration and delaying the onset of pyrolysis compared to the less compact near-wall region.

During the intermediate phase, a large fraction of the bed reaches temperatures in the range of 600–800 K, corresponding to the peak of volatile generation. The gas release front becomes more pronounced, and the mass loss accelerates shrinking of particles, leading to continuous rearrangement of their positions. This dynamic behavior highlights the impact of particle feeding and removal on sustaining pyrolysis over extended periods. Eventually, as temperatures in the lower and middle layers exceed 900–1000 K, the volatile fraction of biomass becomes depleted. Gas generation shifts upward, where raw material particles introduced from the top encounter optimal decomposition conditions. At later times, most of the reactor section under consideration is occupied by char with negligible gas release, while the active pyrolysis zone remains concentrated near the upper layers. These results demonstrate how continuous feeding and discharge alter the evolution of pyrolysis compared to the batch mode. The interplay between particle shrinkage, rearrangement, and the upward migration of the active pyrolysis zone is clearly reflected in the coupled temperature and gas generation fields.

Figure 2.10 shows the influence of inlet velocity on the evolution of different total gas components produced in the gasifier. Two cases were considered, with feed velocities of 0.01 mm/s and 0.02 mm/s. In both cases, CO_2 is the dominant product, followed by CO, while H_2 and CH_4 remain comparatively minor throughout the process. The temporal behavior can be divided into four stages. The first observed is an initial lag phase, which represents initiation of the decomposition process (heating the fuel bed from the bottom) with negligible volatile matter release. The second is a sharp rise in gas generation between $\sim$ 400–700 s that is related to the onset of fuel particles' devolatilization in the lowest bed layer, i.e. just above the combustion zone (compare Fig. 2.9 top maps). The third stage, between 700 and 1700 s corresponds with the stabilization of gas release at a reduced rate, associated with the propagation of a uniform high-temperature (compare Fig. 2.9, maps for times between 840 and 1540 s). The last stage, for process time exceeding 1700 s, represents the stabilization of the reaction front with the reduced temperature, caused by the feeding of the raw material from the top (see Fig. 2.9, bottom maps for 2000 s).

A higher fuel feed rate means a greater amount of raw material to be converted inside the reactor. However, while the main stage of the conversion process is more intensive for higher inlet fuel velocity, resulting in larger interim pyrolysis gas yields, the onset of fuel decomposition is delayed (i.e. gas release maxima are shifted to longer process duration times). This is a consequence of delaying the propagation of the high-temperature front upward in the reactor by the movement of the fed raw material down the reactor.

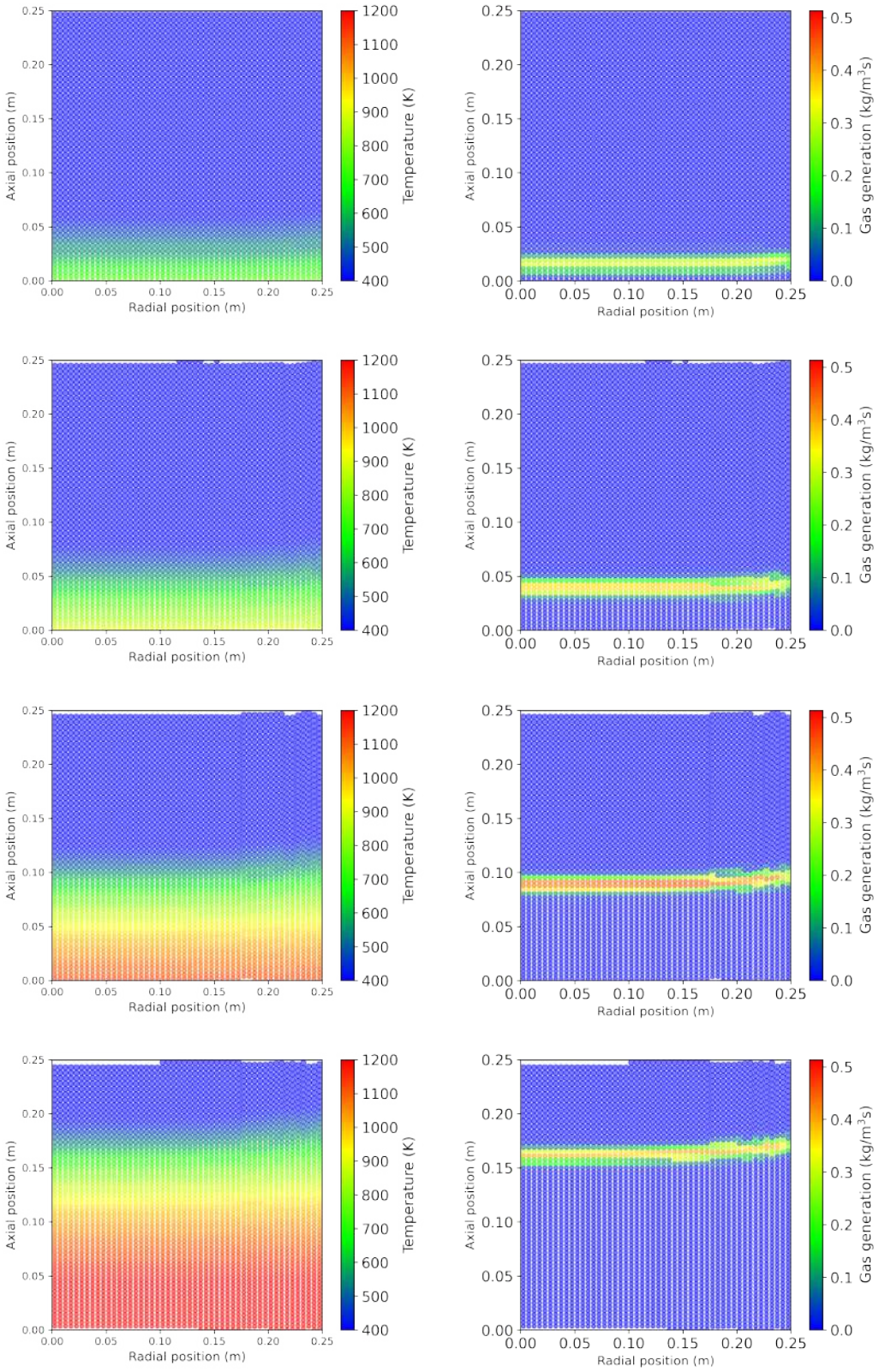

Figure 2.9: Temperature (left) and gas generation (right) at initial velocity 0.01 mm/s and particle diameter 5 mm for times: 840, 1080, 1540, and 2000 s.

Figure 2.11 displays the total gas component generation in the gasifier for particle sizes of 5 mm and 10 mm. Overall, CO_2 and CO are the dominant gaseous products, followed by smaller amounts of H_2 and CH_4. The profiles exhibit a sharp rise during pyrolysis, followed by a plateau or decline as the process slows down. The effect of particle size is evident in both the timing and intensity of gas release. Smaller particles (5 mm) heat up more rapidly due to enhanced heat transfer within the bed, causing them to reach pyrolysis temperature sooner. As a result, the release curves are broader and more gradual. In contrast, larger particles (10 mm) reach the devolatilization temperature in the later phase of the process. However, once decomposition advances, the temperature distribution in the reactor becomes more uniform. This causes a greater portion of the material to reach the pyrolysis threshold almost simultaneously, resulting in more synchronized gas release and sharper, higher peaks in generation, particularly for CO_2 and CO. Despite these differences in timing and peak intensity, the total cumulative amounts of gas produced by the end of pyrolysis remain similar for both particle sizes. These outcomes highlight that particle size governs not only the rate of heating but also the shape of the gas release profile during biomass pyrolysis.

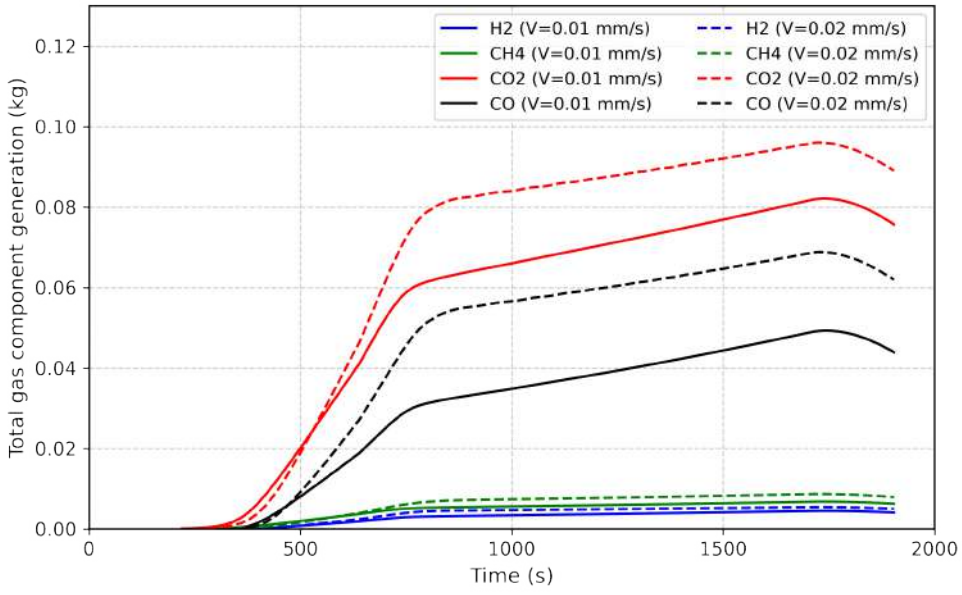

Figure 2.10: Total gas component generation at different fuel feed rates, 0.01 mm/s and 0.02 mm/s; fuel particle diameter of 5 mm.

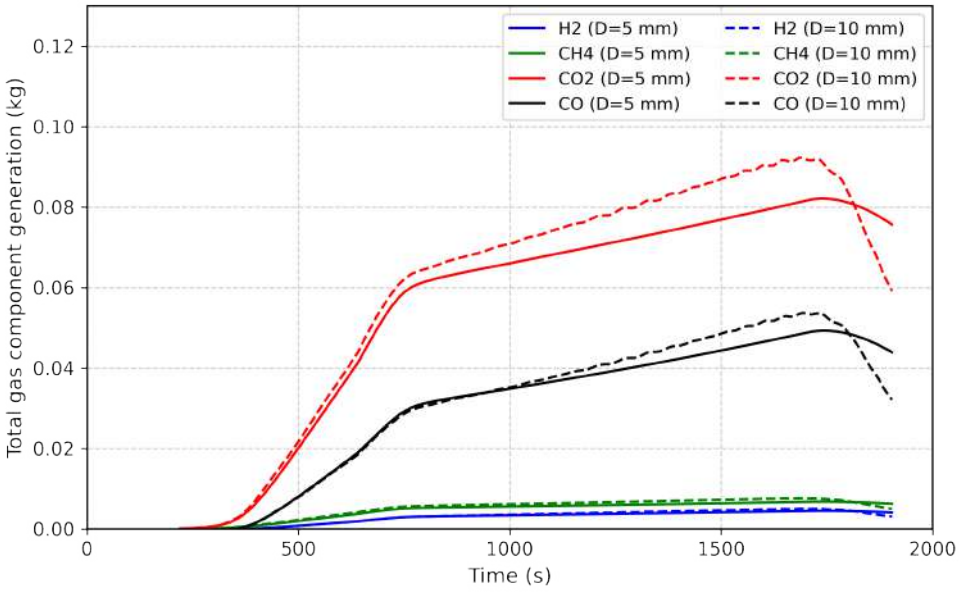

Figure 2.11: Total gas component generation for different particle sizes, 5 mm and 10 mm; fuel feed rate of 0.01 mm/s.

2.3 Validation and comparison of DCEL method and XDEM

To estimate the potential of the developed DCEL method and the accuracy of its predictions, a qualitative comparison of the obtained simulation results was carried out with the predictions of a more advanced method, also based on the mixed Lagrangian-Eulerian approach, which is the XDEM (eXtended Discrete Element Method). This was followed by the validation of both methods' outcomes with experimental data.

2.3.1 Brief description of XDEM basics

The XDEM is an in-house code for simulating processes involving granular materials and fluid interactions. It can predict the behavior of solid fuel particles during thermal treatment via coupling CFD with DEM in a four-way approach [35]. CFD, in the frame of OpenFOAM source [36], allows computing the external flow parameters, in which the extended-DEM module predicts the positions of moving solid fuel particles, providing information about their thermal conversion with the related change in the structure. Each particle, considered to consist of liquid, solid, and gas phases, is assumed to undergo thermodynamic transformations due to heat exchange with the hot surrounding gas. These are described by a set of transient 1D balance equations for mass, momentum, and energy that are solved in the XDEM module [37, 38]. The method accounts for such phenomena as a diffusive and

convective transport of a multicomponent gas mixture through the porous structure of the particle, heat transfer between neighboring particles by conduction and radiation, and heat and mass exchange between fluid and particles. Chemical reactions, including those taking place inside the particle, are modeled as equilibrium reactions.

The computational domain filled with particles is considered a porous medium with the fluid flowing through, modeled as a continuous phase, taking into account the pressure drops. Heat and mass flow between particle and fluid are numerically realized through the source terms that combine the XDEM with the CFD modules.

The XDEM module consists of two parts that can operate simultaneously or separately. Motion-related parameters such as position, velocity, and acceleration are calculated by the dynamics module of the XDEM, while other thermochemical parameters (particle composition, temperature, mass and volume) are predicted by the conversion module [168]. The translational and rotational motions of each particle are predicted based on the equations of classical mechanics according to the following equations:

$$m_p \frac{d\vec{v}_p}{dt} = \vec{F}_c + \vec{F}_g + \vec{F}_b + \vec{F}_d \qquad I_p \frac{d\vec{\omega}_p}{dt} = \sum_j \vec{M}_{p,j} \tag{2.35}$$

where m_p denotes the particle mass, $\vec{v}_p$ is its velocity, $\vec{F}_c$ is a contact force, $\vec{F}_g$ is the gravitational force, $\vec{F}_b$ is the buoyancy force, and $\vec{F}_d$ is the drag force. The contact force of a particle is the sum of all normal $\vec{F}_{c,n}$, and tangential $\vec{F}_{c,t}$ collision forces generated while colliding with the neighbouring particles [169, 170].

Each particle under consideration in the conversion module of XDEM is treated as an ideally spherical solid of porous structure with the privileged direction of flow of released gas. The set of governing equations comprises of: (i) mass conservation for gas flow in the porous zone (similar to Eq. (2.9), (ii) gas momentum conservation, (iii) mass balance of an individual i-th specie, and (iv) energy conservation equation, taking the form, respectively:

$$\frac{\partial}{\partial t}\left(\varepsilon_g \rho_g\right) + \frac{1}{r^2}\frac{\partial}{\partial r}\left(r^2 \varepsilon_g \rho_g v_g\right) = \dot{W}_{sg}, \tag{2.36}$$

$$\frac{\partial p}{\partial r} = -\frac{\varepsilon_g \mu_g}{K} v_g, \tag{2.37}$$

$$\frac{\partial}{\partial t}\left(\varepsilon_g \rho_{g,i}\right) + \frac{1}{r^2}\frac{\partial}{\partial r}\left(r^2 \varepsilon_g \rho_{g,i} v_g\right) = \frac{1}{r^2}\frac{\partial}{\partial r}\left(r^2 D_i \varepsilon_g \frac{\partial \rho_{g,i}}{\partial r}\right) + \varepsilon_g \sum_k \dot{\omega}_{k,i}, \tag{2.38}$$

$$\frac{\partial}{\partial t}\left[\left(\rho c_p\right)_p T\right] + \frac{1}{r^2}\frac{\partial}{\partial r}\left(\frac{1}{r^2} v_g \rho_g c_{p,g} T\right) = \frac{1}{r^2}\frac{\partial}{\partial r}\left(r^2 \lambda \frac{\partial T}{\partial r}\right) + \sum_k \dot{\omega}_k \Delta H_k. \tag{2.39}$$

In the above, the medium properties, such as porosity ϵ_g and permeability K refer to the particle. Term $\dot{\omega}_{k,i}$ is the source term accounting for the consumption/production of

i-th specie from k-th reaction and D_i is the molecular diffusion coefficient. Parameter λ represents an effective thermal conductivity. The last term on the right-hand side in Eq. (2.39) is a total heat source due to the flow with chemical reactions and ΔH_k is the k-th reaction enthalpy.

In the simulations, symmetry boundary conditions are applied at the center of the particle, taking the form, respectively:

$$-\lambda \frac{\partial T}{\partial r}\bigg|_{r=0} = 0, \quad \text{and} \quad -D_i \frac{\partial \rho_{g,i}}{\partial r}\bigg|_{r=0} = 0. \tag{2.40}$$

while at the particle's external surface, the following conditions are assumed:

$$-\lambda \frac{\partial T}{\partial r}\bigg|_{r=R} = \alpha \left(T_s - T_\infty\right) + \dot{q}_{rad} + \dot{q}_{cond}, \tag{2.41}$$

$$-D_i \frac{\partial \rho_{g,i}}{\partial r}\bigg|_{r=R} = \beta_i \left(\rho_{s,i} - \rho_{i,\infty}\right) + \dot{m}_{g,i}, \tag{2.42}$$

where α and β are the heat and mass transfer coefficients, respectively, T_∞, and $\rho_{i,\infty}$ denote ambient gas temperature and gas partial density of the i-th mixture specie. The term $\dot{m}_{g,i}$ determines the exchange of i-th specie by an advective transport through the particle's surface. The heat fluxes on the right-hand side of Eq. (2.41) account for radiative and conductive heat transport between considered particle p and neighboring particles (or objects) j [168, 169]:

$$\dot{q}_{rad} = \sum_j F_{p\to j}\sigma \left(T^4 - T_j^4\right), \quad \text{and} \quad \dot{q}_{cond} = \sum_j \frac{1}{\frac{1}{\lambda_p} + \frac{1}{\lambda_j}} \frac{T - T_j}{\Delta x_{p,j}}, \tag{2.43}$$

where $F_{p\to j}$ denotes the view factor.

The gasification process chemistry involves a kinetic scheme for a two-step global model that describes the biomass thermal decomposition and the oxidation of bio-char [171].

A more detailed description of the XDEM features, including the reaction mechanisms of biomass decomposition, char oxidation and volumetric reactions, is provided in the latest work [157].

2.3.2 XDEM simulations

The XDEM simulation of a batch reactor case, corresponding to the one considered in Section 2.2.4, served as a reference to estimate the suitability of the developed simplified DCEL method for the conversion dynamics predictions.

The simulation carried out for this purpose [157] involved, in the first step, filling the reactor with wood particles of 25 mm in diameter, falling according to gravity. Their initial positions were calculated using the dynamic part of the XDEM module. In the next step, the

thermal conversion XDEM module coupled with CFD (OpenFOAM software) was utilized to obtain the thermal and physical parameters of particles subjected to the external fluid field. Here, the heat was transferred from the hot air that flows into the reactor through the bottom surface. The air temperature was assumed to increase linearly from 300 K to 1300 K within the 1800 s, and remain at this level thereafter until the simulation is completed (4000 s). Sample results of the XDEM simulation, demonstrating the predicted progress of biomass thermal treatment in the reactor, are presented in the form of 3D maps in Fig. 2.12. It displays the particle mean temperature distribution (top line maps) and its mass fraction (bottom line maps) for selected duration times, 1080 s (left) and 3600 s (right). The results show an increase in the bed temperature from the bottom (z = 0 m) to the top, which is due to heat exchange with the hot air, as well as the thermal effects of oxidation reactions of char and flammable pyrolysis gases. Simulaneously, a decrease in the reactor backfill level due to the particle mass and volume change is predicted (compare left and right maps).

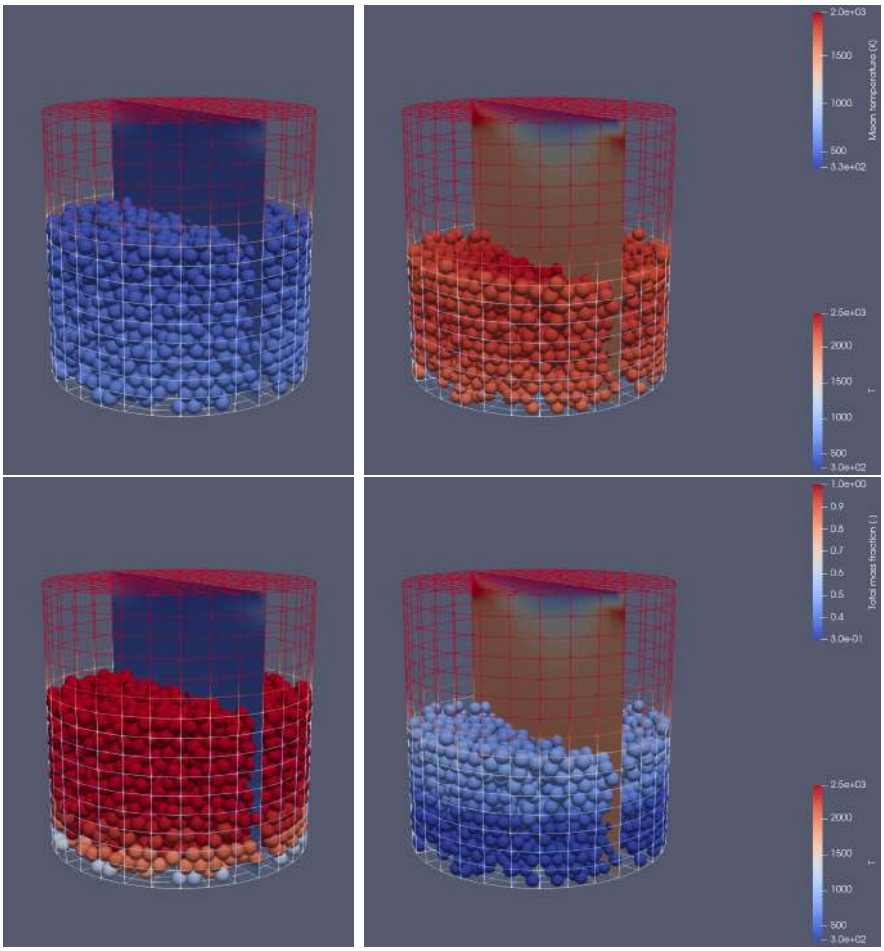

Figure 2.12: Particle mean temperature distribution (top) and its mass fraction (bottom) for selected duration times: 1080 s (left), 3600 s, (right) [157].

Figure 2.13 illustrates changes of bed temperature (CFD porous zone) and porosity distributions on the center plane of the reactor (see Fig. 2.12). Here, a high level of the maximum temperature is related to the oxidation reactions of char and released volatiles (CH_4, CO, H_2, tars). As the process progresses, an increase in bed temperature results in the decomposition of particles, causing them to lose their mass and shrink, which leads to an increase in inter-particle spaces and thereby the bed porosity. The latter increases along the bed height, as well as changes in the radial direction, as shown in Fig. 2.13 (right graphs). Model predictions indicate greater porosity near the wall as compared to the core of the bed. Higher permeability and related channel flow enhance heat transfer in the near-wall zone, which is exhibited in the parabolic-shaped temperature distribution plots.

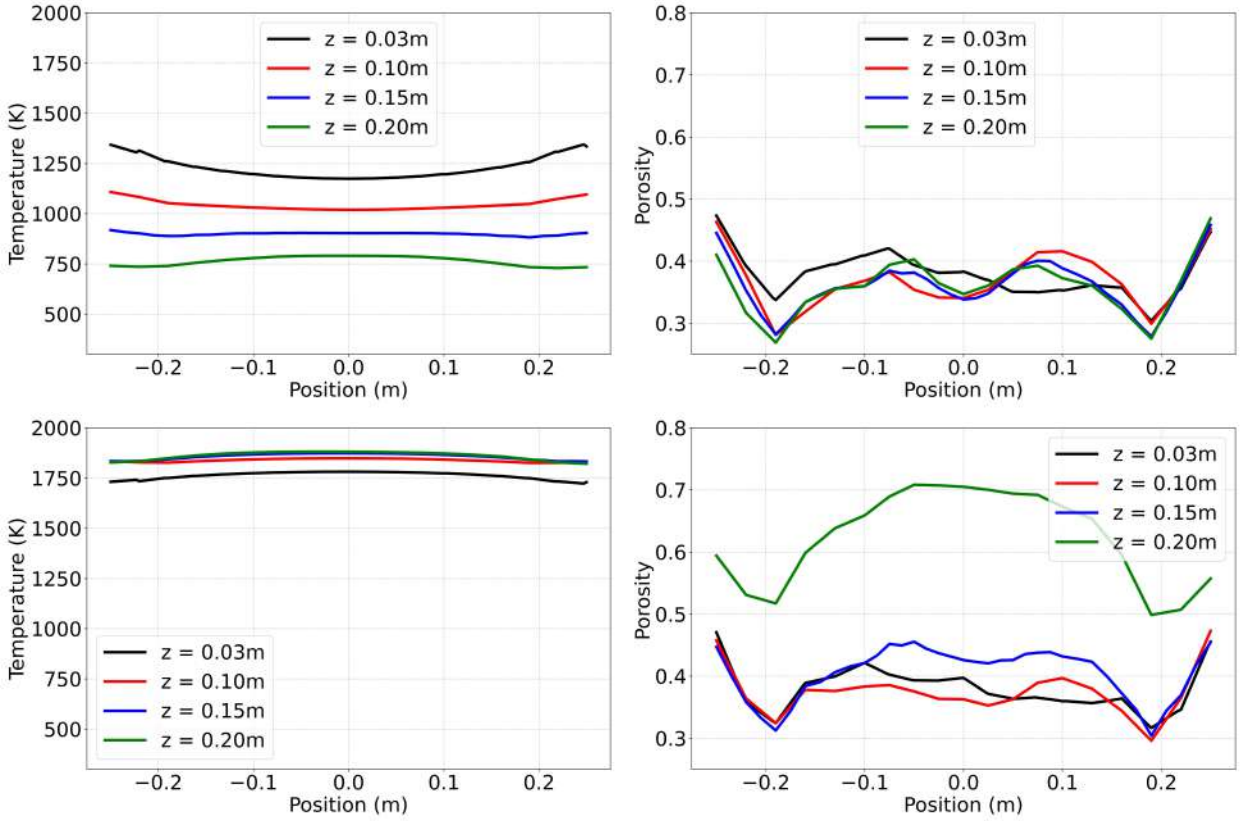

Figure 2.13: Temperature distribution (left) and porosity distribution (right) for: 2000 s (top), 3600 s (bottom), [157].

Through particle tracking in the 3D domain, XDEM provides a better picture and understanding of the conversion process dynamics. Figure 2.15 shows the time variations of the mean temperature and mass fraction for the selected particles. The bottom-most tracked one is located near the hot gas inflow, and the top-most one lies on the upper surface of the fixed bed. Initial positions of selected particles are schematically depicted in Fig. 2.14. As can be observed from the simulation results, particle devolatilization and char oxidation

dynamics depend on the particle location within the bed. For PID 3200, the heating takes around 1000 s and devolatilization completes at 1500 s. Char starts to reduce at 1500 s and that time defines the last stage of thermal conversion, i.e. the gasification/combustion phase. For PID 1300, these times are 1500 s and 2000 s.

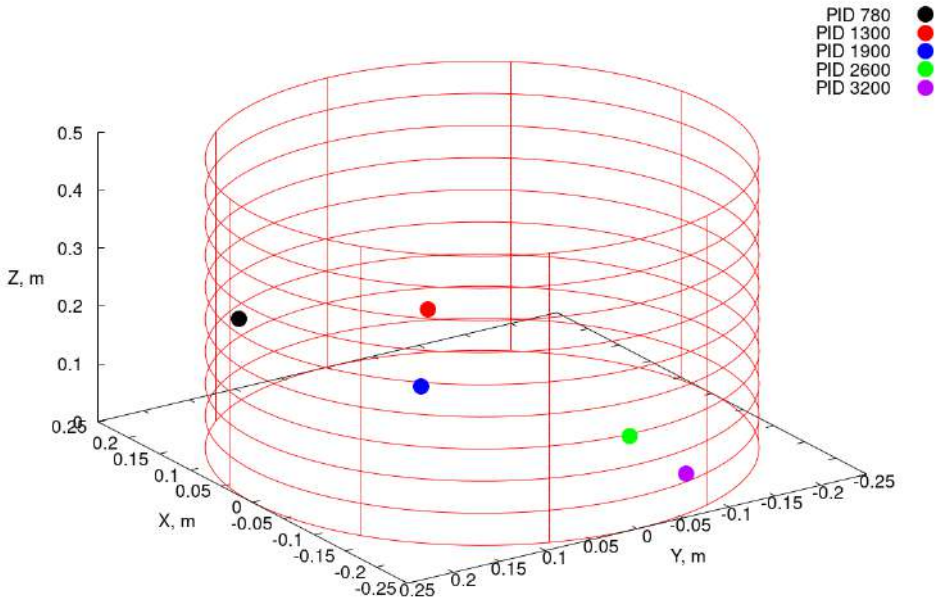

Figure 2.14: Initial positions of selected particles [157].

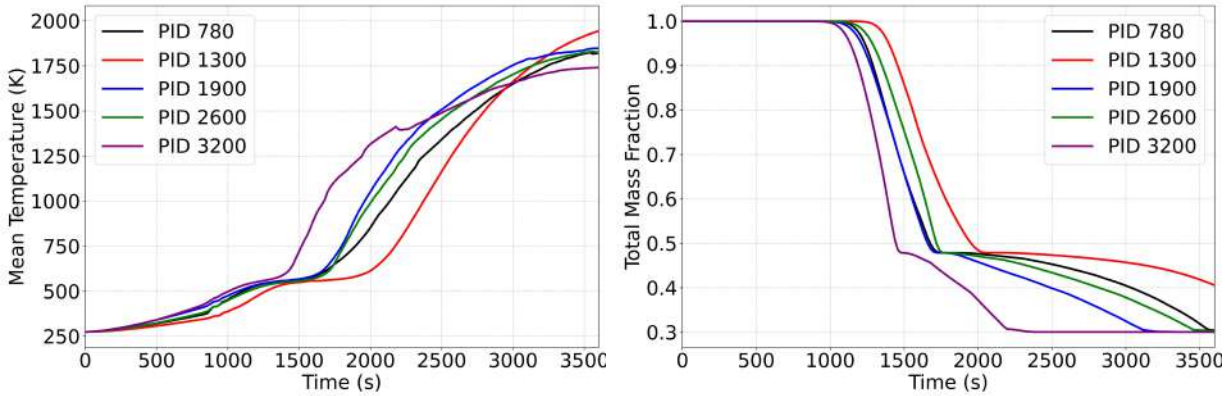

Figure 2.15: Mean temperature distribution (left) and mass fraction (right) over time for selected particles [157].

2.3.3 Comparative analysis

Figure 2.16 demonstrates a comparative analysis of biomass mass loss during pyrolysis as a function of temperature, using both experimental data and simulation results from the DCEL and XDEM models. According to the thermogravimetric analysis (TGA) data for pine wood (points), significant gas generation (mass loss) commences when the particle temperature exceeds 600 K, with the peak generation occurring between 600 and 700 K.

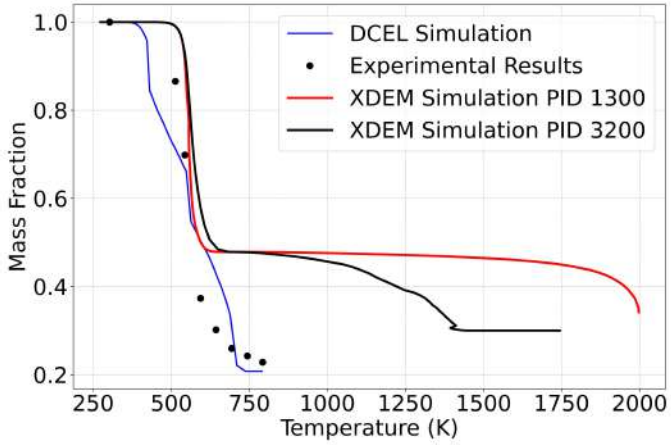

Figure 2.16: Comparison of experimental and simulated biomass mass loss over time, [157].

The results show that the developed DCEL model, which incorporates radiation heat transfer linked to the particle diameter, predicts higher temperatures and a faster pyrolysis process compared to XDEM. This is due to the enhanced heat transfer effects. The DCEL results demonstrate strong alignment with experimental data, validated by a calculated Root Mean Square Error (RMSE) of 0.0878 and a Mean Absolute Error (MAE) of 0.0685. Two sets of XDEM results (PID 1300 and PID 3200) are also displayed. In the XDEM model, combustion is explicitly modeled, resulting in higher temperatures within the domain compared to the DCEL model, which considers only the pyrolysis stage. This leads to notable differences in the predicted thermal behavior of biomass. Both models and experimental data reveal a sharp decline in biomass mass fraction within the temperature range of 600–700 K, corresponding to the most intense release of volatiles. The close match in this region highlights the validity of both models, despite minor discrepancies due to model simplifications and experimental variability.

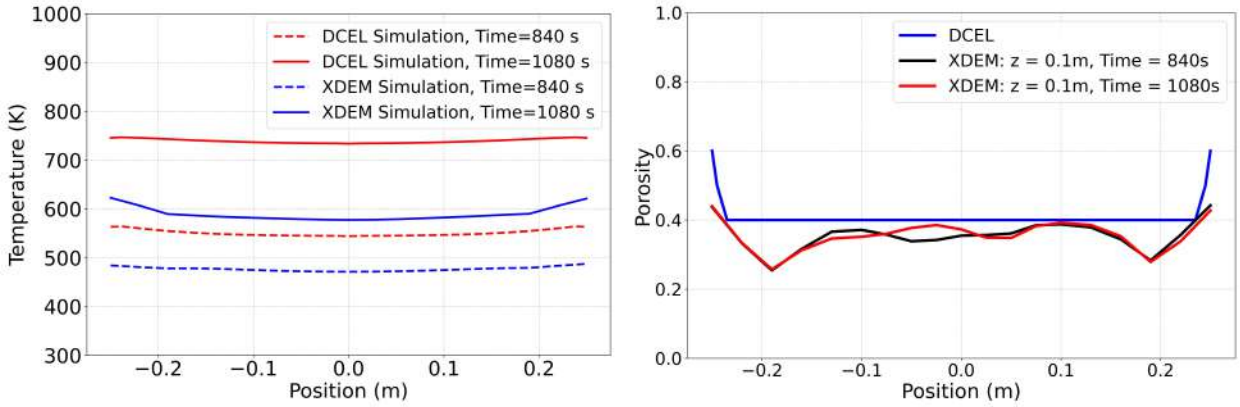

Figure 2.17: Temperature (left) and porosity (right) distributions in DCEL and XDEM simulations, [157].

Figure 2.17 compares the temperature and porosity distributions across the reactor domain at different simulation times for the DCEL and XDEM models. In the DCEL simulation, the inclusion of a radiation heat transfer model results in faster heat propagation and higher temperatures over time compared to the XDEM approach. The differences between the temperature distributions predicted by these two methods become more pronounced as the simulation progresses. The porosity distribution in the DCEL approach is assumed to remain constant throughout the process. In contrast, the XDEM results, which incorporate more detailed phenomena such as combustion and localized effects, show significant variations in porosity over time, reflecting the dynamic nature of biomass decomposition and char formation.

It should be underlined that the XDEM simulation involved the full 3D case computation, which was strictly related to the number of tracked particles, for which the complete set of governing equations was solved. This largely impacts the computational power and calculation time. The duration time of the complete simulation for the studied was at the level of days. However, it is noteworthy that an increased simulation time in the XDEM translates into more detailed and accurate predictions. The time needed to obtain the results from the proposed in-house 2D DCEL model, yet less detailed, was two orders shorter (a few hours).

2.4 Conclusions

An in-house two-dimensional model was developed and implemented, referred to as the dynamic coupled Eulerian–Lagrangian (DCEL) method, to study the transient processes involved in the thermochemical conversion of biomass fuel in a small-scale downdraft gasifying reactor. DCEL simulations were performed for the batch reactor case. The computation results were compared with the outcomes of 3D XDEM simulation. The objective was to

evaluate their suitability for analyzing individual steps of the devolatilization and combustion processes, and for optimizing operational parameters to enhance overall process efficiency. Both methods consider particle behavior during heating, but differ in their level of detail, which results in noticeable differences in computational cost.

The DCEL approach, based on bulk medium properties in the Eulerian domain, is computationally more efficient and capable of capturing particle behavior within externally imposed temperature fields. It provides a robust framework for analyzing the coupled thermal and chemical processes governing biomass conversion. By contrast, the XDEM approach explicitly resolves the motion and interactions of individual particles, while simultaneously predicting their evolving physical and structural parameters. This level of detail enables XDEM to represent kinetic chemistry and heterogeneous reactions more comprehensively, at the expense of significantly higher computational demand.

The key findings of the comparative analysis can be summarized as follows:

- The DCEL model predicts higher heat transfer rates through the porous zone than the XDEM, primarily due to differences in modeling radiative heat transfer.

- The two modeling approaches exhibit distinct particle shrinkage dynamics, driven by their respective pyrolysis sub-models and the inclusion of char oxidation in the XDEM.

- Differences in shrinkage rates affect not only overall mass loss but also porosity distribution within the particle bed.

- Both models capture the increase in near-wall porosity and the associated nonuniform thermal front propagation. However, the XDEM predicts lower porosity overall, owing to three-dimensional particle rearrangement.

Beyond this comparison, additional DCEL simulations were performed to investigate reactor-scale behavior under continuous-flow operation. In this configuration, the interplay of particle feeding, shrinkage, and discharge sustained pyrolysis over extended operation. The results revealed upward migration of the active pyrolysis zone, faster heating near the reactor walls, and continuous rearrangement of particles as mass was lost. Compared to batch mode, continuous operation maintained gas generation by ensuring raw biomass supply, while the lower parts of the fuel bed progressively converted to char.

Sensitivity studies further highlighted the influence of operating parameters on the decomposition progress in the reactor. Higher feed velocities (0.02 mm/s vs. 0.01 mm/s) led to a more intensive devolatization in the main stage of the conversion, but simultaneously, to a delay in the onset of fuel decomposition. However, this did not alter the hierarchy of dominant gas species ($CO_2 > CO > H_2$, CH_4). Particle size was shown to be a critical factor: smaller particles (5 mm) promoted faster heating, but more prolonged gas evolution,

while larger particles (10 mm) decomposed more slowly. Despite these kinetic differences, cumulative gas yields at the end of pyrolysis were comparable across particle sizes.

Overall, in the context of qualitative comparison, the DCEL method appears to be a promising tool for analyzing biomass conversion processes. While XDEM offers greater detail for particle-level insights, DCEL provides computational efficiency and flexibility for reactor-scale studies. The extended analyses, including continuous-flow operation and parameter sensitivity, confirm that hydrodynamic conditions and particle geometry critically shape pyrolysis dynamics. Together, these findings provide a comprehensive framework for guiding reactor design and process optimization in biomass gasification.

Chapter 3

Machine learning for monitoring incineration of sewage sludge

3.1 Description of the case study

The incineration system in the wastewater treatment plant (WWTP) with an average capacity of 4000 kg/hr of dewatered sludge has served as a basis for the present study. The raw wastewater is first passed through the screen and homogenization units. Thereafter, aerobic and anaerobic bio-treatment are carried out in order to remove the contamination of the wastewater. In the last part of the water treatment plant, the mechanically dewatered and compacted sewage sludge (SS) enters the incineration system. The schematic diagram of the incineration system of the plant adopted for the study is shown in Fig. 3.1.

The analyzed system is composed of a rotary dryer, fluidized bed furnace (FBF), condenser, bag filter, scrubber, mixer, and three heat exchangers (HEXs). The moisture of the sludge is absorbed through the super-heated steam, which passes through the rotary dryer. The pre-dried sludge is then burned inside the FBF, while the generated flue gas moves to the heat exchanger (HEX1) to increase the temperature of the steam. The total amount of the absorbed moisture exhausts toward the condenser as excess steam. An air intake (a mixer) controls the flow rate, temperature, and composition of the air before entering HEX2. Later on, the flue gas is directed to HEX3 for preheating the combustion air supplied to the fluidized bed. The exhausts heat the ambient air in HEX3 and move towards the bag filter followed by the scrubber. The concentrations of the hazardous materials in the fumes are reduced before exiting the environment via the chimney.

To reduce the number of input parameters (variables), for the purpose of the analysis, the considered system configuration is simplified compared to the real facility. In the latter, part of the exhaust gas downstream of HEX3 is sent back to FBF to keep the burning temperature at a required lower level and reduce the flue gas flow through the back filter. Additionally, part of the purified flue gas is directed to HEX3 (instead of air) to cool

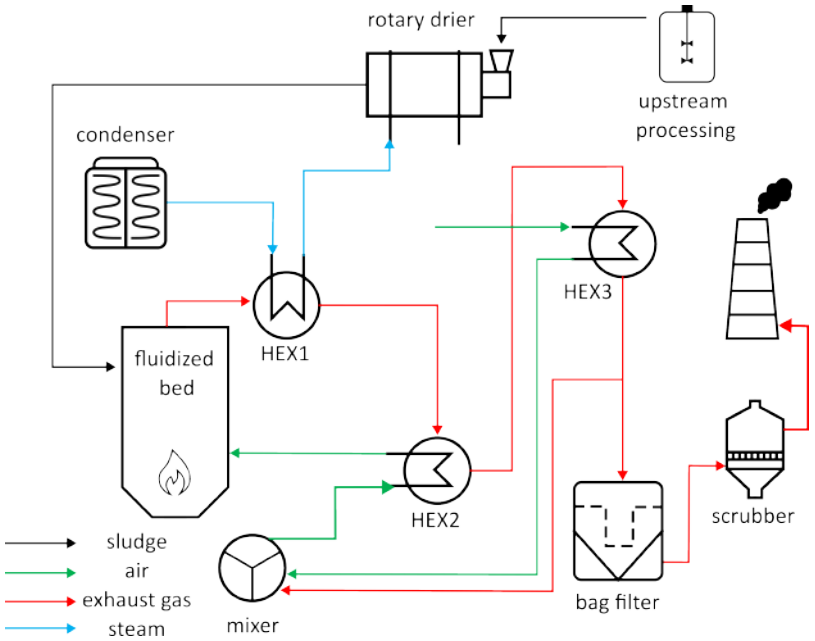

Figure 3.1: An overview of the incineration system.

down hot exhaust gases. Focusing on estimating the usability of ML methods to energy consumption issues, the flue gas recirculation is assumed to be of no relevance to the issues discussed herein.

3.2 Numerical simulation

The analysis of the real-scale sludge thermal treatment system is carried out through ASPEN PLUS, combining various operational units and blocks, including but not limited to the convective dryer and heat exchangers. The principal chemical and physical properties of the SS should be identified to determine its usefulness for the thermal transformation. Numerous factors influence the basic composition of SS, including the concentrations of trace elements and inorganic compounds. Table 3.1 shows an average chemical composition of stabilized dried SS produced in WWTPs in Poland.

Table 3.1: Average composition of SS for Poland (%wt) [64]

Proximate analysis				Ultimate analysis				
Initial Moisture	Volatile	Carbon	Ash	C	H	O	N	P
80 (Dewatered)	71.3	12.43	16.27	29.54	4.47	16.27	3.54	44.74

Figure 3.2 shows the Aspen flowsheet of the modeling procedure for air/steam flow of the incineration system in the water treatment plant for the case studied. It consists of 10 unit operation blocks. The RGibbs block was utilized to simulate the combustion of the

dried sludge in the FBF by minimizing the Gibbs free energy of the system. Different kinds of dryer models containing convective, shortcut, spray, and contact dryer is suggested by Aspen Plus. A convective dryer model is chosen due to the fact that the installed dryer is a rotary type. Numerous industrially produced solid materials with various features are generally dried using the rotary dryer. The heat exchange in HEX1, HEX2, and HEX3 is modeled with HeatX block, wherein in HEX1, heat is transferred between fumes and steam, whereas in the others, between the flue gas and mixed air. Two separators exist in the model used for dividing the steam and air. The absorbed moisture in the dryer is condensed by employing the condenser block. Flow rate and temperature are controlled by mixing three streams, including ambient air, air sucked from the steam scrubber (condenser), and heated air exiting HEX3, which is simulated via a mixer block in ASPEN. Finally, one heat exchanger (SHEX) is modeled via a Heater block to improve the energy performance of the modeled system.

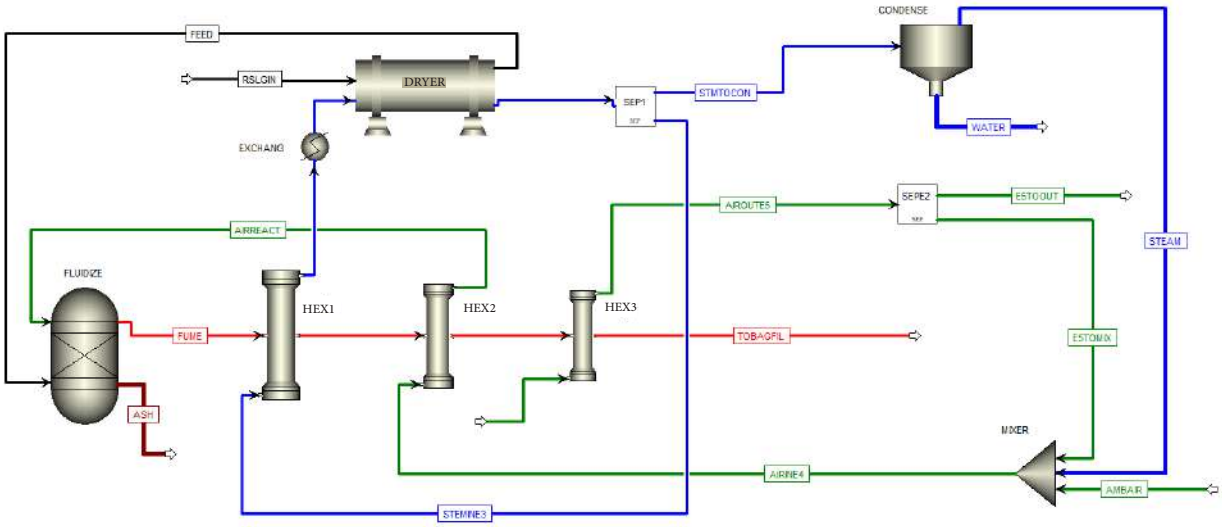

Figure 3.2: Comprehensive Aspen Plus flow sheet for the sludge incineration system [82].

Table 3.2 provides a brief explanation of the incineration system blocks in the ASPEN PLUS flowsheet.

Table 3.2: Description of the ASPEN PLUS model block

Block ID	Aspen Block	description
FBF	RGibbs	Equilibrium modeling based on the minimization of the Gibbs free energy
Dryer	Convective dryer	Reduce sludge moisture content by defined stoichiometric reaction
HEX1	HeatX	Steam superheating
HEX2, HEX3	HeatX	Preheating air for combustion
SepSteam	Separator	Separation of moisture absorbed in a dryer
Condenser	Condenser	Steam condensing process
MixairE2	Mixer	Controlling flow rate and temperature of air stream to HEX2
SHEX	Heater	Controlling steam temperature before dryer

3.2.1 Model assumptions

Based on the nature of Aspen Plus and the thermodynamic model, the following assumptions are made in developing the simulation model:

- The moisture of the sludge while entering the incineration part is assumed to be 80%.
- Heat loss in a fluidized bed furnace and heat exchangers are neglected.
- The range of the particle size distribution mesh of the sludge entering the dryer is between 4 and 10 mm.
- Critical solids moisture and equilibrium solid moisture content is 0.1 and 0.05, respectively.

3.2.2 Validation

The ASPEN PLUS simulation model of the incineration facility under consideration is validated by the available data reported for the existing real-scale incineration system in WWTP. For this purpose, the system characteristics (input flows) given in Table 3.3 were used for the ASPEN simulation to calculate the temperature of flue gas stream exiting the furnace (FBF), the steam outlet temperature of HEX1, and the air outlet temperature of HEX2. A good agreement between the simulation results and the system was obtained, as shown in Table 3.4. This validation provided a reliable model for generating a data-set of the design characteristics of the system.

Table 3.3: System input flows at operating condition

Item	Unit	Design value
SS	Mass Flow rate (kg/hr)	4000
Steam in Dryer	Mass Flow rate (kg/hr)	12000
Steam in Dryer	Temperature (°C)	525
Flue gas from HEX1	Temperature (°C)	497
Flue gas from HEX2	Temperature (°C)	273
Mixed air into HEX2	Flow rate (m^3/hr)	15450

Table 3.4: Numerical simulation and system values

	Numerical Analysis	**System**	**Error(%)**
Fume temperature (FBF)	833.36	863	3.5
Steam outlet temperature (HEX1)	215	200	7
Air outlet temperature (HEX2)	295	300	1.7

As ASPEN simulations are time-consuming it is not possible to examine all the possible combinations of the system designing variables, thus developing an ML model that is

a proper representation of the system can provide the chance for checking many different design parameters within a few minutes. Taking the advantage of a comparative study along with the optimization of the energy performance of SS system, the aforementioned challenges in the WWTP were tackled by developing and sophisticating three different ML techniques, namely Parallel (SVM, GBM, and RF), ANN, and chained algorithm to predict the temperature in fluidized bed (TFB), steam heat transfer rate (SHTR), and dryer residence time (DRT), comprising the target values of the existing SS thermal treatment system. First, the numerical simulation of this system was carried out inside the ASPEN PLUS software, followed by the validation through a real system. Then, ASPEN PLUS simulations were utilized for different SS system characteristics to generate the data-rich framework. Next, multi-output individual ML models are employed to predict the aforementioned target values. Finally, the optimization technique (Brute-force search) was utilized to achieve the values of the SS characteristics associated with the optimum desired heat transfer and dryer residence time. The developed hybrid model could be employed in various incineration systems in water treatment plants in Europe, since they almost operate on a similar cycle and within the same standard.

3.3 Data generation and preprocessing

A data-rich framework is constructed through a total of 76 simulation results obtained by the ASPEN PLUS. For each simulation, particular characteristics of the system were changed within an actual possible range (real system limitations) of available plant components. The aim is to generate a dataset with a wider range of system parameters that later on will be used for finding the optimal parameters of the system. Although the ASPEN simulation calculates flow parameters in all components of the plant, only 10 features were considered in the present study. These key features are either target variables (need to be optimized) or actual inputs (can be changed by plant operators) including: (i) feed temperature (the temperature of the pre-dried sludge which is fed into the fluidized bed), (ii) air temperature (HEX2) (the temperature of the mixed air which enters HEX2), (iii) flue gas temperature (HEX1) (the temperature of the fumes exiting from HEX1), (iv) steam flowrate (HEX1) (the flowrate of the steam which enters HEX1), (v) feed moisture content (the percentage of the moisture in a sludge after being dried), (vi) inlet steam temperature to the dryer (the temperature of the steam supplied to the dryer), (vii) air flowrate (HEX2) (the volume flowrate of the mixed air entering HEX2), and 3 outputs: temperature in a fluidized bed furnace (the temperature of the fumes exiting from the furnace), steam heat transfer (the heat transferred from the steam in the exchanger before the dryer), dryer residence time (the time required for drying the sludge). After consulting with plant operation team, 76 simulations (which are possible to implement) were conducted to get the data-set framework (a detailed list of the parameters obtained through the ASPEN PLUS can be found in data

availability section). Table 3.5 provides the statistical parameters of the dataset.

Table 3.5: Description of statistical dataset

	Input							Output		
	FT[a] (°C)	ATE2[b] (°C)	FTE1[c] (°C)	SFE1[d] (m^3/hr)	MF[e] -	STD[f] (°C)	AFE3[g] (m^3/hr)	TFB[h] (°C)	SHTR[i] (kW)	DRT[j] (hr)
Max	80	60	550	15500	0.33	550	16200	1003	276	12.82
Min	30	20	450	10000	0.2	500	12000	810	-367	8
Std	12.56	6.63	24.18	143.12	0.05	17.75	1208	45.34	127	1.07
Mean	74.60	39.40	500	11868	0.27	522	14117	885	-71	10

[a] Feed temperature;
[b] Air temperature (HEX2);
[c] Fume temperature (HEX1)
[d] Steam flowrate (HEX1)
[e] Moisture content in a feed
[f] Steam inlet temperature to dryer
[g] Air flowrate (HEX2)
[h] Temperature in a fluidized bed furnace
[i] Steam heat transfer rate
[j] Dryer residence time

3.4 Machine learning methods

In this section, three different ML algorithms, including parallel, ANN, and chained, applied to predicting the target variables were explained in detail. In the parallel model, the multi-output problem is divided into several single-output models wherein GBM (Fig. 3.3 (a)), RF (Fig. 3.3 (b)), and SVM (Fig. 3.3 (c)) algorithms were tested to choose the most accurate model. Second, the well-known ANN algorithm was described. Finally, a novel chained method was proposed for the prediction of multi-output problems presented in this study.

Gradient Boosting Machine (GBM)

GBM (Fig. 3.3 (a)) is a tree-based machine learning model that could be thought of as a more advanced version of Random Forest (RF). RF itself is an ensemble method for generating decision trees that uses a bootstrap aggregation. It is a non-parametric regression strategy for constructing prediction rules that do not necessitate the specification of an explicit prior assumption on the type of incorporation between the predictor and the

outcome [172]. The essential difference between GBM and RF in ensemble generation is the construction tree approach. New trees are added to the boosting operation in the boosting approach in order to reduce the inaccuracy of target variable prediction. The estimation error decreases when new trees are added to the GBM structure with a continuous learning factor until it reaches the maximum attainable model accuracy [173].

Random Forest (RF)

Ensemble learning is a method that mixes the prediction effects of more than one algorithm to gain a high-quality final output. Random Forest (RF) is an ensemble method that implements a bootstrap aggregation to generate decision trees. The very last output of this algorithm is an aggregation of the prediction of all developed decision trees. This technique enables to consider all data dimensions almost equally and forestalls trees from coming to be extremely correlated [172].

Support Vector Machine (SVM)

Pioneer work of [174] introduced the statistical learning theory, which led to the Support Vector Machine (SVM) technique that is a supervised learning model. The principles of optimum class separation underpin SVM classification algorithms. It efficiently deals with various types of classification problems, such as material modeling [175], medical assessments [176], and transportation sectors [177]. In this method, the best classifier with the shortest distance between the nearest patterns in each class is sought. Employing the kernel approaches, SVM sensitively identifies non-linear decision surfaces without having knowledge of the transformation procedure to translate the patterns from the input space to a higher-dimensional space. The SVM technique builds a model from the training data and assigns new data to a class using the hyperplane in a higher-dimensional space that is placed at a maximum distance from the labeled classes in order to reduce observed training and generalized errors and gain generalized performance. The kernel coefficient (γ) and the regularization parameter (C) are two highly connected parameters that influence the model complexity of SVM. The model's optimization is accomplished by adjusting these two parameters at the same time. Linear SVM is utilized in this study. In the linear form of SVM, a set of samples $\{x_i, y_i\}_{i=1}^{n}$ is given. The training samples are $\mathrm{x}_i \in \mathbb{R}^l$ (l-dimensional real spaces) and their associated labels $\mathrm{y}_i \in \{+1,\text{-}1\}$. As stated, a decision hyperplane is determined through the SVM (l and n are the numbers of features and samples). The hyperplane, $h(x) = w^T.x + b$ for $w \in \mathbb{R}^l$ is formulated in order to maximize the margin between different classes as represented in Fig. 3.3 (c). The b and w represent the bias and normal vector to the hyperplane as decision variables, respectively. The data classes could be categorized correctly via a sufficient classifier that provides high precision.

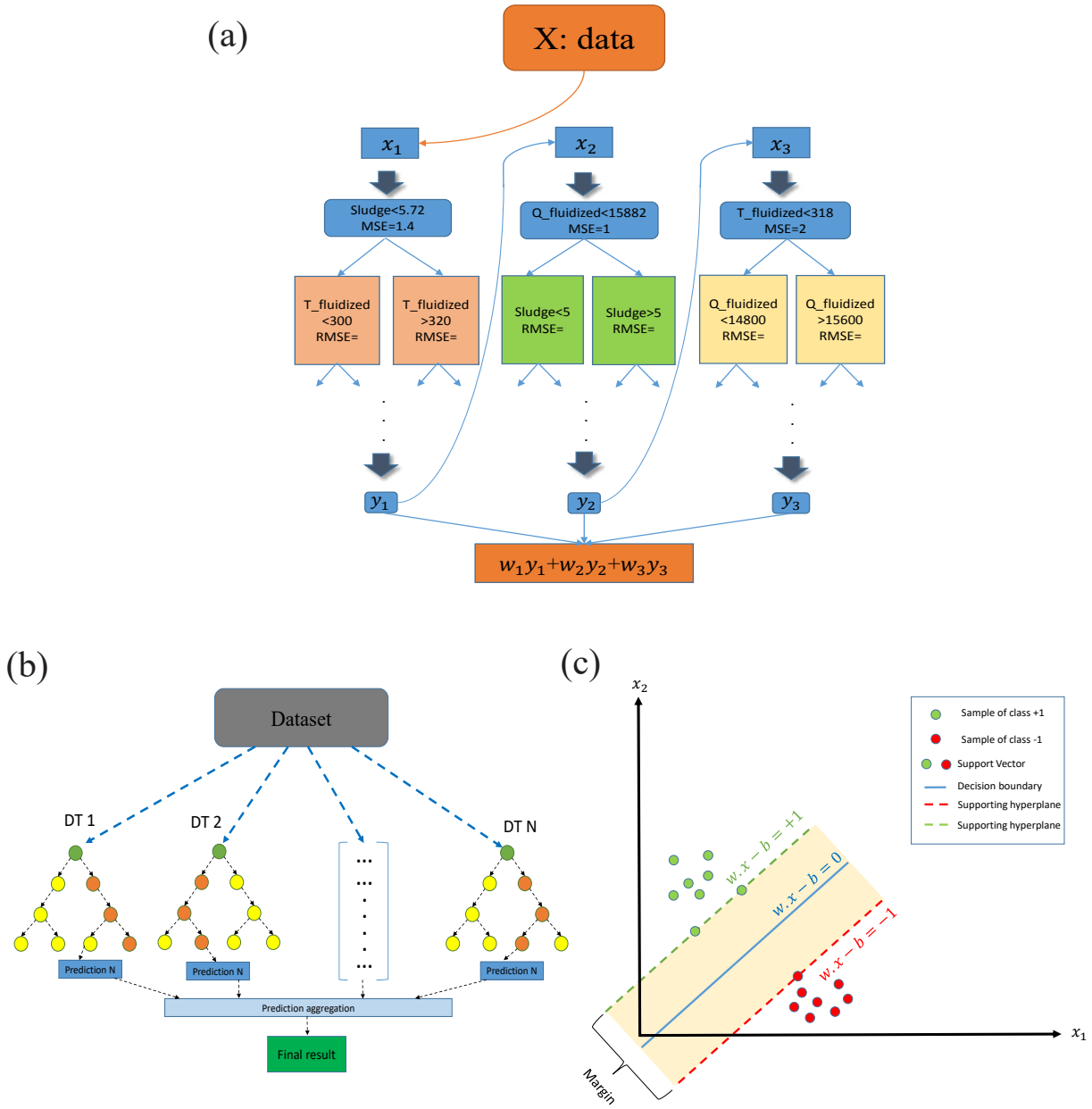

Figure 3.3: Schematic view of three ML models utilized inside parallel model (a) GBM, (b) RF, (c) SVM, [82].

Parallel structure

To develop a multi-output regression model, one of the simplest approaches is to divide the multi-output problem into several single-output models. This structure is called the direct (parallel) method. As shown in Fig. 3.4, one instance of the provided model (RF or GBM, or SVM) receives all the independent variables (X) and predicts one output (Y1 or

Y2 or Y3) per ML model. Although this structure is the simplest one, it can be considered a performance baseline. In this method, the correlation between dependent parameters is ignored. Several types of ML algorithms have been tested, such as SVM, RF, and GBM, as instances of this structure. Finally, GBM instances were chosen for all the separate ML models (for each output).

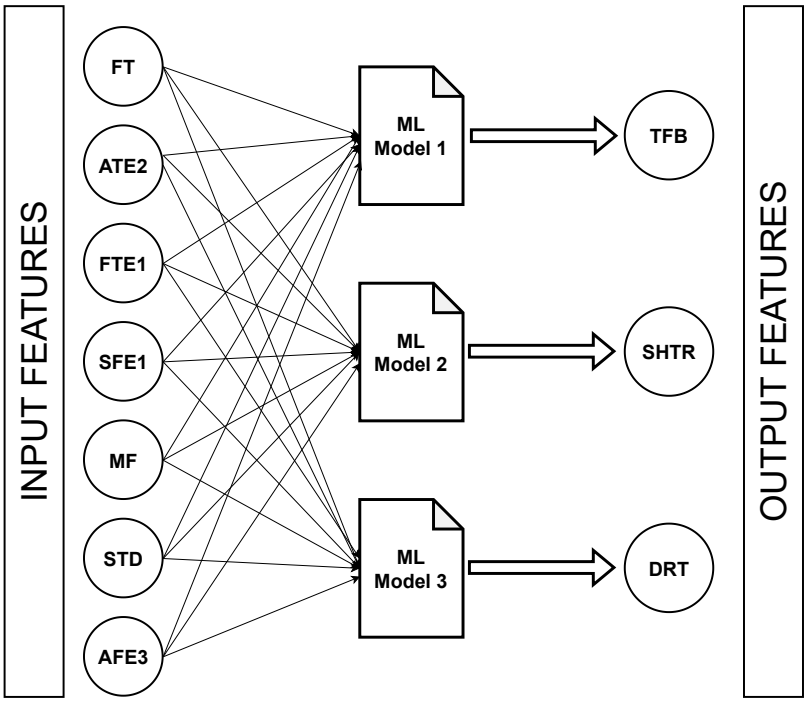

Figure 3.4: Schematic view of the parallel technique [82]; the symbols used are provided in Table 3.5.

Artificial Neural Network (ANN)

Imitating the human nervous system, the ANN, as a modeling approach, is employed to predict the non-linear transformation between input and output data [178]. An extensive number of neural network models employ backpropagation (BP) networks and BP variants in practical applications of ANNs [179]. Various algorithms have been developed in order to predict the target values through the ANN technique. Those algorithms are but are not limited to the Levenberg-Marquardt algorithm, Stochastic Gradient Descent algorithm (SGD), Quasi-Newton Algorithms, and Conjugate Gradient Back Propagation algorithm. An SGD-based ANN algorithm is utilized in this study through Python programming to train and predict the energy performance of the SS utilization system. This algorithm is computationally fast as it only needs the calculation of a single realization of the gradient at each time step and is conveniently fitted into memory since a single training sample is being

processed by the network [180]. Generally, the objective function, as follows, is required to be minimized:

$$L(\lambda) = \frac{1}{n}\sum_{i=1}^{n} L_i(\lambda), \tag{3.1}$$

wherein the parameter λ that minimizes $L(\lambda)$ is to be estimated. Each summand function L_i is typically associated with the i-th observation in the dataset utilized for training. In SGD, the true gradient of $L(\lambda)$ is approximated via a gradient in a one example:

$$\lambda := \lambda - \eta \nabla L_i(\lambda), \tag{3.2}$$

in which η represents the learning rate. The algorithm executes the aforementioned update for each training example as it sweeps across the training set. Several passes over the training set can be performed until the algorithm converges [181]. Thereafter, to avoid cycles, the data can be shuffled after each pass. In most cases, an adaptive learning rate is used to ensure that the algorithm converges. As I was using the AutoKeras library, then an early stop function was utilized. The goal of the training is to minimize the loss. With this, the metric to be monitored would be 'loss', and the mode would be 'min'. A model.fit() training loop will check at end of every epoch whether the loss is no longer decreasing. Once it is found to no longer decrease, model.stop_training is marked True and the training terminates. The structure of the ANN model is represented in Fig. 3.7.

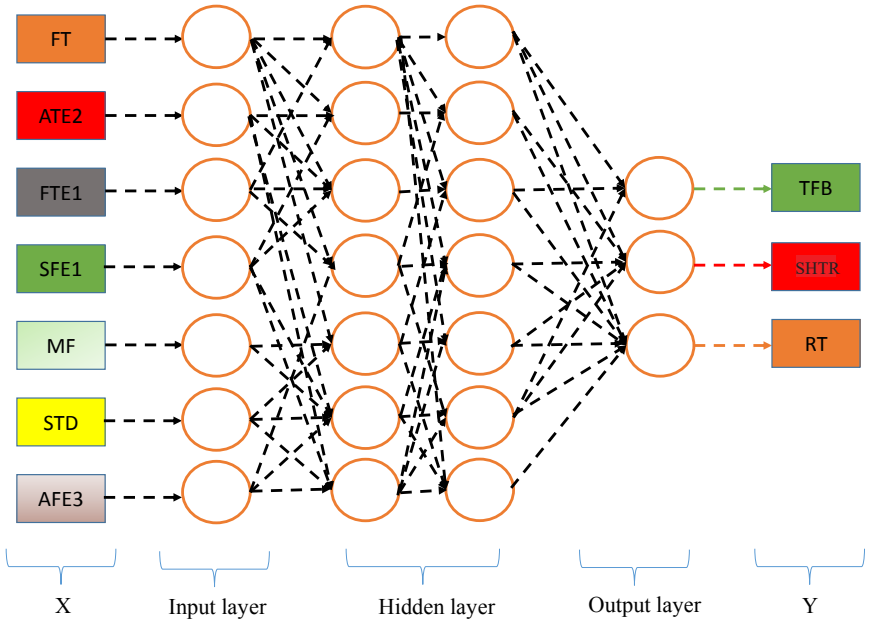

Figure 3.5: Schematic view of the ANN model [82]; the symbols used are provided in Table 3.5.

Chained algorithm

Another efficient model structure (Chained) is developed in the present study to capture the correlation between the dependent variables (output targets) for tackling the multi-output challenge. As shown in Fig. 3.6(a), this structure consists of three ML models (each output feature is dedicated to one model), which are trained by the train set (real values). All independent features (X) and one target feature (Y1) are used to train the first ML model (GBM1). For the training process, the second model (GBM2) received (X+Y1) and (Y2), and the last model received (X+Y1+Y2) and (Y3) for the training phase. Thus, GBM2 and GBM3 can benefit from more data. The chained process increases the prediction accuracy by considering the correlation between several outputs.

As represented in Fig. 3.6(b), the input test independent features (X) are given to the GBM1 and the predicted output (Y1-hat) is collected from this ML model. Furthermore, ($\hat{Y_1}$) was concatenated with X and all were given to the GBM2. Finally, GBM3 receives (X+$\hat{Y_1}$+$\hat{Y_2}$) as input and makes predictions for the last output feature ($\hat{Y_3}$) in the chained process. The model metrics for various chain combinations are provided in Table 3.8.

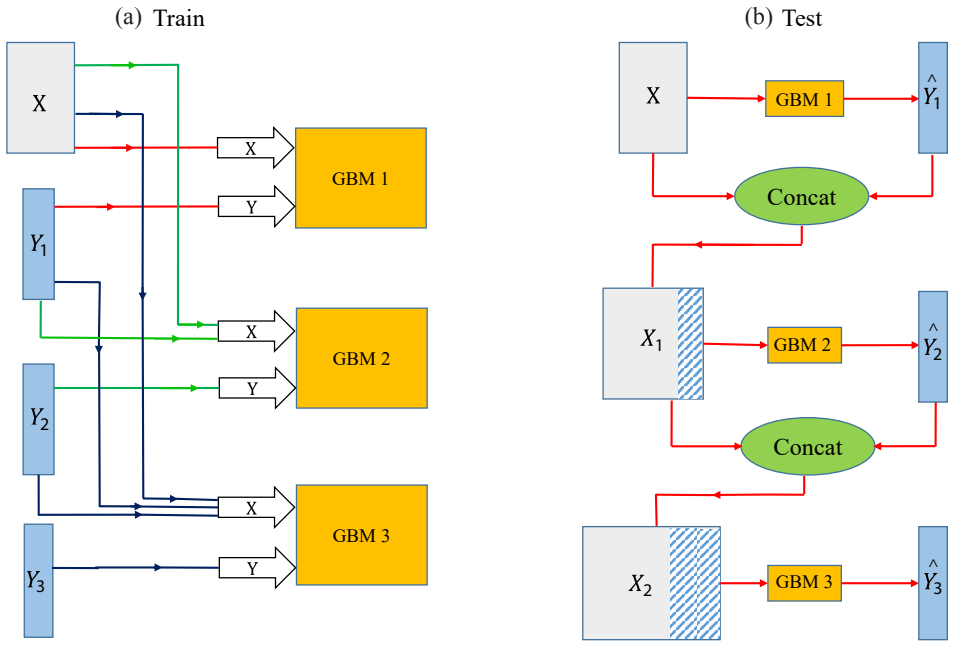

Figure 3.6: Schematic view of the Chained model [82].

Machine learning inference is the process of running data points into a machine learning model to calculate an output, such as a single numerical score. The system used for achieving the inference time for each model was (GeForce GTX 1650 GPU from NVIDIA with 4GB RAM). The inference time for each model was illustrated in Fig. 3.7 and calculated as the time for processing the array of test data set (single batch input). It was shown that the chained and parallel models both outperformed the ANN algorithm in the time required to

get output. The parallel model, due to its simplicity, provided the result sooner than the chained model, though the difference could be considered negligible. The inference time is very important when it is planned to deploy a model for the plant, especially when the model needs to perform in real time on massive input data coming from sensors.

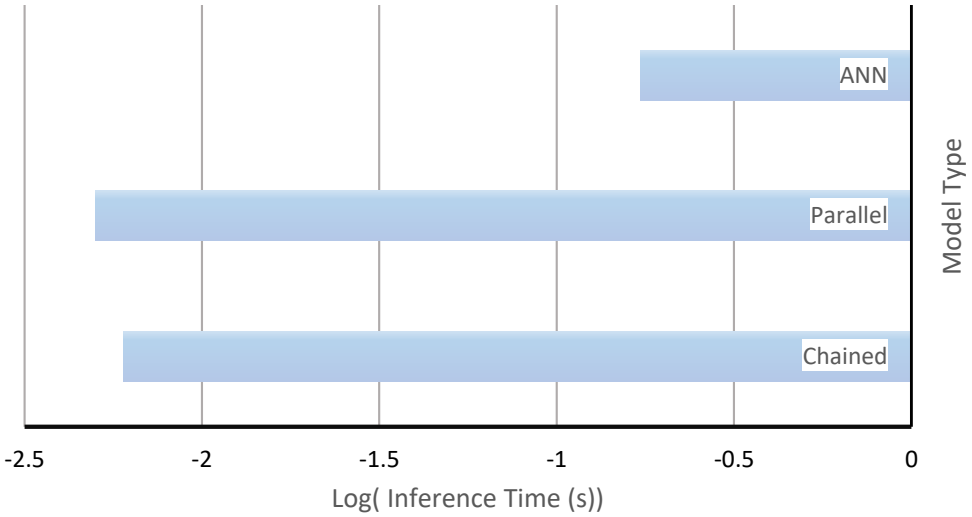

Figure 3.7: The logarithmic inference time for each developed model type [82].

3.5 Feature selection methods

Training an ML model including all the available data generally leads to a decline in model accuracy and overfitting issues. To train ML algorithms efficiently, the redundant and unnecessary features of the data-set should be eliminated. Therefore, feature selection (FS) methods are utilized to omit the redundant dimensions of the data-set while only keeping the most relevant features. The relevancy is associated with the contribution of the feature to increase the ML model accuracy. The linear correlation of variables could be investigated by Pearson correlation (Eq. (3.3)) [182].

$$r = \frac{\sum (x_i - \bar{x})\,(y_i - \bar{y})}{\sqrt{\sum (x_i - \bar{x})^2 (y_i - \bar{y})^2}}, \tag{3.3}$$

wherein r, x_i, $\bar{x}$, y_i, $\bar{y}$ are the correlation coefficient, values of the x-variable in a sample, mean of the values of x-variable, values of the y-variable in a sample, and mean of the values of y-variable, respectively.

3.5.1 Model metrics

Several common methods have been implemented to measure the quality of the machine learning models. These methods (model metrics) show how accurate the model prediction is

in different conditions, i.e. on test data set. Among those, the Mean Squared Error (MSE), Mean Absolute Error (MAE), and Coefficient of Determination (R^2) are considered for this study.

$$\mathrm{MSE} = \frac{1}{n}\sum_{i=1}^{n}(a_i - p_i)^2 \tag{3.4}$$

$$\mathrm{MAE} = \frac{1}{n}\sum_{i=1}^{n} \mid a_i - p_i \mid, \tag{3.5}$$

$$\mathrm{R}^2 = 1 - \frac{\sum(a_i - p_i)^2}{(a_i - \mu_a)^2}, \tag{3.6}$$

where $i = 1, 2, ..n$ is the number of observations, and n is the total number of records. Also, a_i, p_i, and μ_a are output, real values, and a mean value, respectively.

3.6 Results and discussion

The results of a comparative study between three proposed ML approaches are provided and the best method was identified. Thereafter, the parametric study is provided to investigate the influence of the chosen parameters on the target variables. Finally, the optimization technique was explained to choose the optimum solution for the energy performance of the SS treatment system and the corresponding values were provided. It is worth mentioning that for DT, RF, and GBM the normalization process is not necessary generally. Accordingly, for the neural networks, normalization was not utilized since a customized layer exists in this library, which handles the normalization process itself.

3.6.1 Comparative study

In the present study, from the total of 76 data records, around 61 data records were utilized as a training set, while others were for testing for all the proposed models. With a 5-fold cross-validation approach, the selection of training and test sets was changed and model metrics were calculated by averaging the result of each fold.

Table 3.6 shows the model metrics for the parallel method for each output. The average correlation coefficient for each technique is also provided for comparison purposes. The GBM algorithm provides a more accurate prediction of target values than other models, following the RF and SVM, with the R^2 of 0.85, 0.78, and 0.63, respectively. The overall prediction of the SVM algorithm is weak, which is possibly due to the overlapping of the target classes.

Table 3.6: Model metrics for the parallel method leader board

		Hyper_parameters					Train				Test				
Model	Output	ne[a]	lr[b]	msf[c]	mss[d]	md[e]	R^2	MAE	MSE	RMSE	R^2	MAE	MSE	RMSE	R^2_{avg}
GBM	TFB	40000	0.01	1	2	1	0.99	2.6	15	3.873	0.87	7.17	131	11.45	**0.85**
	SHTR	3000	0.01	1	2	1	0.98	11	277	16.64	0.75	29	3354	57.91	
	DRT	5000	0.01	3	2	2	0.99	0.01	0	0	0.94	0.11	0.02	0.14	
RF	TFB	120	-	1	2	None	0.97	4.6	56	7.5	0.77	12.6	360	18.97	0.78
	SHTR	650	-	1	2	None	0.96	15	579	24.1	0.7	41	3862	62.14	
	DRT	500	-	1	2	None	0.98	0.08	0.01	0.1	0.88	0.23	0.1	0.32	
SVM	TFB	-	-	-	-	-	0	824	68167	261.1	0	850	68180	261.11	0.63
	SHTR	-	-	-	-		0.35	83	10373	101.8	0.32	87	10739	103.63	
	DRT	-	-	-	-	-	0.92	16	0.08	0.283	0.88	18	10	3.16	

[a] n_estimator
[b] learning_rate
[c] min_samples_leaf
[d] mean_samples_split
[e] max_depth

The ANN leader board framework for five different ANN models is provided in Table 3.7. ANN-II (bold) shows the highest correlation coefficient with R^2=0.95. Thus this model is chosen for conducting a comparative study. Even though the other proposed ANN could also predict the target variables with acceptable accuracy. The worst ANN model is comparable with the GBM model proposed in the parallel model.
The model metrics for different chain combinations are shown in Table 3.8. The combination of SHTR for Y_1, DRT for Y_2 and TFB for Y_3 (case No. 6) provided the most accurate model among other combinations with the R^2=0.91. The worst scenario is assigned for the combination of TFB for Y_1, DRT for Y_2, and SHTR for Y_3 (case No. 3) with the R^2=0.87.

As represented in Fig. 3.8, the Pearson correlation suggested that the strongest negative correlation is between the SFE1 and DRT, while the highest positive relation is between SFE1 and SHTR. It should be highlighted that since the correlation between features was between -0.8 and 0.8, discerning the patterns between data features was such a complicated task to be processed by engineers. Thus, ML could be a very useful and efficient tool for the prediction of the target values (TFB, SHTR, and DRT).

For comparing the distribution of the errors, Fig. 3.9 shows the normalized error for all models for three different outputs. The normalization was performed for each output separately. Regarding TFB, the error range of the Parallel model is closely distributed near the zero line (red line) around [0.2,0.4], while the Chained model distribution of errors is in different ranges, and ANN errors are between 0.2 and 0.6. Thus, the Parallel model had a better performance on TFB. Concerning SHTR, the Parallel and Chained model error distribution is identical, as it was selected for the first input for the chained model. Error

Table 3.7: ANN leader board architecture

		Train			Test		
Model	Description	R^2	MAE	RMSE	R^2	MAE	RMSE
ANN-I	MCE(7), Dens(1024), ReLu(1024) ReLu(32), Dens(32) Dens(64), ReLu(64), `regression_head_1(3)`	0.99	5.48	11.13	0.92	11.68	28.83
ANN-II	**MCE(7), Dens(32), ReLu(32) Dens(512), ReLu(512) Dens(32) , ReLu(32), regression_head_1(3)**	**1**	**7.96**	**2.82**	**0.94**	**8.35**	**21.07**
ANN-III	MCE(7) Dens(512), ReLu(512) DropOut(512), `regression_head_1(3)`	0.97	7.83	15.67	0.92	11.98	27.23
ANN-IV	MCE(7), Dens(512) ReLu(512), Dens(64) ReLu(64), `regression_head_1(3)`	1	1.04	2.19	0.93	8.83	22.15
ANN-V	MCE(7) , Dens(32) ReLu(32), Dens(512) , ReLu(512) DropOut(512), `regression_head_1(3)`	0.99	5.42	10.51	0.92	10.95	24.49

Table 3.8: Model metrics for various chain combinations

	Model combinations			Test set			
Case	Y_1	Y_2	Y_3	R^2 for Y_1	R^2 for Y_2	R^2 for Y_3	R^2_{avg}
1	TFB	SHTR	DRT	0.87	0.84	0.97	0.89
2	SHTR	TFB	DRT	0.75	0.91	0.96	0.87
3	TFB	DRT	SHTR	0.87	0.96	0.78	0.87
4	DRT	SHTR	TFB	0.94	0.88	0.78	0.88
5	DRT	TFB	SHTR	0.94	0.95	0.46	0.79
6	**SHTR**	**DRT**	**TFB**	0.75	0.98	0.97	**0.91**

concentration for SHTR prediction via ANN is considerably around the zero line. DRT prediction was the most difficult target, and while the ANN error range is mostly higher than zero line, the Parallel model errors are distributed over the ranges. Nevertheless, as the DRT prediction was the last target in the Chained model, it has slightly more errors (error is accumulated in the process).

The most crucial feature of an ML model is its capability of analysing and understanding data instead of memorizing it. Hence, the test set performance of these models is more important than the training and validation sets. Figure 3.10 shows the predicted versus real values for the testing (colored points) dataset of three outputs for ANN (blue points), chained (red points), and parallel (green points) in order to evaluate the performance of each

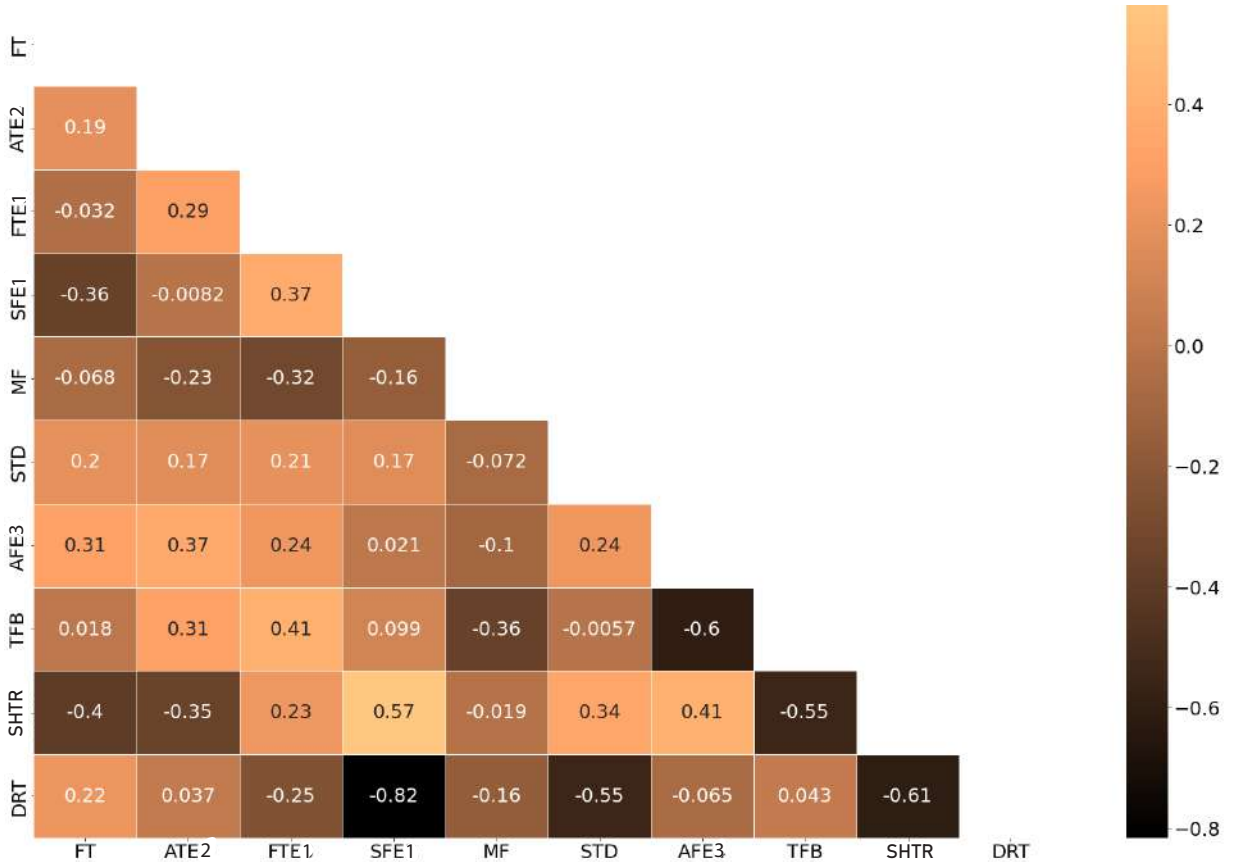

Figure 3.8: Pearson correlation heat map [82].

model. The predictive performance of each model is evaluated for each output separately. Accordingly, whisker plots that show the absolute error for each model are represented.

3.6.2 Parametric studies and sensitivity analysis

Since the proposed chained model is able to predict the target values (TFB, SHTR, and DRT) accurately enough in a short time period, a parametric study is carried out to investigate the effect of the selected parameters on the outputs based on the predictions given by the chained model. Some of the independent variables are maintained fixed while others are modified according to their feasible range of values to generate the 3D graphs. Table 3.9 outlines the parametric research carried out in the present study, wherein different factors were fixed while the remaining factors varied with each trial (PS: Goal variable, VP: Varying parameter).

Figures 3.11 (a,b) show the effect of ATE2, FTE1, MF, and AFE3 on the temperature in the fluidized bed furnace. The HEX2 supplies the air required for the combustion of the sludge, thus, an increase in the flue gas temperature (outlet of HEX1) and air temperature (inlet to HEX2) corresponds with higher temperatures predicted for air supplied to the

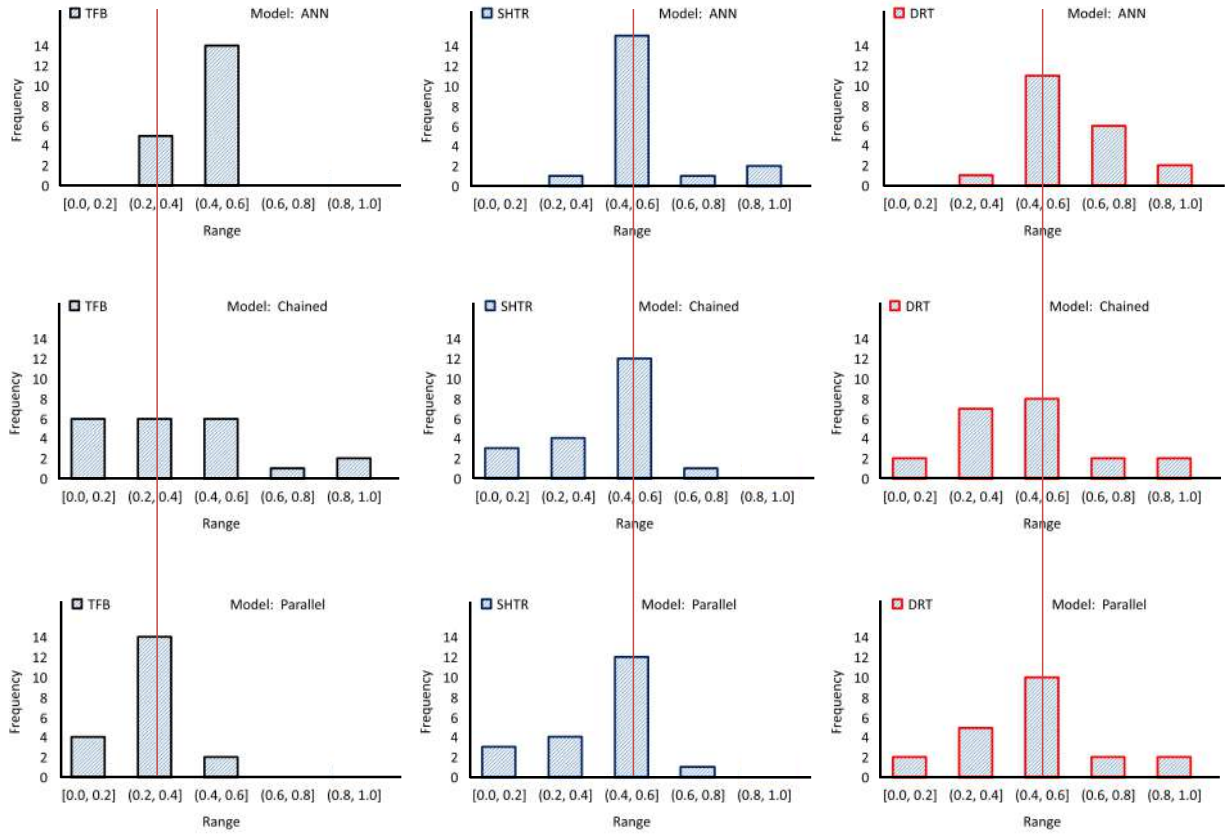

Figure 3.9: Error histogram [82].

Table 3.9: Summary of parametric study

Study No.	Parameters									
	DRT	SHTR	TFB	FTE1	ATE2	AFE3	SFE1	MF	STD	FT
1	-	-	PS	VP	VP	14000	12000	0.28	520	50
2	-	-	PS	500	40	VP	12000	VP	525	80
3	PS	-	-	VP	40	14000	VP	0.28	520	50
4	PS	-	-	500	40	14400	12000	VP	VP	80
5	-	PS	-	500	VP	14000	VP	0.28	520	50
6	-	PS	-	500	40	VP	12000	0.2727	VP	80

fluidized bed, thereby leading to higher TFB values. On the other hand, the moisture content of sludge inversely affects the combustion temperature both in lower and higher airflow entering the fluidized bed. The observed tendency follows from the fact that the high excess-air number (real-to-stoichiometric air ratio) and increased moisture fraction in the fuel decrease the combustion temperature. It is interesting that for lower AFE3 values, the effect of MF on TFB is more highlighted than for higher AFE3. This may be due to the larger water-to-combustion air volume ratio in lower AFE3s with respect to the higher AFE3s.

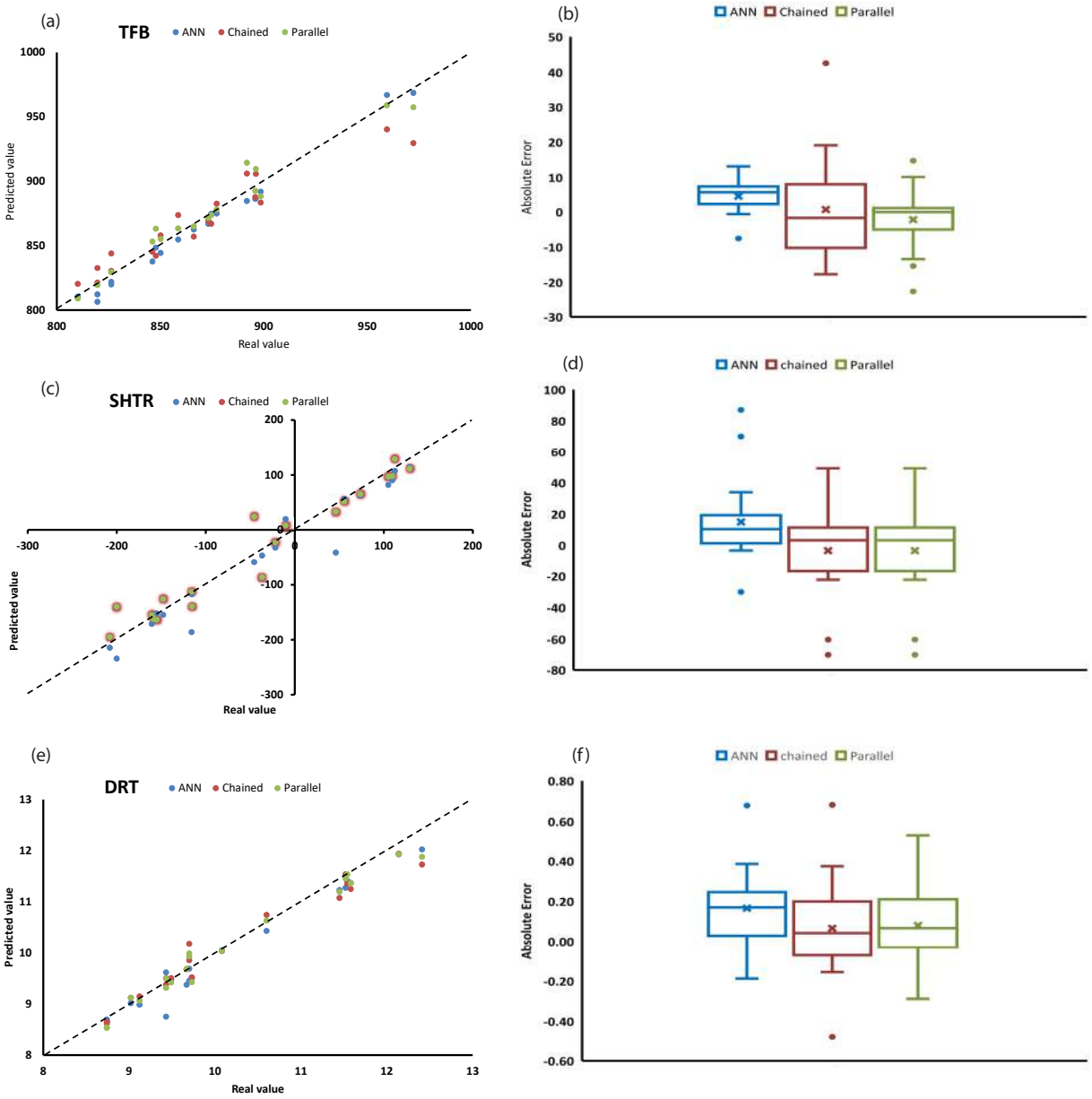

Figure 3.10: Real vs. predicted values: (a) TFB, (b) SHTR, (c) DRT, and whisker plots for TFB (d), SHTR (e), DRT (f), [82].

Figures 3.12(a,b) illustrate the effect of FTE1, SFE1, MF, and STD on the dryer residence time. The time required for the sludge to be dried depends upon the volume and temperature of the flow steam passing through the dryer. It should be highlighted that the sludge residence time in the dryer is decreased while the HEX1 outlet fume temperature increases since the temperature difference of fumes between the inlet and outlet of HEX1 becomes larger and results in higher steam temperature at the outlet from HEX1. It is

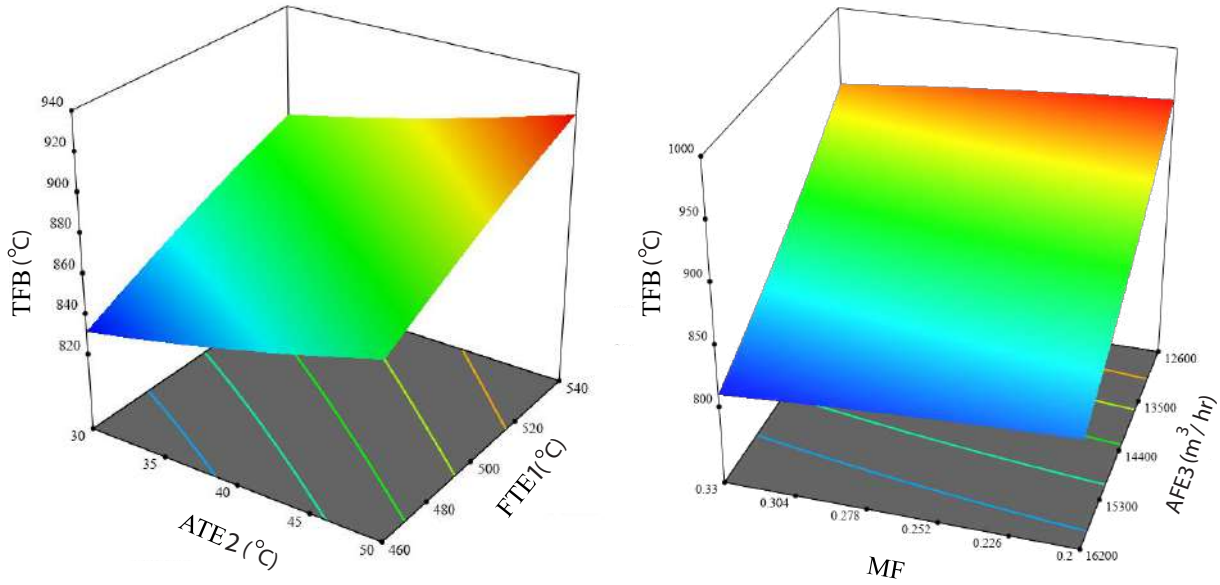

(a) (b)

Figure 3.11: Effect of (a) FTE1 and ATE2, (b) MF and AFE3, on TFB, [82].

obvious, Fig. 3.12(b), that with the rise in the inlet steam temperature (STD), the dryer residence time decreases. Similarly, the higher assumed moisture content in the sludge leaving the dryer translates into a shorter time required for the drying process. Considering the fact that the moisture content of the sludge entering the dryer is constant (initial moisture = 80%), it takes less time for the sludge to be dried while reaching larger values of MF than the smaller ones.

Figures 3.13(a,b) represent the impact of ATE2, SFE1, and STD, AFE3 on the steam heat transfer rate. An increase in the temperature of the input airflow (to HEX2) results in a higher temperature of the flue gas, which moves to HEX2 and thereby leads to a higher temperature of superheated steam exiting HEX2. As a result, the value of a heat transfer rate is enhanced. Obviously, as the volume flow rate of steam increases, the outlet temperature of steam (HEX2) decreases. Hence, the heat transfer rate required for the steam to reach the needed temperature (STD=520°C in this case) begins to change from negative to positive values. Steam heat transfer rates shift towards positive values with increasing temperature of the exchange. As the amount of air supplied to the combustion chamber increases, the flue gas temperature decreases, which causes the steam in HEX1 to absorb less heat. For lower values of AFE3, the steam heat transfer rate is negative, while as AFE3 increases, the steam needs to be heated to reach the required temperature.

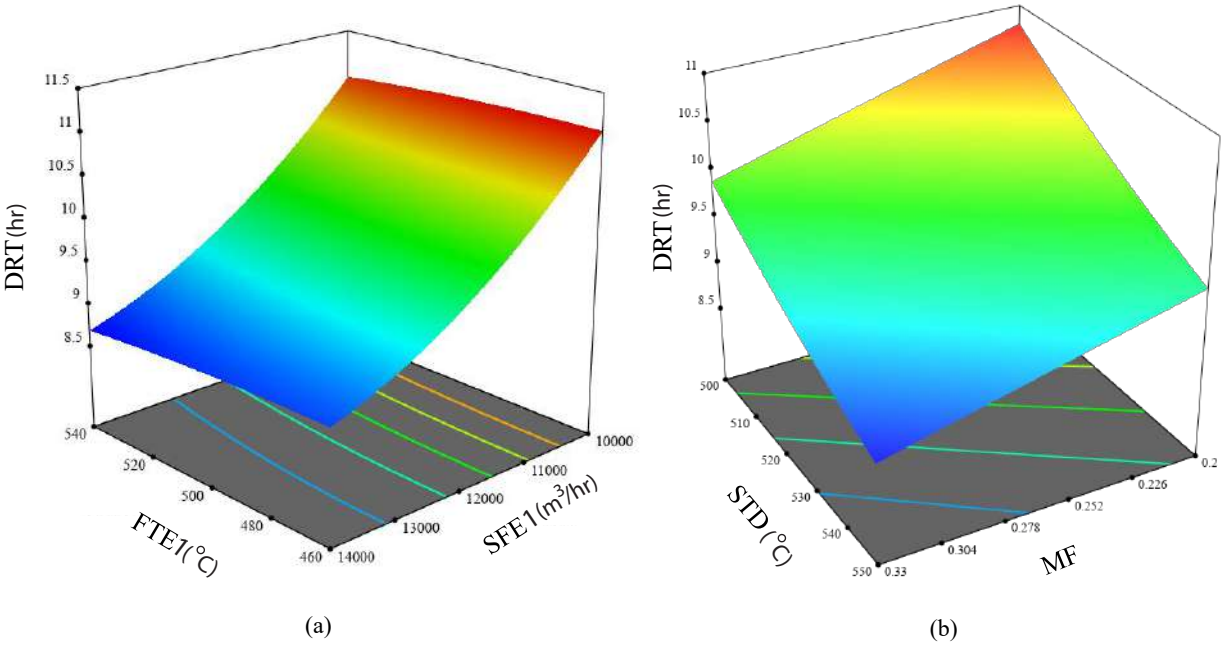

Figure 3.12: Effect of (a) FTE1 and SFE1 (b) MF and STD, on DRT, [82].

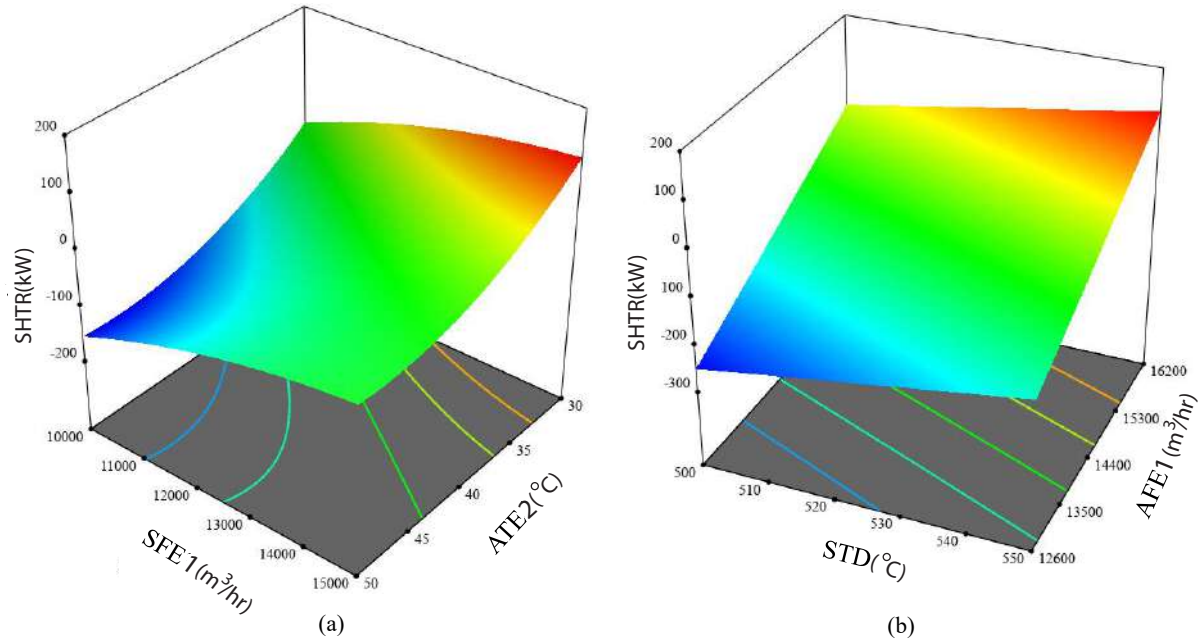

Figure 3.13: Effect of (a) SFE1 and ATE2 (b) AFE3 and STD, on SHTR, [82].

3.6.3 Optimization

Reducing the price of energy has been among the challenging tasks for designers of energy systems. Hence, the maximum efficiency of systems should be calculated. The maximum

achievable energy, which may be utilized for other parts of this cyclical system, e.g. fermentation operational units, for the present case study is obtained. Thereafter, the most optimal operational range of each component of the treatment plant is computed. According to the waste thermal treatment standards that follow the UE regulations regarding the required waste incineration operating parameters [183], as well as the BAT guidelines for reducing NO_x emissions [184], the temperature in the furnace (TFB) should remain between 850 and 950 °C. Similarly, the dryer residence time should not exceed 10 hr considering the size of the dryer and flow rate of sludge. Considering the aforementioned circumstances, a large data-set of potential operational ranges was created (200k records) via Python, after which it is given to the three ML models developed earlier (ANN, chained, and parallel). The chained model was chosen due to the calculation time and accuracy provided for the large dataset utilized in the optimization algorithm. Table 3.10 provides the optimum results given by the chained model. The optimum value of TFB, SHTR, and DRT 890.13 °C, -249.79 kW, and 9.70 hr.

Table 3.10: Optimization results for chained model

Input							Output		
FT (°C)	ATE2 (°C)	FTE1 (°C)	SFE1 (m^3/hr)	MF (%)	STD (°C)	AFE3 (m^3/hr)	TFB (°C)	SHTR (kW)	DRT (hr)
70	50	450	13000	0.32	500	13000	890.13	-249.79	9.70
70	50	450	14000	0.32	500	13000	890.40	-249.79	9.32
70	50	450	14000	0.28	500	13000	897.61	-249.79	9.81
70	50	450	13000	0.3	500	13000	897.93	-249.79	9.71
70	50	450	14000	0.3	500	13000	898.20	-249.79	9.32

3.7 Conclusions

Addressed in this study, is the development of the state-of-the-art robust chained multioutput regression, the ANN approach, and parallel ML techniques (GBM, RF, and SVM) via SciKit-Learn library in Python integrated with the hyper-parameter tuning and k-fold cross-validation method in order to predict the target variables (fluidized bed temperature, steam heat transfer rate, and dryer residence time) of the SS incineration system, on the example of the wastewater treatment plant under operation (Poland). The steam heat transfer rate (heat duty) and fluidized bed temperature of the SS are predicted through three different proposed models. All proposed ML models are validated over a database using four performance measures under 5-fold cross-validation. A comparative study is carried out to select the most accurate method of prediction. The comparisons show the superiority of the ANN and chained algorithms in terms of predictive performance and overall prediction accuracy. It is concluded that the proposed chained model slightly underperforms the ANN model

while predicting the target variables. The R^2 for the chained model is 0.91, while for the ANN 0.95. However, the robustness of this technique was highlighted through the inference time. The inference time for the ANN model (t=0.176 s) is around 28 times longer with respect to the one obtained for the chained algorithm (t=0.006 s). The inference time is an important factor when choosing the best method in the case study utilized in the present research. Also, the worst performance among all the suggested models is associated with the parallel model with $R^2 = 0.85$. Therefore, this model could not be suitable for the prediction of the energy performance of SS.

It is revealed that the steam flowrate has the highest positive and negative correlation with the steam heat transfer rate and dryer residence time, respectively. The effect of air temperature and flowrate on the dryer residence time is negligible. Also, the fuel moisture content has the least influence on the steam heat transfer rate. The effect of the fuel temperature, steam flowrate, and steam temperature on the temperature in the fluidized bed can be neglected, though other target variables are influenced by these inputs.

Finally, the maximum achievable energy is calculated employing the proposed ML techniques, using the data within the operation range of all inputs. It was shown that the chained model suggested the optimum solution with the best accuracy among others. The values of TFB, SHTR, and DRT are 890.13 °C, -249.79 kW, and 9.70 hr, respectively.

Thanks to the chained ML model proposed in this study, not only could the design process of the prospective SS incineration systems become convenient, but also the energy performance of the existing systems could be predicted and optimized by considering input features without dealing with more time-consuming and expensive labor work.

Chapter 4

Closed-loop energy optimization using a real-time digital twin

4.1 Description of a closed-loop incineration system of WWTP

In this chapter, a simplified configuration of the sewage sludge incineration system introduced earlier in Chapter 3 (see Fig. 3.1) is considered to investigate the energy consumption of the plant. As described previously, the installation consists of a rotary dryer, fluidised bed furnace (FBF), condenser, bag filter, scrubber, mixer, and three heat exchangers (HEX1, HEX2, HEX3). The detailed process description of the system is provided in Section 3.1.

Unlike the previous analysis in Chapter 3, which focused on optimization for a representative single hour of operation, the present study extends the investigation to a full 24-hour dataset in order to capture the system's temporal variations. For the present analysis, the focus is on the main operational features that influence energy performance. In particular, the process begins with the removal of sludge moisture in the rotary dryer by means of super-heated steam. The pre-dried sludge is then incinerated in the FBF, and the resulting flue gas is utilised for heat recovery through the three heat exchangers. Hazardous components in the exhaust gases are subsequently reduced in the bag filter and scrubber before discharge into the environment. In addition, biogas generated during anaerobic digestion in the wastewater treatment plant is injected into the fluidised bed when the bed temperature drops due to high sludge moisture or operational fluctuations. This biogas injection serves to stabilise combustion and maintain the required temperature level.

4.2 Methodology

The methodology involves a multi-step process, incorporating data collection, analytical calculations using in-house codes written in Fortran and Python, and simulation modeling in AnyLogic. Schematic explanation of the procedure is presented in Fig. 4.1. In the first step, analytical calculations of flue gas composition and temperature of combustion were conducted. Then, the obtained information, together with the gathered measurement data, were used for further calculations. AnyLogic is a simulation software that combines system dynamics, discrete-event, and agent-based approaches, which allows modeling of both physical processes and operational behavior in engineering systems. The simulation of the wastewater treatment plant was conducted using AnyLogic software, with the main objective of predicting the reactor temperature over a 24-hour period. The model was then validated with the use of the real data gathered in the system of the wastewater treatment plant. The system operating data included the sludge flow rate, biogas flow rate, sludge moisture content, air temperature, steam temperature at the inlet and outlet of heat exchanger No. 3, temperatures of flue gases at the inlets and outlets of heat exchangers 1, 2 and 3. The dataset taken into account in this analysis covers a time frame of 24 hours.

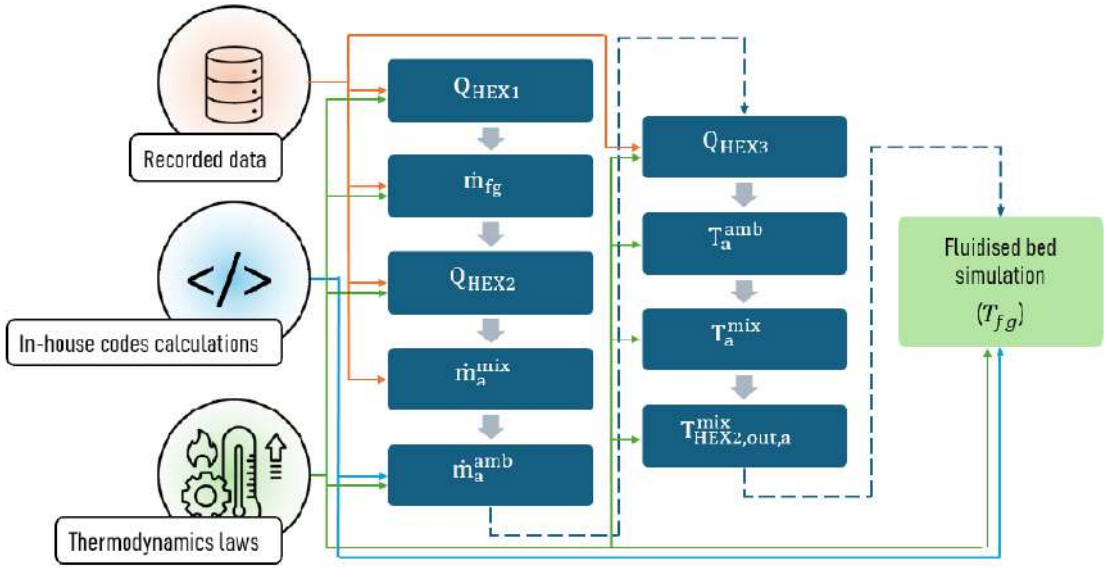

Figure 4.1: Graphical explanation of the performed analysis.

4.3 Analytical calculations

In addition to the acquired data, it was necessary to estimate additional parameters, such as flue gas composition, and combustion temperature, and their influence on the furnace temperature. In the first step, the gas composition and combustion temperature were calculated for three moisture contents of sludge (20%, 30%, and 40%) and three recirculation rates (20%, 30%, and 40%). For each combination of moisture and recirculation rate, the analysis was performed for ten λ (excess-air ratio) values ranging from 1.14 up to 2.38. Then, based on the obtained data, a linear regression model was used in order to estimate a function for the furnace temperature.

4.3.1 Flue gas stream – chemical calculations

To determine the amount of flue gas and composition, chemical calculations were performed considering a global reaction of combustion of sewage sludge. A general empirical formula of $C_xH_yO_zN_q$ for the sludge was assumed with x, y, z, q defined based on the chemical sludge composition. The combustion with air excess was taken into account with the resulting flue gas composed of the basic compounds such as CO_2, H_2O, O_2 and N_2, according to the reaction:

$$C_xH_yO_zN_q + n_{ox}\lambda(O_2 + 3.76N_2) \rightarrow n_{CO_2}CO_2 + n_{H_2O}H_2O + n_{O_2}O_2 + n_{N_2}N_2, \tag{4.1}$$

where n denotes the number of moles and λ is the excess air ratio which is expressed by:

$$\lambda = \frac{1}{AFR}\frac{m_{ox}}{m_{ss,d}}. \tag{4.2}$$

In the above, AFR represents air-to-fuel ratio, m_{ox} and $m_{ss,d}$ stand for the mass of oxidizer and dry sewage sludge, respectively. The resulting flow rate of flue gases $\dot{m}_{fg}$ was determined from the mass balance equation:

$$\dot{m}_{ss}^{in} + \dot{m}_{ox} = \dot{m}_{fg} + \dot{m}_a, \tag{4.3}$$

where $\dot{m}_a$ represents the mass rate of ash.

Knowing the chemical composition of the fuel (sludge), based on the above equations, the amount of CO_2, H_2O, O_2, and N_2, and the flue gas stream were calculated for various configurations of moisture, recirculation rate and excess air ratio.

4.3.2 Combustion temperature

In the sewage sludge combustion system, part of the exhaust gas is recirculated back to the combustion chamber. This is mainly to control the process temperature and keep it at the required level that prevents NO_x emissions. To simulate the process with flue gas

recirculation, the computation method involved two steps. In the first one, the combustion temperature for the process stage with no recirculation was determined as the initial process temperature for the next step. Here, the energy balance for the furnace chamber includes the input energy of: (i) dry sewage sludge ($\dot{Q}_{\mathrm{ss,d}}$), (ii) moisture contained in the sludge ($\dot{Q}_{\mathrm{H_2O}}$), (iii) oxidizer ($\dot{Q}_{\mathrm{ox}}$) and (iv) sludge chemical energy ($\dot{Q}_{\mathrm{ch}}$), and the outflow thermal energy of: (v) flue gas ($\dot{Q}_{\mathrm{fg}}$), (vi) steam ($\dot{Q}^{\mathrm{fg}}_{\mathrm{H_2O}}$) and (vii) removed ash ($\dot{Q}_{\mathrm{a}}$), and is written as

$$\dot{Q}_{\mathrm{ss,d}} + \dot{Q}_{\mathrm{ch}} + \dot{Q}_{\mathrm{H_2O}} + \dot{Q}_{\mathrm{ox}} = \dot{Q}_{\mathrm{fg}} + \dot{Q}^{\mathrm{fg}}_{\mathrm{H_2O}} + \dot{Q}_{\mathrm{a}}, \tag{4.4}$$

where

$$\dot{Q}_{\mathrm{ss,d}} = (\dot{m}c)_{\mathrm{ss,d}}\, T^{in}, \tag{4.5}$$

$$\dot{Q}_{\mathrm{ch}} = \dot{m}_{\mathrm{ss}}\mathrm{HHV}, \tag{4.6}$$

$$\dot{Q}_{\mathrm{H_2O}} = Y_{\mathrm{H_2O}}\dot{m}_{\mathrm{ss}}h_{\mathrm{H_2O}}(T^{in}), \tag{4.7}$$

$$\dot{Q}_{\mathrm{ox}} = \dot{m}_{\mathrm{ox}}\sum_i Y_{i,\mathrm{ox}}h_i(T_{\mathrm{ox}}), \tag{4.8}$$

$$\dot{Q}_{\mathrm{fg}} = \dot{m}_{\mathrm{fg}}\sum_i Y_{i,\mathrm{fg}}h_i(T_{\mathrm{fg}}), \tag{4.9}$$

$$\dot{Q}^{\mathrm{fg}}_{\mathrm{H_2O}} = Y_{\mathrm{H_2O}}\dot{m}_{\mathrm{ss}}h_{\mathrm{H_2O}}(T_{\mathrm{fg}}), \tag{4.10}$$

$$\dot{Q}_{\mathrm{a}} = (1 - Y_{\mathrm{H_2O}})\,\dot{m}_{\mathrm{ss}}c_{\mathrm{a}}(T_{\mathrm{fg}}). \tag{4.11}$$

In the above, $\dot{m}$ stands for the mass flow rate, c is the specific heat, whereas T represents temperature, h is the specific enthalpy, $Y_{\mathrm{H_2O}}$ is the mass fraction of moisture in the sludge at the inlet to the furnace and Y_i is the mass fraction of i-th gas component. Subscripts a, fg, and H_2O represent ash, flue gas, and water/steam, respectively. The quantity HHV is the higher heating value of the sludge. Superscript *in* stands for the inlet parameter value. The enthalpies of compounds were determined using the *RefProp* database [185]. To calculate the combustion temperature sought, the iteration method was applied.

Based on the parameters obtained at the first step, for the set flow rate of a recirculated flue gas $\dot{m}^r_{\mathrm{fg}}$, the composition of an oxidizing gas mixture supplied to the furnace chamber and the resulting flue gas composition were calculated, according to the system of mass balance equations:

$$\dot{m}_{\mathrm{ss}} + \dot{m}_{\mathrm{ox}} + \dot{m}^r_{\mathrm{fg}} = \dot{m}_{\mathrm{fg}} + \dot{m}_{\mathrm{a}}, \tag{4.12}$$

$$\dot{m}_{\mathrm{fg}} = \dot{m}^{out}_{\mathrm{fg}} + \dot{m}^r_{\mathrm{fg}}, \tag{4.13}$$

where *out* refers to the outlet flue gas stream from the combustion system.

The combustion temperature was then recalculated, solving iteratively the modified energy balance for the recirculation-type system, formulated as:

$$\dot{Q}_{\mathrm{ss,d}} + \dot{Q}_{\mathrm{ch}} + \dot{Q}_{\mathrm{H_2O}} + \dot{Q}_{\mathrm{ox}} + \dot{Q}^r_{\mathrm{fg}} = \dot{Q}^{out}_{\mathrm{fg}} + \dot{Q}^{\mathrm{fg}}_{\mathrm{H_2O}} + \dot{Q}_{\mathrm{a}}, \tag{4.14}$$

where $\dot{Q}^{r}_{\mathrm{fg}}$ and $\dot{Q}^{out}_{\mathrm{fg}}$ represent the energy of recirculated and the remaining (outlet) flue gas streams, respectively:

$$\dot{Q}^{r}_{\mathrm{fg}} = \dot{m}^{r}_{\mathrm{fg}} \sum_{i} Y_{i,r} h_i(T_{\mathrm{ox}}), \tag{4.15}$$

$$\dot{Q}^{out}_{\mathrm{fg}} = \dot{m}^{out}_{\mathrm{fg}} \sum_{i} Y_{i,\mathrm{fg}} h_i(T_{\mathrm{fg}}), \tag{4.16}$$

which allowed to calculate the temperature of combustion, needed for the next step of the analysis.

Based on the analytical calculation results, a function describing the furnace temperature was determined. Following the stoichiometric calculations, based on the data gathered in the previous steps, five factors influencing the furnace temperature were established: sludge flow rate ($\dot{m}_{\mathrm{ss}}$), sludge moisture content ($Y_{\mathrm{H_2O}}$), mixed air flow rate ($\dot{m}^{\mathrm{mix}}_{\mathrm{a}}$) and temperature ($T^{\mathrm{mix}}_{\mathrm{a}}$), and the recirculation rate (R). A linear regression model and the Python language were used in order to derive an equation allowing for calculating the furnace temperature for these five factors:

$$\begin{aligned} T_{furnace} = {} & a_1 \cdot \dot{m}_{\mathrm{ss}} + b_1 \cdot \dot{m}^{\mathrm{mix}}_{\mathrm{a}} + c_1 \cdot T^{\mathrm{mix}}_{\mathrm{a}} + d_1 \cdot R + e_1 \cdot Y_{\mathrm{H_2O}} \\ & + a_2 \cdot \dot{m}^{2}_{\mathrm{ss}} + b_2 \cdot (\dot{m}^{\mathrm{mix}}_{\mathrm{a}})^2 + c_2 \cdot (T^{\mathrm{mix}}_{\mathrm{a}})^2 + d_2 \cdot R^2 + e_2 \cdot Y^{2}_{\mathrm{H_2O}} \\ & + f_1 \cdot \dot{m}_{\mathrm{ss}} \cdot \dot{m}^{\mathrm{mix}}_{\mathrm{a}} + f_2 \cdot \dot{m}_{\mathrm{ss}} \cdot T^{\mathrm{mix}}_{\mathrm{a}} + f_3 \cdot \dot{m}_{\mathrm{ss}} \cdot R + f_4 \cdot \dot{m}_{\mathrm{ss}} \cdot Y_{\mathrm{H_2O}} \\ & + f_5 \cdot \dot{m}^{\mathrm{mix}}_{\mathrm{a}} \cdot T^{\mathrm{mix}}_{\mathrm{a}} + f_6 \cdot \dot{m}^{\mathrm{mix}}_{\mathrm{a}} \cdot R + f_7 \cdot \dot{m}^{\mathrm{mix}}_{\mathrm{a}} \cdot Y_{\mathrm{H_2O}} \\ & + f_8 \cdot T^{\mathrm{mix}}_{\mathrm{a}} \cdot R + f_9 \cdot T^{\mathrm{mix}}_{\mathrm{a}} \cdot Y_{\mathrm{H_2O}} + f_{10} \cdot R \cdot Y_{\mathrm{H_2O}} \end{aligned} \tag{4.17}$$

Values of coefficients $a_1 - f_{10}$ can be found in the Appendix. In the further step, the determined function was implemented into the AnyLogic software in order to simulate the wastewater treatment system work in various conditions.

4.4 Dynamic simulation in AnyLogic

Systems of ordinary differential equations and partial differential equations serve as mathematical frameworks, extensively applied in scientific and engineering fields for dynamic system modeling [186, 187]. A governing equation describes the relationships among variables, such as temperature or chemical concentration, representing state variables in a dynamic system. The equations are derived from general empirical observations and specific hypotheses, such as the first law of thermodynamics. However, in real-world systems, formulating governing equations becomes challenging due to the complexity of the system and the simultaneous occurrence of multiple phenomena, leading to uncertainties in existing principles. With advancements in sensor technology, it is now possible to sample data from dynamic systems, opening doors for extracting insights into their physical behavior. This has sparked increased interest in recent years in creating data-driven techniques to

uncover the governing equations behind these dynamic systems [188]. Comprehending the behavior of dynamic systems through data is an important scientific and practical problem, particularly in engineering where testing many scenarios during prototyping is necessary.

In this study, a scenario is examined where the information about the state variables dynamic system, particularly a water treatment plant, is examined over the course of a day. This data forms a series of multiple variables recorded over time.

4.4.1 Modeling in AnyLogic

The procedure of the simulation is presented on the scheme in Fig. 4.2. To initiate the modeling process in AnyLogic, our primary objective is to determine the heat transfer occurring within heat exchanger 1 (HEX1). This involves calculating the mass flow rate of steam entering the heat exchanger. Leveraging recorded data for the inlet and outlet temperatures of HEX1, I can compute the heat transferred between the flue gas and steam ($\dot{Q}_{\mathrm{HEX1}}$) utilizing the equation:

$$\dot{Q}_{\mathrm{HEX1}} = \dot{m}_{\mathrm{st}} \cdot \left(h_{\mathrm{st}}^{out} - h_{\mathrm{st}}^{in}\right), \tag{4.18}$$

where $\dot{m}_{\mathrm{st}}$ denotes the mass flow rate of steam, and h_{st}^{in} and h_{st}^{out} represent the enthalpies of the steam at the inlet and outlet of HEX1, respectively.

To model the enthalpy of steam within the simulation, a linear correlation has been established based on the properties of water at atmospheric pressure $h = 2.0514T + 2465.7$ [189]. The assumption of negligible pressure drop is considered in this correlation. It allows for a simplified yet accurate estimation of enthalpy values without the need for direct table lookup.

In the subsequent step, the mass flow rate of the flue gas is determined by utilising the heat transfer in the heat exchanger. Assuming a constant specific heat for the flue gas ($c_{p,\mathrm{fg}}$), and considering the temperature differences between the outlet and inlet of the flue gas, the mass flow rate of the flue gas can be calculated from:

$$\dot{m}_{\mathrm{fg}} = \frac{\dot{Q}_{\mathrm{HEX1}}}{c_{p,\mathrm{fg}}\left(T_{\mathrm{fg}}^{out} - T_{\mathrm{fg}}^{in}\right)}. \tag{4.19}$$

Moving to the next stage in HEX2, heat transferred in heat exchanger 2 is determined by utilising the previously obtained mass flow rate of the flue gas. By considering the temperatures of the flue gas at the inlet and outlet of HEX2, the heat flow can be calculated using the equation:

$$\dot{Q}_{\mathrm{HEX2}} = \dot{m}_{\mathrm{fg}} c_{p,\mathrm{fg}} \left(T_{\mathrm{fg,HEX2}}^{out} - T_{\mathrm{fg,HEX2}}^{in}\right). \tag{4.20}$$

Next, the mass flow of the mixed air passing through HEX2 and entering the furnace is determined. Initially, the volume flow rate of the mixed air is recorded. To obtain the

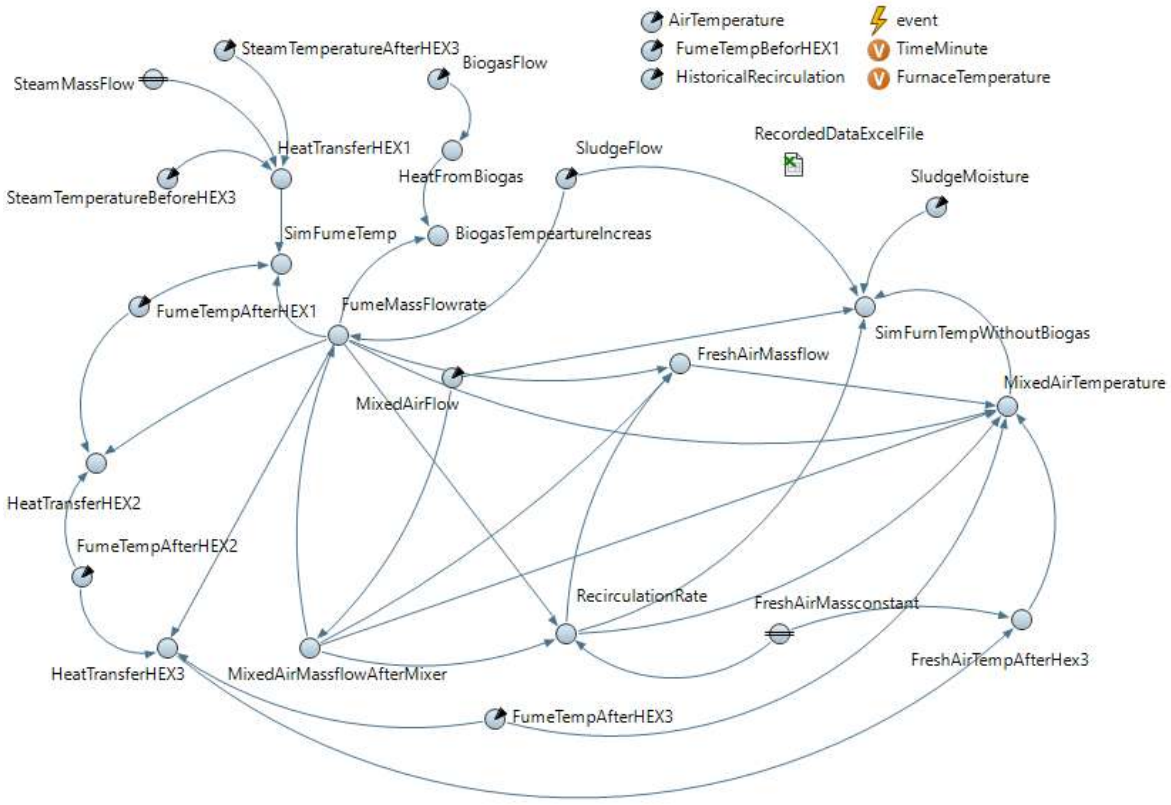

Figure 4.2: Diagram of the simulation procedure

density of the mixed air, an assumption is made that the temperature of the mixed air falls within the range of 200 to 300 °C. With this assumption, the dynamic parameter of mass flow is obtained by multiplying the density of the mixed air with the recorded volume flow rate:

$$\dot{m}_{\mathrm{a}}^{\mathrm{mix}} = \rho_{\mathrm{a}}^{\mathrm{mix}} \dot{V}_{\mathrm{a}}^{\mathrm{mix}}. \tag{4.21}$$

Within the mixer, a portion of the flue gas from HEX3 is combined with the ambient air preheated in HEX3, forming the mixed air stream that enters HEX2. With the known mass flow rates of the mixed air and the flue gas, and considering the recirculation percentage of the flue gas obtained through analytical solution employing the mass conservative equation, the mass flow rate of the ambient air can be determined from the relationship:

$$\dot{m}_{\mathrm{a}}^{\mathrm{amb}} = \dot{m}_{\mathrm{a}}^{\mathrm{mix}} - \left(\frac{R}{100} \cdot \dot{m}_{\mathrm{fg}} \right). \tag{4.22}$$

Further, the temperature of the supplied air after HEX3 is determined using the equation:

$$T^{\text{amb}}_{\text{a,HEX3}} = T_{\text{amb}} + \frac{\dot{Q}_{\text{HEX3}}}{\dot{m}^{\text{amb}}_{\text{a}} \cdot c_{p,\text{a}}}, \tag{4.23}$$

utilizing the thermal output of HEX3 calculated for the known mass flow rate of the flue gas and the inlet and outlet temperatures, given as:

$$\dot{Q}_{\text{HEX3}} = \dot{m}_{\text{fg}} c_{p,\text{fg}} \left(T^{in}_{\text{fg,HEX3}} - T^{out}_{\text{fg,HEX3}} \right), \tag{4.24}$$

and assuming the ambient temperature (T_{amb}) of the air in September at the water treatment plant location is approximately 14°C.

When returning to the mixer, the temperature of the mixed air entering HEX2 is determined. With the known mass flow rate of the mixed air, the mass flow rate of the preheated ambient air along with its temperature after HEX3, the mass flow rate of the flue gas, and the recirculation percentage, energy conservation in the mixer allows for the calculation of the temperature of the mixed air using the equation:

$$\begin{aligned} \dot{m}^{\text{mix}}_{\text{a}} \cdot c^{\text{mix}}_{p,\text{a}} \cdot T^{\text{mix}}_{\text{a}} = \dot{m}^{\text{amb}}_{\text{a}} \cdot c_{p,\text{a}} \cdot T^{\text{amb}}_{\text{a,HEX3}} + \\ \left(1 - \frac{R}{100}\right) \cdot \dot{m}_{\text{fg}} \cdot c_{p,\text{fg}} \cdot T^{out,\text{mix}}_{\text{fg}}. \end{aligned} \tag{4.25}$$

Moving forward to HEX2, the temperature of the mixed air exiting HEX2 and directed to the furnace is determined. Utilising the heat transferred in HEX2, along with the known mass flow rate of the mixed air and its temperature at the inlet of HEX2, the temperature at the outlet of HEX2 can be calculated using the equation:

$$T^{out,\text{mix}}_{\text{a,HEX2}} = T^{in,\text{mix}}_{a,\text{HEX2}} + \frac{\dot{Q}_{\text{HEX2}}}{\dot{m}^{\text{mix}}_{\text{a}} \cdot c^{\text{mix}}_{p,\text{a}}}. \tag{4.26}$$

Finally, as described in the previous section, the linear regression analysis of analytical results was performed and utilised. This regression model takes into account key parameters, such as the mass of sludge and moisture, recirculation percentage, air flow rate, air temperature, and the amount of biogas. By inputting these functions into the regression model, I obtain an estimated temperature of the flue gas.

4.5 Results and discussion

4.5.1 Model validation

In the validation process, the simulated furnace temperature is meticulously compared with historical sensor data, specifically focusing on observations from the 1st of September 2021, as depicted in Fig. 4.3. The analysis is based on a 24-hour dataset and this duration is sufficient to capture the typical daily operational patterns of the wastewater treatment

plant. It includes daily fluctuations in inflow rate, temperature, and sludge characteristics. These short-term dynamics are critical for evaluating the immediate responsiveness and stability of the simulation model. Of course, access to longer-term data would enable a more comprehensive validation across varying operational scenarios, such as seasonal changes or maintenance cycles. Nonetheless, the 24-hour data serve as a reliable and representative baseline for initial validation, particularly when the chosen day reflects typical wastewater treatment plant operation. By running the simulation model under conditions mirroring those of the historical period, I sought to ensure its accuracy in replicating real-world dynamics.

The comparison revealed a reasonable alignment between the simulated and measured reactor temperatures, indicating that our simulation model captures the essential behavior of the system. This was supported by quantitative metrics such as Mean Squared Error (MSE), Mean Absolute Error (MAE), and the Coefficient of Determination (R-squared). With an MSE of 331.53, an MAE of 11.78, and an R-squared value of 0.71, the model was able to reasonably reproduce the observed trends and provided meaningful insights into the system's dynamics. While not fully capturing all variations, this level of correspondence suggests that the simulation offers a sufficiently reliable representation of the system for the purposes of analysis and understanding.

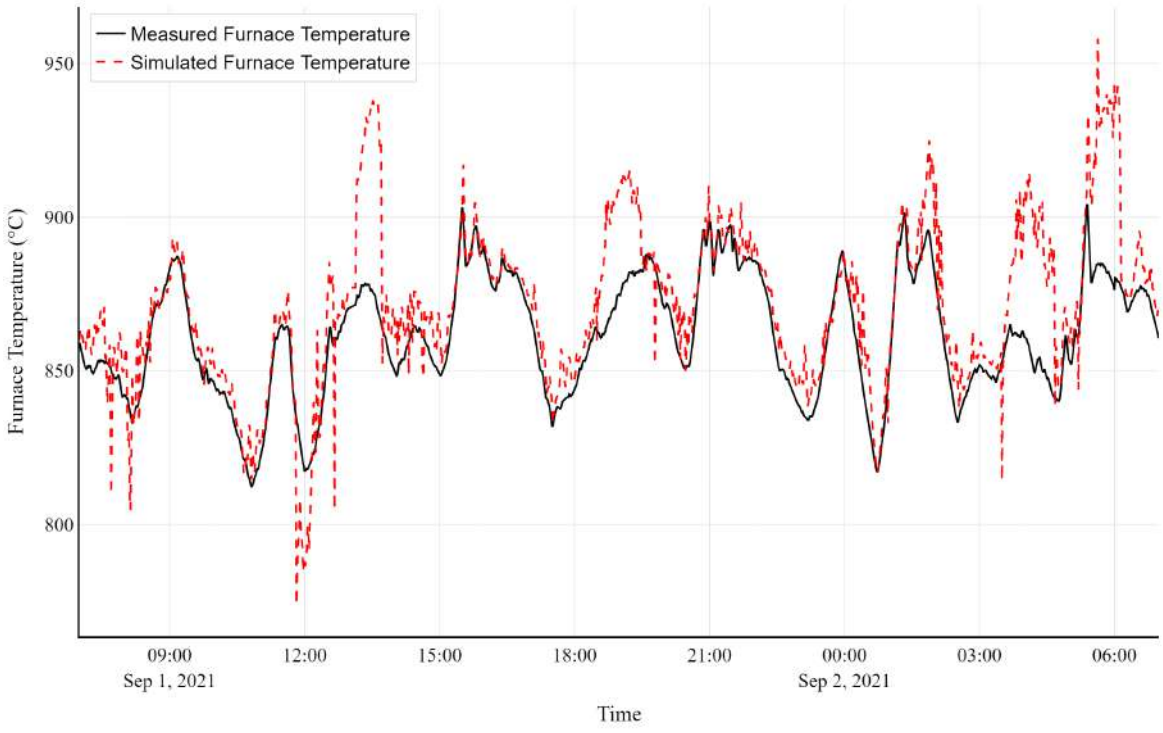

Figure 4.3: Comparison of measured and simulated furnace temperature.

4.5.2 Furnace output

Figures 4.4–4.6 show the relations between various parameters of the fluidised bed furnace. Furnace temperature in relation to excess air fuel ratio is shown in Fig. 4.4. Obviously, the decrease in the excess air ratio is inseparably connected with the temperature increase. The two plots, however, show a slight variation in temperature with the change in moisture content (Fig. 4.4a) and the recirculation rate (Fig. 4.4b) for a given excess air ratio. In the first case, representing the case of a recirculation rate at the level of 30%, the decrease in moisture content from 40 to 20% corresponds to a slight temperature increase (of about 30 degrees) for a high excess air ratio (of 2.2). With a decreasing excess air ratio, the decreasing moisture causes even more temperature growth. The influence of the recirculation rate is very similar. Recirculation decreasing from 40 to 20% results in a slight increase in temperature. This effect is more pronounced at lower excess air ratios.

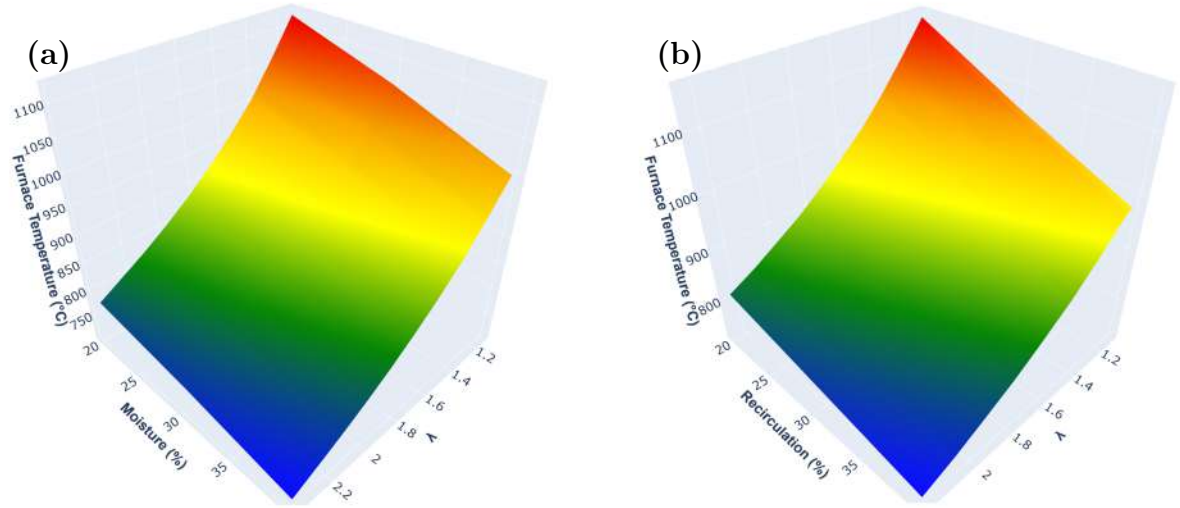

Figure 4.4: Furnace temperature under different conditions: (a) influence of moisture content and excess air ratio (recirculation rate 30%), (b) influence of recirculation rate and excess air ratio (moisture content 30%); Sludge flow 4 tons/hr.

Figure 4.5 shows the influence of recirculation rate and excess air ratio on CO_2 and O_2 concentration. As expected, CO_2 concentration (Fig. 4.5a) is increasing with the decrease in the excess air ratio. Simultaneously, O_2 concentration (Fig. 4.5b) is increasing with an increase in the excess air ratio. Recirculation seems to have a very small or no influence on both CO_2 and O_2 concentrations in the investigated range.

Finally, Fig. 4.6 displays the influence of moisture and excess air ratio on CO_2 and H_2O concentrations. It seems that moisture has either a very small or no influence on the CO_2

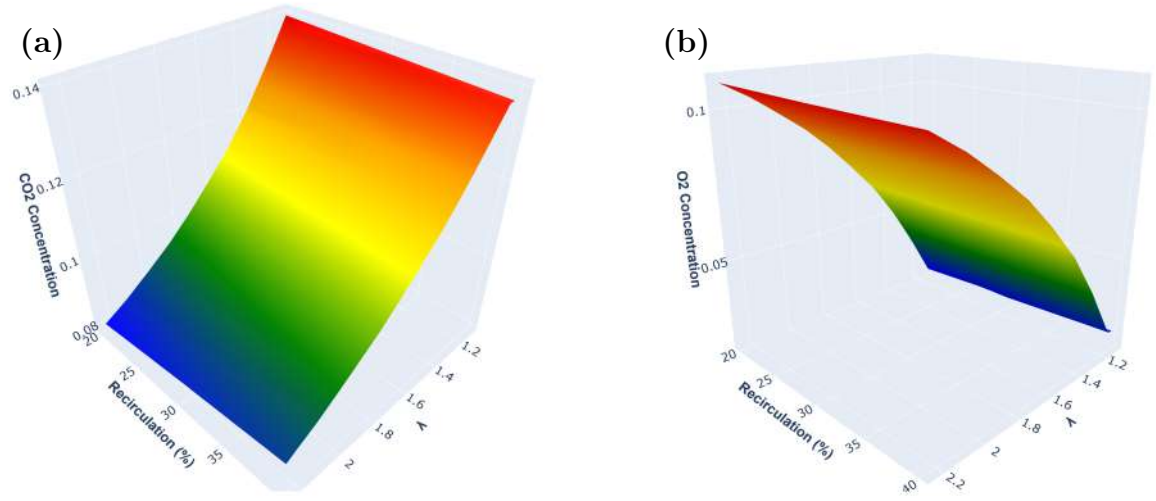

Figure 4.5: Influence of recirculation rate and excess air ratio on: (a) CO_2 concentration, (b) O_2 concentration; (Operating conditions: sludge flow 4 tons/hr, moisture content 30%).

concentration (Fig. 4.6a). However, when it comes to H_2O concentration (Fig. 4.6b), it obviously increases with an increase in the moisture content in the sludge.

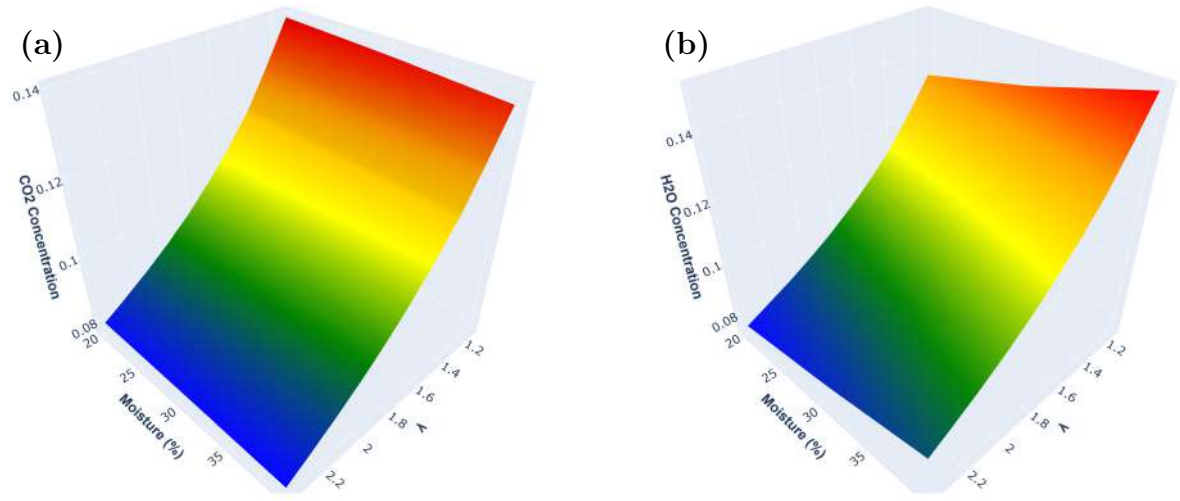

Figure 4.6: Influence of moisture content and excess air ratio on: (a) CO_2 concentration, (b) H_2O concentration; (Operating conditions: sludge flow 4 tons/hr, recirculation rate 30%).

4.6 Scenario simulation

The Pearson correlation analysis was conducted to investigate the relationships between various operational parameters, such as: sludge flow, recirculation rate, biogas flow, mixed air temperature, mixed air flow, moisture and furnace temperature. The correlation coefficients shown on the heatmap in Fig. 4.7 provide insight into the strength and direction of linear relationships between these parameters.

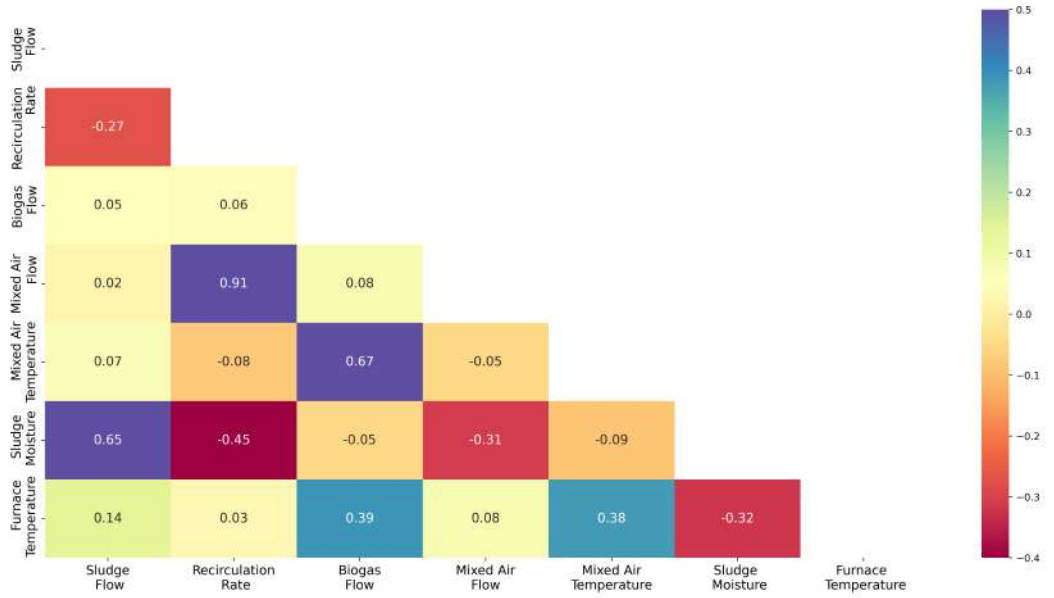

Figure 4.7: Pearson correlation.

Starting from the negative correlations, the value of the Pearson correlation coefficient for the recirculation rate and the moisture of the sludge ($r = -0.45$) indicated that an increase in the recirculation rate is justified for processing the sludge with a lower moisture content. This correlation is evident owing to the fact of achieving higher combustion temperatures for less-moisturized fuels. A negative correlation is also observed between sludge moisture and furnace temperature ($r = -0.32$) and mixed air flow ($r = -0.31$). These values, suggesting a weak, although not yet negligible relation, show that lower moisture levels in the sludge contribute to higher process temperatures, and thus are associated with an increased need for combustion air to provide the required temperature level. The positive correlation between recirculation rate and mixed air flow ($r = 0.91$) of very high value shows strong linear dependence between these two. This obviously indicates that an increase in recirculation rate, related to its adjustments aimed to maintain optimal conditions within the system, corresponds with an increase in mixed air flow. A strong positive correlation

is also shown between the biogas flow and mixed air temperature (r = 0.67), suggesting that higher biogas flow rates translate into the elevated temperatures of the mixed air, owing to heat released during biogas combustion and the corresponding flue gas temperature rise. Another strong positive correlation coefficient was obtained for sludge feeding rate and sludge moisture (r = 0.65), which clearly illustrates an increase of moisture in the system as the amount of sludge fed increases. Moreover, the moderate positive correlation between biogas flow and furnace temperature (r = 0.39) suggests that as the biogas flow increases, the furnace temperature also tends to increase. Similarly to the mixed air temperature, this relationship can be explained by the fact that higher biogas flow can enhance combustion efficiency, and in consequence raise the furnace temperature. This interrelation is also expressed through the positive moderate value of the correlation coefficient between furnace temperature and mixed air temperature (r = 0.38). Following this analysis, different scenarios in AnyLogic were considered based on the manipulation of the most influencing factors: biogas flow, sludge moisture, mixed air temperature and mixed air flow.

4.6.1 Multi-factor scenario analysis

In order to find the best solution for energy-saving in a wastewater treatment plant, the basic scenario and 5 other proposed scenarios were simulated and compared. Each scenario is characterised by different biogas flow rate, sludge moisture, mixed air temperature, and mixed air flow. These parameters were selected based on the Pearson correlation analysis described above. Based on the analysed options, the best proposed solution was selected.

The basic scenario is a simulation of the process under the same operation conditions, as for the recorded data, used for both input data and later the validation of the model. Further analysis includes 5 scenarios with parameters changed from the baseline (reference) scenario.

The other proposed scenarios focus on reducing the costs and efficiency of the wastewater treatment plant with the optimisation of the biogas amount used in order to enhance the decomposition processes in the fluidised bed furnace. Since the reduction of the biogas flow rate causes the temperature drop in the furnace, the aim here was to find an optimal solution, where the biogas consumption is lowered, but the temperature in the furnace is kept above 850°C, which is required for the correct and complete combustion, and satisfies the relevant regulations that involve the best available techniques (BAT) in the incineration of sewage sludge [190]. The daily fluctuations of biogas consumption in the real case scenario are presented in Fig. 4.8.

The change in the parameters for each proposed scenario is gathered in Table 4.1. The values are expressed in the percentage increase or decrease of the initial value of the parameter in the basic (reference) scenario, since the values varied in time in the 24-hour period. The simulated temperature changes during this time are presented in Figures 4.9 and 4.10. The red lines represent temperatures over 850°C, while the blue lines represent temperatures

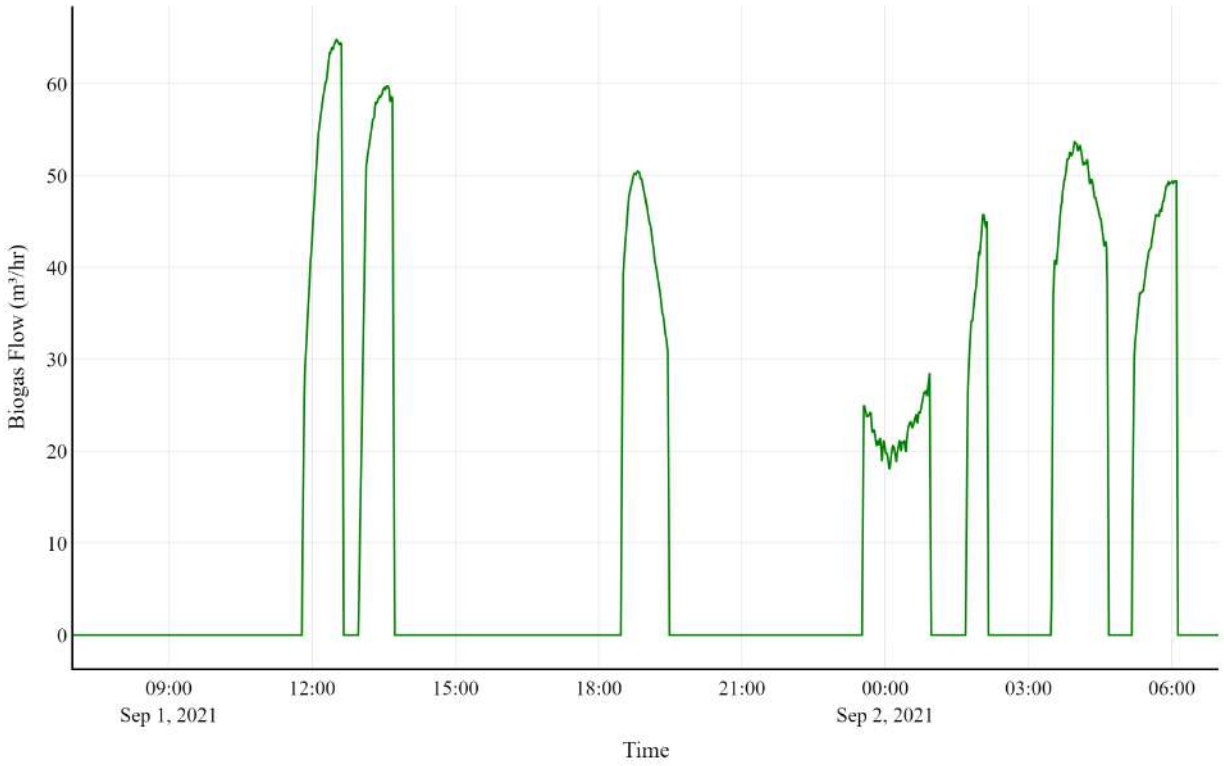

Figure 4.8: Daily fluctuations in biogas consumption (m^3/hr) fed into the furnace.

below this value. Green areas indicate time periods, where the biogas was injected into the furnace in order to keep the required temperature level. The time at which the biogas was injected is the same for the basic scenario and all of the other scenarios. The difference is the lower flow rate of the injected biogas, and therefore, lower total consumption.

Table 4.1: Scenario simulation plan (up and down arrows denote increase or decrease of the parameter).

Scheme	**Biogas flow**	**Sludge moisture**	**Mixed air temperature**	**Mixed air flow**
Scenario 1	30% ⇓	5% ⇑	20% ⇑	10% ⇑
Scenario 2	30% ⇓	30% ⇓	5% ⇓	10% ⇑
Scenario 3	40% ⇓	35% ⇓	10% ⇓	15% ⇑
Scenario 4	40% ⇓	40% ⇓	10% ⇓	20% ⇑
Scenario 5	45% ⇓	40% ⇓	20% ⇓	15% ⇑

The results across various scenarios show that in order to choose the best option, it is necessary to optimise between the unacceptable operation duration and total biogas consumption. The unacceptable operation duration is the total time (within simulated 24 h), in which the temperature in the furnace dropped below 850°C, which is the minimum com-

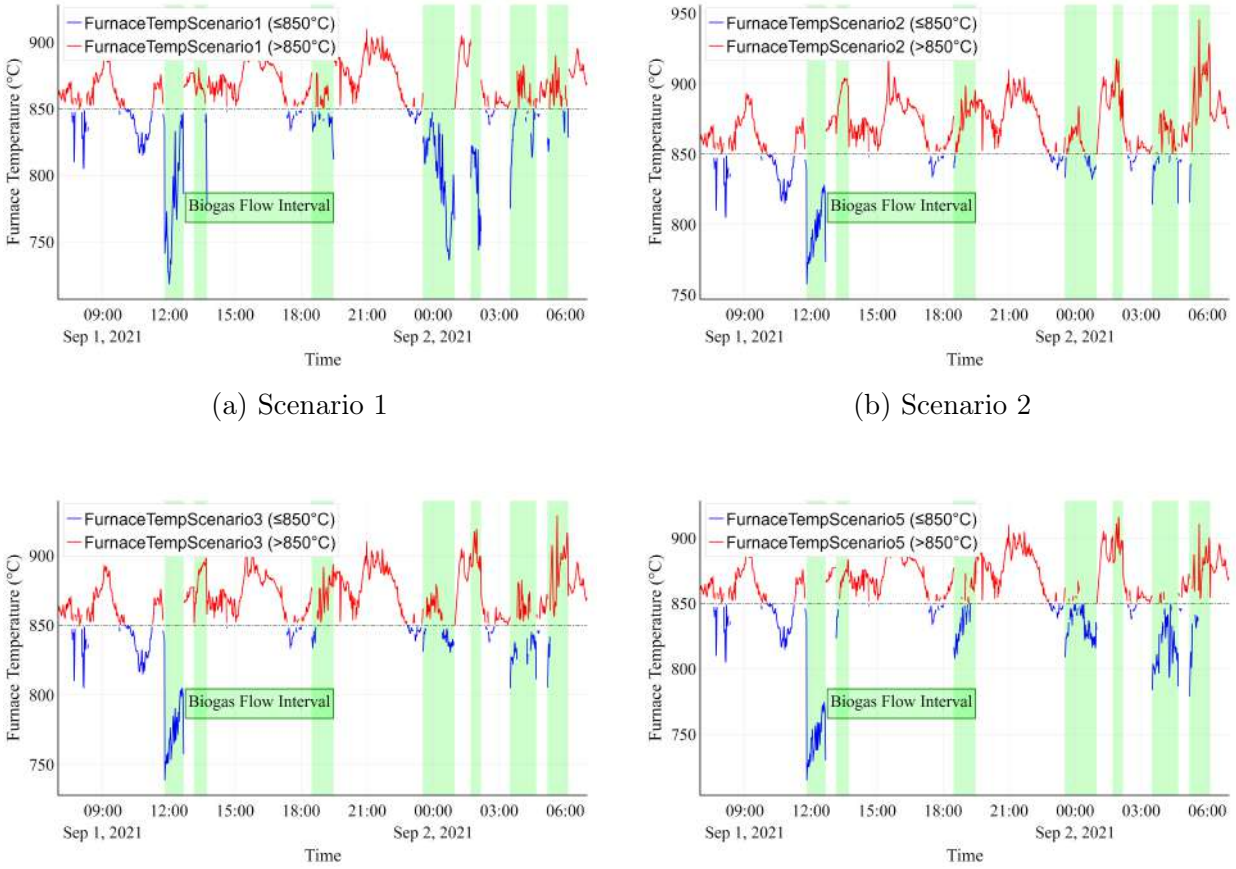

(a) Scenario 1

(b) Scenario 2

(c) Scenario 3

(d) Scenario 5

Figure 4.9: Furnace temperature variation for different scenarios.

bustion temperature demanded by European regulations. The basic scenario demonstrates 421 minutes of unacceptable operation duration and 273m^3 of biogas consumption.

Scenario 1 assumed a decrease of 30% of biogas flow, and an increase in sludge moisture (5%), mixed air temperature (20%), and mixed air flow (10%), see Table 4.1. These changes resulted in a slightly increased unacceptable operation duration of 448 minutes but with a significantly reduced biogas consumption of 191m^3 (Fig. 4.11). For Scenario 2 it was also proposed to decrease the biogas flow by 30%, while the sludge moisture decreased by 30%, the mixed air temperature decreased by 5%, and the mixed air flow increased by 10%. This solution shows an improvement with a decreased unacceptable operation duration of 317 minutes, maintaining the biogas consumption at 191m^3. Next, scenario 3, assumes a 40% decrease in biogas flow, a 35% decrease in sludge moisture, a 10% decrease in the mixed air temperature, and a 15% increase in mixed air flow. This continues the trend with further reduced unacceptable operation duration of 351 minutes, while biogas consumption lowered to 164m^3. Scenario 4, by further decreasing the sludge moisture and

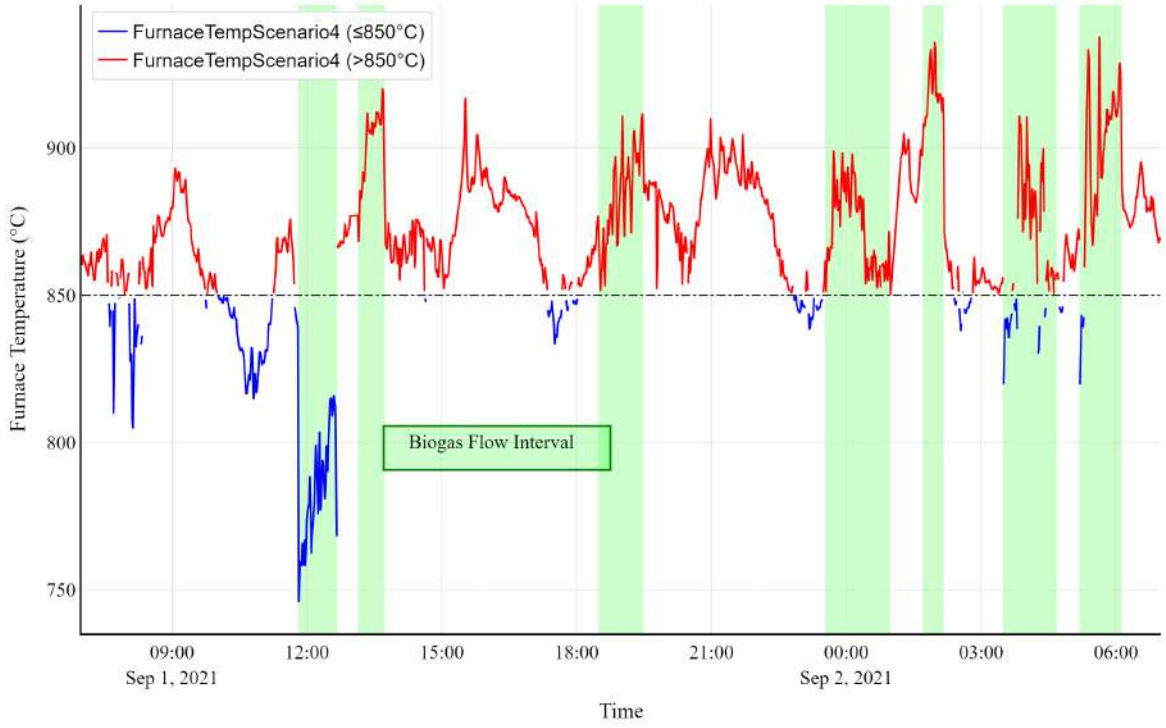

Figure 4.10: Furnace temperature variation for optimal scenario - scenario 4.

increasing the mixed air flow, presents an even more optimized performance, achieving 281 minutes of unacceptable operation duration and 164m^3 of biogas consumption. Finally, scenario 5 attempts to further reduce biogas consumption (45% decrease). While showing the highest unacceptable operation duration of 449 minutes, scenario 5 achieves the lowest biogas consumption at 123m^3. This showed that a further decrease in biogas flow causes the drop of the furnace temperature below the accepted level. Therefore, the best proposed scenario is scenario 4, which allows for both the reduction of the unacceptable operation duration and the biogas consumption. The biogas consumption was decreased by 40% when compared with the real-life case, and the unacceptable operation time decreased from 421 minutes to 281 minutes per day, which is 33% less. At the same time, the average fluidised bed temperature for scenario 4 is 867°C, while for the basic scenario, it is 5 degrees lower.

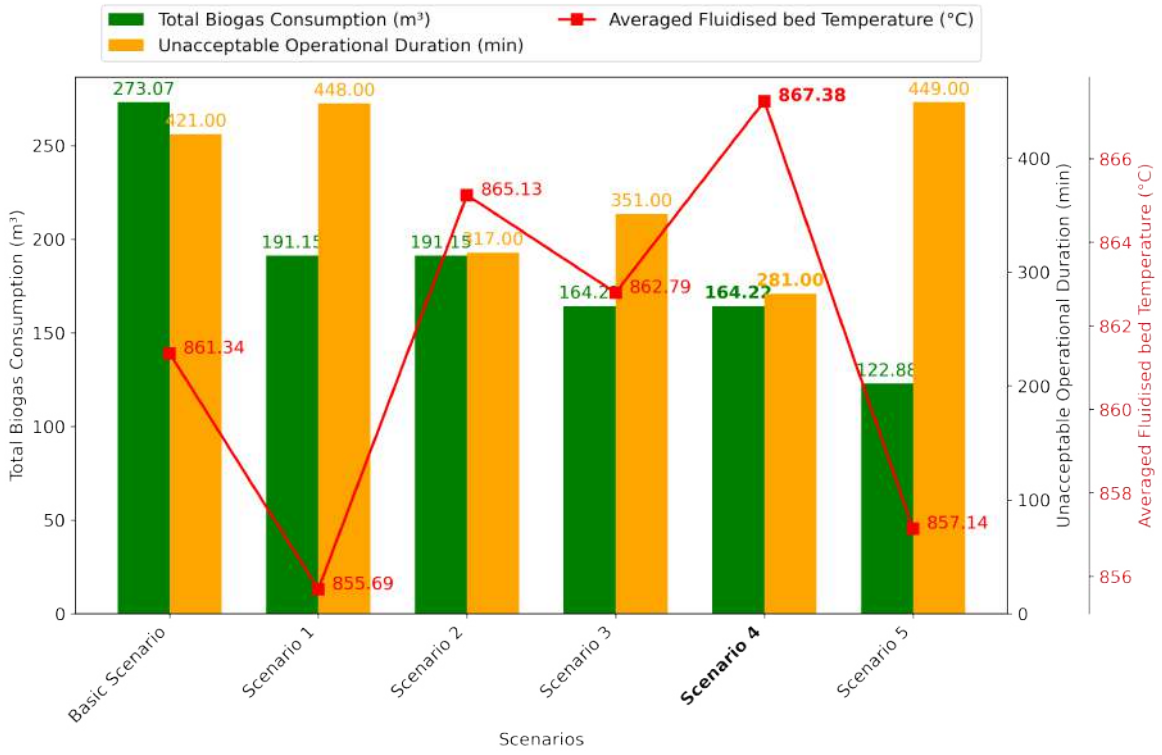

Figure 4.11: Comparison of operational metrics.

4.7 Conclusions and final remarks

The study covers the analysis of a sewage sludge incineration system of the wastewater treatment plant and searches for possibilities of reducing costs and finding energy savings solutions for the existing real-life system. It successfully demonstrated the development and implementation of a real-time Digital Twin for energy optimization in wastewater treatment, specifically targeting biogas consumption in the incineration process. By combining physical modeling, real-time data integration, and simulation in AnyLogic, I achieved a dynamic and accurate representation of the fluidised bed reactor and related components.

Five different scenarios with varying conditions were analysed using the developed model and the best solution predicted a 40% decrease in biogas consumption compared to real-life data (from 273 down to 164 m^3). Simultaneously, the duration of low-temperature combustion processes was reduced from 421 to 281 minutes per day. This solution represents significant resource savings, optimizing the overall efficiency of the WTTP's energy use. However, to achieve this, the sludge moisture needs to be decreased by 40%. Since drying is an energy-consuming process, this must be considered to ensure the net benefits align with the plant's energy optimization goals. However, these findings underscore the potential of

Digital Twin technology to significantly enhance energy efficiency, reduce operational costs, and contribute to more sustainable industrial processes.

The model presented in this work presents a useful optimisation method for similar systems. It can be used as a great tool for analysing many possible solutions and alignments of the interrelating conditions and parameters of the system, without the need for expensive or time-consuming testing methods. The model can be easily adjusted and continuously updated with real-time data, while maintaining its accuracy and relevance over time. This adaptability is a key feature of Digital Twin technology, by making the model a base component for developing a digital twin of the system that enables dynamic monitoring, predictive analysis, and helps in decision-making in a virtual environment mirroring real operations.

Chapter 5

Summary

5.1 General conclusions

This doctoral thesis has established and demonstrated a holistic, multi-scale framework for the analysis, monitoring, and optimization of complex thermochemical energy conversion systems. The research was driven by the critical need to bridge the gap between detailed component-level analysis and system-wide operational efficiency. This gap often limits the full potential of renewable energy technologies such as biomass gasification and waste incineration. Through the development of novel computational methods, the application of advanced data-driven techniques, and the pioneering implementation of a digital twin, this work provides a comprehensive roadmap for enhancing the performance and sustainability of complex energy systems.

The work started at the micro-scale with detailed modeling of a biomass conversion in a fixed-bed gasifier (Chapter 2). A major step was the development of the in-house two-dimensional Dynamic Coupled Eulerian-Lagrangian (DCEL) method, implemented to simulate the variability of bed movement down the reactor as the devolatilization progresses. The model was able to capture key processes that are often simplified in other studies. These included the release of volatiles and decomposition-related particle shrinkage, and coupled conduction-radiation heat transfer through the packed bed. By assuming the non-uniform porosity decreasing from the reactor wall to the core, the near-wall effect of enhanced heat transfer related to increased contribution of radiation in loosely packed zones was captured. The simulation results for the flow reactor case indicated the impact of process parameters, such as particle size and fuel feed rate, on the process dynamics. One of the main strengths of this model is its calculation efficiency. Relatively simple, it can deliver results much faster than more complex methods. A qualitative comparison of the proposed DCEL method predictions was then made with the advanced eXtended Discrete Element Method (XDEM) outcomes for the batch reactor case. XDEM provided a more complete 3D view of particle interactions and combustion chemistry. However, the study showed a

clear trade-off between accuracy and computational cost. This comparison gives engineers and researchers practical guidance. They can choose the model that best fits their goals, whether they need quick design tests or a deeper study of particle-scale physics.

Building on the earlier work, the thesis expanded to the system level using machine learning (ML) techniques (addressed in Chapter 3). A sewage sludge incineration plant was used as a case study. To support this, a detailed dataset was created with Aspen Plus simulations. This data was then used to train advanced ML models, including a new chained algorithm. The models showed high accuracy in predicting key performance indicators, i.e. temperature in the fluidized bed (TFB), steam heat transfer rate (SHTR), and dryer residence time (DRT). These parameters are essential for improving plant operations. The models also allowed parametric studies, which revealed complex relationships between inputs and outputs. These patterns are often difficult for plant operators to see. The optimization study then identified a set of operating parameters that could greatly improve energy efficiency. This brought the system closer to being energy self-sufficient.

Moving on to more advanced multi-method system modeling, the thesis focuses on the design and validation of a real-time digital twin for energy optimization (Chapter 4). Unlike static simulations, this digital twin combined chemical calculations, physical models of heat exchangers, and live plant data in a dynamic AnyLogic environment. It was not just a model but a working virtual replica. The twin could simulate the plant's behavior over 24 hours with high accuracy, as confirmed by historical sensor data. The real value came from scenario analysis. This led to a clear strategy: reduce biogas use by 40% and cut the time of non-compliant low-temperature operation by 33%. These improvements are more than just numbers. They translate to lowering operating costs, reducing dependence on fossil fuels, and supporting more sustainable and environmentally compliant operations.

In conclusion, this dissertation makes several key contributions to the fields of energy engineering and computational modeling:

1. A novel multi-scale modeling framework: It presents a proven pathway to integrate particle-scale, component-level, and system-wide analyses into one workflow. It also proves that looking at these parts separately is not enough to solve modern energy problems.

2. Advanced computational tools: The development of the DCEL method as an accessible tool for modeling reactive porous beds, promising in terms of computational efficiency and reliability. It has the potential to fill the gap between overly simplistic 1D models and computationally prohibitive high-fidelity CFD-DEM simulations. As such, and further developed to include other key physicochemical phenomena, it can serve as a tool for multivariate simulations, supporting in this way the in-depth process analysis, design and data-driven optimization.

3. A roadmap for ML-driven optimization: The successful application of a hybrid Aspen-ML methodology offers a robust template for optimizing other complex industrial processes where first-principles modeling is time-consuming or expensive, enabling rapid virtual experimentation and discovery of optimal set-points.

4. A practical Digital Twin implementation: The thesis moves beyond the theoretical concept of digital twins to deliver a fully realized, validated implementation for a wastewater treatment plant. It serves as a case study that showcases the tangible economic and environmental benefits of this Industry 4.0 technology, providing a replicable model for other industrial facilities.

The research outcomes together show that the future of energy system design and operation will depend on combining physics-based modeling, data-driven analysis, and digital twin technology. This combined approach is essential for reaching higher efficiency, stronger reliability, and better sustainability in the shift to a circular economy.

5.2 Future work

The findings of this thesis open up several promising avenues for future research, building directly upon the established foundation.

The most immediate and natural extension would be to model the complete gasification process beyond the pyrolysis zone. At this stage of development, the DCEL model provides a deep understanding of the devolatilization stage. Future work should integrate the drying, oxidation and reduction zones, incorporating homogeneous gas-phase reactions and heterogeneous surface reactions on the char. This would enable the prediction of final syngas composition and quality, which is the ultimate metric for gasifier performance.

A key next step is to connect the CFD model of the gasifier with the full system simulation of the energy plant. Right now, the system model uses simplified or input-based versions of the gasifier. In the future, an advanced model could be developed. In this setup, the detailed CFD model would run on a high-performance computing cluster and provide accurate boundary conditions and performance maps for a real-time system model. This would make it possible to optimize the system using detailed component behavior and support the design of fully integrated energy systems.

Furthermore, the digital twin implementation can be significantly enhanced. Future work could focus on building a real-time data pipeline. This pipeline would automatically feed live sensor data from the plant into the twin. With this setup, true online monitoring and predictive control would be possible. Applying Model Predictive Control (MPC) algorithms based on the digital twin could enable fully autonomous, closed-loop optimization of the incineration process. The system would then be able to adjust air flows, sludge feed, and biogas injection in real time, depending on fuel quality and plant demands.

Finally, the ML methodologies can be expanded. Applying deep learning architectures, such as Long Short-Term Memory (LSTM) networks, could improve the prediction of temporal dynamics and transient events within the plant. Additionally, exploring Reinforcement Learning (RL) could lead to the development of AI control agents that learn optimal operational strategies through interaction with the digital twin, further pushing the boundaries

of optimal plant operation.

In essence, this thesis lays the groundwork for a new generation of intelligent, integrated, and ultra-efficient energy conversion systems, and the proposed future work aims to bring this vision closer to reality.

Bibliography

[1] I. Janajreh, I. Adeyemi, S.S. Raza, and C. Ghenai. A review of recent developments and future prospects in gasification systems and their modeling. *Renewable and Sustainable Energy Reviews*, 138:110505, 2021.

[2] D. Kardaś, S. Polesek-Karczewska, T. Turzyński, I. Wardach-Święcicka, Ł. Heda, J. Szymborski, and P. Hercel. The red-hot air furnace for an externally fired gas turbine power unit designing aspects and performance testing. *Appl. Therm. Eng.*, 236, Part B:121552, 2024.

[3] Y.A. Situmorang, Z. Zhao, A.Yoshida, A. Abudula, and G. Guan. Small-scale biomass gasification systems for power generation (<200 kW class): A review. *Renewable and Sustainable Energy Reviews*, 117:109486, 2020.

[4] A.Z. Yahaya, M.R. Somalu, A. Muchtar, S.A. Sulaiman, and W.R.W. Daud. Effect of particle size and temperature on gasification performance of coconut and palm kernel shells in downdraft fixed-bed reactor. *Energy*, 175:931–940, 2019.

[5] J. Cespiva, L. Niedzwiecki, J.Vereš, J.Skřínský, M.Wnukowski, K.Borovec, and T. Ochodek. Evaluation of the performance of the cross/updraft type gasification technology with the sliding bed over a circular grate. *Biomass and Bioenergy*, 167: 106639, 2022.

[6] S. Valizadeh, H. Hakimian, A. Farooq, B.-H. Jeon, W.-H. Chen, S.H. Lee, S.-C. Jung, M.W. Seo, and Y.-K. Park. Valorization of biomass through gasification for green hydrogen generation: A comprehensive review. *Bioresource Technology*, 365:128143, 2022.

[7] H. Song, G. Yang, P. Xue, Y. Li, J. Zou, S. Wang, H. Yang, and H. Chen. Recent development of biomass gasification for H2 rich gas production. *Applications in Energy and Combustion Science*, 10:100059, 2022.

[8] J. Zhang, J. Zhong, L. Yang, Z. Wang, D. Chen, and Q. Wang. Enhancement effect of semicoke waste heat on energy conservation and hydrogen production from biomass gasification. *Renewable Energy*, 236:121340, 2024.

[9] M. A. Masmoudi, M. Sahraoui, N. Grioui, and K. Halouani. 2-D modeling of thermo-kinetics coupled with heat and mass transfer in the reduction zone of a fixed bed downdraft biomass gasifier. *Renewable Energy*, 66:288–298, 2014.

[10] P. Basu. *Biomass Gasification, Pyrolysis and Torrefaction: Practical Design and Theory*. Academic Press, 2013.

[11] A.A.P. Susastriawan, H. Saptoadi, and Purnomo. Small-scale downdraft gasifiers for biomass gasification: A review. *Renewable and Sustainable Energy Reviews*, 76: 989–1003, 2017.

[12] M. Ajorloo, M. Ghodrat, J. Scott, and V. Strezov. Recent advances in thermodynamic analysis of biomass gasification: A review on numerical modelling and simulation. *Journal of the Energy Institute*, 102:395–419, 2022.

[13] S. Polesek-Karczewska, P. Hercel, B. Adibimanesh, and I. Wardach-Święcicka. Towards sustainable biomass conversion technologies: a review of mathematical modeling approaches. *Sustainability*, 16:8719, 2024.

[14] S. Safarian, R. Unnþórsson, and C. Richter. A review of biomass gasification modelling. *Renewable and Sustainable Energy Reviews*, 110:378–391, 2019.

[15] A. Ramos, E. Monteiro, and A. Rouboa. Numerical approaches and comprehensive models for gasification process: A review. *Renewable and Sustainable Energy Reviews*, 110:188–206, 2019.

[16] S. Ghorbani, K. Atashkari, and M. Borji. Three-stage model-based evaluation of a downdraft biomass gasifier. *Renewable Energy*, 194:734–744, 2022.

[17] M. Oevermann, S. Gerber, and F. Behrendt. Euler–Lagrange/DEM simulation of wood gasification in a bubbling fluidized bed reactor. *Particuology*, 7:307–316, 2009.

[18] M.J. Andrews and P.J. O'Rourke. The multiphase particle-in-cell (MP-PIC) method for dense particulate flows. *International Journal of Multiphase Flow*, 22(2):379–402, 1996.

[19] D.M. Snider, P.J. O'Rourke, and M.J. Andrews. An incompressible two-dimensional multiphase particle-in-cell model for dense particle flows. Technical report, Los Alamos National Laboratories, Los Alamos, LA-13280-MS, 1997.

[20] D.M. Snider. An incompressible three-dimensional multiphase particle-in-cell model for dense particle flows. *Journal of Computational Physics*, 170(2):523–549, 2001.

[21] D.M. Snider, S.M. Clark, and P.J. O'Rourke. Eulerian–lagrangian method for three-dimensional thermal reacting flow with application to coal gasifiers. *Chemical Engineering Science*, 66:1285–1295, 2011.

[22] J. Xie, W. Zhong, B. Jin, Y. Shao, and H. Liu. Simulation on gasification of forestry residues in fluidized beds by eulerian–lagrangian approach. *Bioresource Technology*, 121:36–46, 2012.

[23] M. Aziz, D. Budianto, and T. Oda. Computational fluid dynamic analysis of co-firing of palm kernel shell and coal. *Energies*, 9(3):137, 2016.

[24] H. Sun, G. Bao, H. Liu, J. Hu, and H. Wang. Particle-scale simulation of air-blown gasification of biomass materials in bubbling fluidized bed reactor. *Renewable Energy*, 220:119682, 2024.

[25] W. P. Adamczyk, K. Myohanen, E.-U. Hartge, J. Ritvanen, A. Klimanek, T. Hyppanen, and R.A. Białecki. Generation of data sets for semi-empirical models of circulated fluidized bed boilers using hybrid euler-lagrange technique. *Energy*, 143:219–240, 2018.

[26] G. Hu and G. Li and Y. Zheng and Z. Zhang and Y. Xu. Euler-Lagrange modeling of wood chip gasification in a small-scale gasifier. *Journal of the Energy Institute*, 88: 314–322, 2015.

[27] I. Janajreh and M. Al Shrah. Numerical and experimental investigation of downdraft gasification of wood chips. *Energy Conversion and Management*, 65:783–792, 2013.

[28] U. Kumar and M.C. Paul. Cfd modelling of biomass gasification with a volatile break-up approach. *Journal of Chemical Engineering", volume=195, pages=413–422, year=2019,.*

[29] D.A. Rodriguez-Alejandro, A. Zaleta-Aguilar, V.H. Rangel-Hernández, and A. Olivares-Arriaga. Numerical simulation of a pilot-scale reactor under different operating modes: Combustion, gasification and pyrolysis. *Biomass and Bioenergy*, 116:80–88, 2018.

[30] H. Li, T. Qi, and Y. Zhang. Effect of furnace structure on burden distribution and gas flow in sinter vertical cooling furnace. *Applied Sciences*, 13:11268, 2023.

[31] Y. Gao and C. K. Chan. CFD-DEM simulation of raceway size and mechanical characteristics of industrial scale blast furnace. *Polish Journal of Chemical Technology*, 25(3):71–78, 2023.

[32] M. Wang, T. Jia, X. Song, L. Yin, D. Chen, and K. Qian. CFD–DEM simulation of heat transfer and reaction characteristics of pyrolysis process of MSW heated by high-temperature flue gas. *Processes*, 12(390), 2024.

[33] MFiX. *Open Source Multiphase Flow Modeling for Real-world Applications*. Available: https://mfix.netl.doe.gov/products/mfix/, March 2024.

[34] J. G. Rosser, T. Okosun, O. J. Ugarte, and C. Q. Zhou. Investigation of jamming phenomenon in a direct reduction furnace pellet feed system using the discrete element method. *Dynamics*, 3:711–736, 2023.

[35] B. Peters, X. Besseron, A. Estupinan, F. Hoffmann, M. Michael, and A. Mahmoudi. Enhanced thermal process engineering by the Extended Discrete Element Method (XDEM). *Universal Journal of Engineering Science*, 1(4):139–145, 2013.

[36] OpenFOAM. *OpenFOAM documentation*. Available: http://www.openfoam.com. [Accessed, December 2013. URL `http://www.openfoam.com`.

[37] A. A. Estupinan Donoso and B. Peters. *XDEM used for predicting tungsten-oxide reduction*. CAPE Forum 2015, Computer Aided Process Engineering, University of Paderborn, Germany 2015, April 27-29, 2015.

[38] A. H. Mahmoudi, F. Hoffmann, and B. Peters. Semi-resolved modeling of heat-up, drying and pyrolysis of biomass solid particles as a new feature in XDEM. *Applied Thermal Engineering*, 93:1091–1104, 2016.

[39] A. Anca-Couce, N. Zobel, and H.A. Jakobsen. Multi-scale modeling of fixed-bed thermo-chemical processes of biomass with the representative particle model: Application to pyrolysis. *Fuel*, 103:773–782, 2013.

[40] J.F. Perez, A. Melgar, and F.V. Tinaut. Modeling of fixed bed downdraft biomass gasification: Application on lab-scale and industrial reactors. *International Journal of Energy Research*, 38:319–338, 2014.

[41] A.K. Sharma. Modeling fluid and heat transport in the reactive, porous bed of downdraft (biomass) gasifier. *International Journal of Heat and Fluid Flow*, 28:1518–1530, 2007.

[42] W. Yang, A. Ponzio, C. Lucas, and W. Blasiak. Performance analysis of a fixed-bed biomass gasifier using high-temperature air. *Fuel*, 87:235–245, 2006.

[43] C. Mandl, I. Obernberger, and F. Biedermann. Modelling of an updraft fixed-bed gasifier operated with softwood pellets. *Fuel*, 89:3795–3806, 2010.

[44] T.K. Patra, K.R. Nimisha, and P.N. Sheth. A comprehensive dynamic model for downdraft gasifier using heat and mass transport coupled with reaction kinetics. *Energy*, 116:1230–42, 2016.

[45] S. Sharma S. and P.N. Sheth. Air-steam biomass gasification: Experiments, modeling and simulation. *Energy Convers. Manage.*, 110:307–18, 2016.

[46] J.F. Perez, P.N. Benjumea, and A. Melgar. Sensitivity analysis of a biomass gasification model in fixed bed downdraft reactors: Effect of model and process parameters on reaction front. *Biomass Bioenergy*, 83:403–21, 2015.

[47] Y. Hou, B. Yang, S. Zhang, Y. Qi, and X. Yu. 4E analysis of an integrated solar-biomass heating system: A case study in rural housing of northern China. *Sustainable Energy Technologies and Assessments*, 53:102794, 2022.

[48] Z. Shareefdeen and A.A. Mishu. Air emissions in waste to energy (W2E) plants. *Clean Technologies and Environmental Policy*, pages 1–10, 2021.

[49] D. Panepinto, F. Viggiano, and G. Genon. Analysis of the environmental impact of a biomass plant for the production of bioenergy. *Renewable and Sustainable Energy Reviews*, 51:634–647, 2015.

[50] The European Green Deal. Communication from the Commission to the European Parliament, the European Council, the European Economic and Social Committee of the Regions. COM(2019) 640 final, Brussels, 11.12.2019.

[51] P. Ziółkowski, J. Badur, H. Pawlak-Kruczek, K. Stasiak, M. Amiri, L. Niedzwiecki, K. Krochmalny, J. Mularski, P. Madejski, and D. Mikielewicz. Mathematical modelling of gasification process of sewage sludge in reactor of negative CO2 emission power plant. *Energy*, 244:122601, 2022.

[52] S. Polesek-Karczewska, T. Turzyński, D. Kardaś, and Ł. Heda. Front velocity in the combustion of blends of poultry litter with straw. *Fuel Processing Technology*, 176: 307–315, 2018.

[53] M. Kantorek, K. Jesionek, S. Polesek-Karczewska, P. Ziółkowski, M. Stajnke, and J. Badur. Thermal utilization of meat-and-bone meal using the rotary kiln pyrolyzer and the fluidized bed boiler–the performance of pilot-scale installation. *Renewable Energy*, 164:1447–1456, 2021.

[54] G. Lazaroiu and L. Mihaescu. *Innovative Renewable Waste Conversion Technologies*. Springer, 2021.

[55] M. Haghighat, N. Majidian, A. Hallajisani, and M. Samipourgiri. Production of bio-oil from sewage sludge: A review on the thermal and catalytic conversion by pyrolysis. *Sustainable Energy Technologies and Assessments*, 42:100870, 2020.

[56] C.P. Gerba and J.E. Smith. Sources of pathogenic microorganisms and their fate during land application of wastes. *Journal of Environmental Quality*, 34:42–48, 2005.

[57] J. Zhang, J. Jin, M. Wang, R. Naidu, Y. Liu, Y.B. Man, X. Liang, M.H. Wong, P. Christie, Y. Zhang, C. Song, and S. Shan. Co-pyrolysis of sewage sludge and rice husk/ bamboo sawdust for biochar with high aromaticity and low metal mobility. *Environmental Research*, 191:110034, 2020.

[58] A. M. Zaharioiu, F. Bucura, R.E. Ionete, F. Marin, M. Constantinescu, and S. Oancea. Opportunities regarding the use of technologies of energy recovery from sewage sludge. *SN Applied Sciences*, 3:775, 2021.

[59] M. Kacprzak, E. Neczaj, K. Fijałkowski, A. Grobelak, A. Grosser, M. Worwag, A. Rorat, H. Brattebo, A. Almås, and B.R. Singh. Sewage sludge disposal strategies for sustainable development. *Environmental research*, 156:39–46, 2017.

[60] Eurostat(2018). Total sewage sludge production from urban wastewater. `https://ec.europa.eu/eurostat/databrowser/view/ten00030/default/table?lang=en`.

[61] S. Alamu, O. Samuel, A. Wemida, T. Tsegaye, and G. Oguntimein. Sustainability assessment of municipal solid waste in Baltimore USA. *Sustainability*, 13(4):1915, 2021.

[62] T. Sato, M. Qadir, S. Yamamoto, T. Endo, and A. Zahoor. Global, regional, and country level need for data on wastewater generation, treatment, and use. *Agricultural Water Management*, 130:1–13, 2013.

[63] J. Mateo-Sagasta, L. Raschid-Sally, and A. Thebo. Global wastewater and sludge production, treatment and use. In *Wastewater*, pages 15–38. Springer, 2015.

[64] S. Werle and R.K. Wilk. A review of methods for the thermal utilization of sewage sludge: The Polish perspective. *Renewable Energy*, 35(9):1914–1919, 2010.

[65] G. Przydatek and A.K. Wota. Analysis of the comprehensive management of sewage sludge. *Journal of Material Cycles and Waste Management*, 22:80–88, 2020.

[66] K. Śpiewak. Gasification of Sewage Sludge — A Review. *Energies*, 17(17):4476, 2024.

[67] N. Gao, K. Kamran, C. Quan, and P.T. Williams. Thermochemical conversion of sewage sludge: A critical review. *Progress in Energy and Combustion Science*, 79: 100843, 2020.

[68] M. Hu, Z. Ye, H. Zhang, B. Chen, Z. Pan, and J. Wang. Thermochemical conversion of sewage sludge for energy and resource recovery: technical challenges and prospects. *Environmental Pollutants and Bioavailability*, 33:145–163, 2021.

[69] D. Panepinto, S. Fiore, G. Genon, and M. Acri. Thermal valorization of sewer sludge: perspectives for large wastewater treatment plants. *Journal of Cleaner Production*, 137:1323–1329, 2016.

[70] A. Kijo-Kleczkowska, K. Środa, and H. Otwinowski. Study into combustion of sewage sludge as energetic fuel. *Archives of Mining Science*, 58(4):1085–1100, 2013.

[71] J. Oladejo, K. Shi, X. Luo, G. Yang, and W. Tao. A review of sludge-to-energy recovery methods. *Energies*, 12:60, 2019.

[72] M. Chen, J. Yang, L. Hu, M.S. Hossain, and G. Muhammad. Urban healthcare big data system based on crowdsourced and cloud-based air quality indicators. *IEEE Communications Magazine*, 56(11):14–20, 2018.

[73] O.S. Djandja, A.A. Salami, Z.-C. Wang, J. Duo, L.-X. Yin, and P.-G. Duan. Random forest-based modeling for insights on phosphorus content in hydrochar produced from hydrothermal carbonization of sewage sludge. *Energy*, page 123295, 2022.

[74] M. Bertolini, D. Mezzogori, M. Neroni, and F. Zammori. Machine Learning for industrial applications: A comprehensive literature review. *Expert Systems with Applications*, 175:114820, 2021.

[75] F. Bagherzadeh and T. Shafighfard. Ensemble Machine Learning approach for evaluating the material characterization of carbon nanotube-reinforced cementitious composites. *Case Studies in Construction Materials*, 17:e01537, 2022.

[76] F. Bagherzadeh, A.S. Nouri, M.-J. Mehrani, and S. Thennadil. Prediction of energy consumption and evaluation of affecting factors in a full-scale wwtp using a machine learning approach. *Process Safety and Environmental Protection*, 154:458–466, 2021.

[77] T. Shafighfard, F. Bagherzadeh, R.A. Rizi, and D.-Y. Yoo. Data-driven compressive strength prediction of steel fiber reinforced concrete (sfrc) subjected to elevated temperatures using stacked machine learning algorithms. *Journal of Materials Research and Technology*, 21:3777–3794, 2022.

[78] S.R.Naqvi, Z. Hameed, R. Tariq, S.A. Taqvi, Imtiaz I. Ali, M.B.K. Niazi, T. Noor, A. Hussain, N. Iqbal, and M. Shahbaz. Synergistic effect on co-pyrolysis of rice husk and sewage sludge by thermal behavior, kinetics, thermodynamic parameters and artificial neural network. *Waste Management*, 85:131–140, 2019.

[79] Y.W. Huang and MQ M.Q. Chen. Artificial neural network modeling of thin layer drying behavior of municipal sewage sludge. *Measurement*, 73:640–648, 2015.

[80] M. El-Rawy, M.K. Abd-Ellah, H. Fathi, and A.K.A Ahmed. Forecasting effluent and performance of wastewater treatment plant using different machine learning techniques. *Journal of Water Process Engineering*, 44:102380, 2021.

[81] R. Oulebsir, A. Lefkir, A. Safri, and A. Bermad. Optimization of the energy consumption in activated sludge process using deep learning selective modeling. *Biomass and Bioenergy*, 132:105420, 2020.

[82] B. Adibimanesh, S. Polesek-Karczewska, F. Bagherzadeh, P. Szczuko, and T. Shafighfard. Energy consumption optimization in wastewater treatment plants: machine learning for monitoring incineration of sewage sludge. *Sustainable Energy Technologies and Assessments*, 56:103040, 2023.

[83] M. Bagheri, R. Esfilar, M.S. Golchi, and C.A. Kennedy. A comparative data mining approach for the prediction of energy recovery potential from various municipal solid waste. *Renewable and Sustainable Energy Reviews*, 116:109423, 2019.

[84] A. Sharafati, S.B.H.S. Asadollah, and M. Hosseinzadeh. The potential of new ensemble machine learning models for effluent quality parameters prediction and related uncertainty. *Process Safety and Environmental Protection*, 140:68–78, 2020.

[85] M. Yaqub, H. Asif, S. Kim, and W. Lee. Modeling of a full-scale sewage treatment plant to predict the nutrient removal efficiency using a long short-term memory (LSTM) neural network. *Journal of Water Process Engineering*, 37:101388, 2020.

[86] H. Bi, C. Wang, X. Jiang, C. Jiang, L. Bao, and Q. Lin. Thermodynamics, kinetics, gas emissions and artificial neural network modeling of co-pyrolysis of sewage sludge and peanut shell. *Fuel*, 284:118988, 2021.

[87] W. Zhang, X. Cheng, Y. Hu, and Y. Yan. Online prediction of biomass moisture content in a fluidized bed dryer using electrostatic sensor arrays and the random forest method. *Fuel*, 239:437–445, 2019.

[88] O.S. Djandja, P.-G. Duan, L.-X. Yin, Z.-C. Wang, and J. Duo. A novel machine learning-based approach for prediction of nitrogen content in hydrochar from hydrothermal carbonization of sewage sludge. *Energy*, 232:121010, 2021.

[89] Annual Energy Outlook. With Projections to 2050. *US Energy Information Administration*, 2007.

[90] K. Holmberg, R. Siilasto, T. Laitinen, P. Andersson, and A. Jäsberg. Global energy consumption due to friction in paper machines. *Tribology International*, 62:58–77, 2013.

[91] F.S.T. da Silva, C.A. da Costa, C.D.P. Crovato, and R. da Rosa Righi. Looking at energy through the lens of Industry 4.0: A systematic literature review of concerns and challenges. *Computers & Industrial Engineering*, 143:106426, 2020.

[92] T. Stock, M. Obenaus, S. Kunz, and H. Kohl. Industry 4.0 as enabler for a sustainable development: A qualitative assessment of its ecological and social potential. *Process Safety and Environmental Protection*, 118:254–267, 2018.

[93] K. Bunse, M. Vodicka, P. Schönsleben, M. Brülhart, and F.O. Ernst. Integrating energy efficiency performance in production management–gap analysis between industrial needs and scientific literature. *Journal of Cleaner Production*, 19(6-7):667–679, 2011.

[94] J.R. Duflou, J.W. Sutherland, D. Dornfeld, C. Herrmann, J. Jeswiet, S. Kara, M. Hauschild, and K. Kellens. Towards energy and resource efficient manufacturing: A processes and systems approach. *CIRP annals*, 61(2):587–609, 2012.

[95] N. Martin, E. Worrell, M. Ruth, L. Price, R.N. Elliott, A.M. Shipley, and J. Thorne. Emerging energy-efficient industrial technologies. Technical report, American Council for an Energy-Efficient Economy (ACEEE), 2000.

[96] A. Sa, P. Thollander, and M. Rafiee. Industrial energy management systems and energy-related decision-making. *Energies*, 11(10):2784, 2018.

[97] J. Friederich, D.P. Francis, S. Lazarova-Molnar, and N. Mohamed. A framework for data-driven digital twins of smart manufacturing systems. *Computers in Industry*, 136:103586, 2022. ISBN: 0166-3615 Publisher: Elsevier.

[98] Y. Sun, M. Lu, Y. Sun, Z. Chen, H. Duan, and D. Liu. Application and evaluation of energy conservation technologies in wastewater treatment plants. *Applied Sciences*, 9 (21), 2019. ISSN 2076-3417.

[99] S. Di Fraia, N. Massarotti, and L. Vanoli. A novel energy assessment of urban wastewater treatment plants. *Energy Conversion and Management*, 163:304–313, 2018. ISSN 0196-8904.

[100] Sameer Al-Dahidi, Mohammad Alrbai, Loiy Al-Ghussain, and Ali Alahmer. Maximizing energy efficiency in wastewater treatment plants: A data-driven approach for waste heat recovery and an economic analysis using organic rankine cycle and thermal energy storage. *Applied Energy*, 362:123008, 2024.

[101] Y. Yu, Z. Zou, and S. Wang. Statistical regression modeling for energy consumption in wastewater treatment. *Journal of Environmental Sciences*, 75:201–208, January 2019. ISSN 1001-0742. URL `http://dx.doi.org/10.1016/j.jes.2018.03.023`.

[102] Haixu Ding, Jian Tang, and Junfei Qiao. Dynamic modeling of multi-input and multi-output controlled object for municipal solid waste incineration process. *Applied Energy*, 339:120982, 2023.

[103] M. Grieves. Digital twin: manufacturing excellence through virtual factory replication. *White paper*, 1(2014):1–7, 2014.

[104] A. Khodadadi and S. Lazarova-Molnar. Essential Data Requirements for Industrial Energy Efficiency with Digital Twins: A Case Study Analysis. *Procedia Computer Science*, 238:631–638, 2024.

[105] F.E. Cellier and J. Greifeneder. *Continuous system modeling*. Springer Science & Business Media, 2013.

[106] A.-J. Wang, H. Li, Z. He, Y. Tao, H. Wang, M. Yang, D. Savic, G.T. Daigger, and N. Ren. Digital Twins for Wastewater Treatment: A Technical Review. *Engineering*, 36:21–35, 2024. ISSN 2095-8099.

[107] W.-Y. Sean, Y.-Y. Chu, L.L. Mallu, J.-G. Chen, and H.-Y. Liu. Energy consumption analysis in wastewater treatment plants using simulation and SCADA system: Case study in northern Taiwan. *Journal of Cleaner Production*, 276:124248, 2020.

[108] F. Harrou, T. Cheng, Y. Sun, T. Leiknes, and N. Ghaffour. A data-driven soft sensor to forecast energy consumption in wastewater treatment plants: A case study. *IEEE Sensors Journal*, 21(4):4908–4917, 2020.

[109] J.F. de Canete, P. del Saz-Orozco, J. Gómez de Gabriel, R. Baratti, A. Ruano, and I. Rivas-Blanco. Control and soft sensing strategies for a wastewater treatment plant using a neuro-genetic approach. *Computers & Chemical Engineering*, 144:107146, 2021.

[110] R. Hosseinalizadeh, H. Shakouri, and H. Izadbakhsh. Planning for energy production from municipal solid waste: An optimal technology mix via a hybrid closed-loop system dynamics-optimization approach. *Expert Systems with Applications*, 199:116929, 2022.

[111] R. Zhao, B. Xi, Y. Liu, J. Su, and S. Liu. Economic potential of leachate evaporation by using landfill gas: A system dynamics approach. *Resources, Conservation and Recycling*, 124:74–84, 2017.

[112] A.C.H. Pinha and J.K. Sagawa. A system dynamics modelling approach for municipal solid waste management and financial analysis. *Journal of Cleaner Production*, 269: 122350, 2020.

[113] R.R. Bora, R.E. Richardson, and F. You. Resource recovery and waste-to-energy from wastewater sludge via thermochemical conversion technologies in support of circular economy: a comprehensive review. *BMC Chemical Engineering*, 2:8, 2020.

[114] M. Praspaliauskas and N. N. Pedišius. A review of sludge characteristics in lithuania's wastewater treatment plants and perspectives of its usage in thermal processes. *Renewable and Sustainable Energy Reviews*, 67:899–907, 2017.

[115] A. Kijo-Kleczkowska, K. Środa, M. Kosowska-Golachowska, T. Musiał, and K. Wolski. Combustion of pelleted sewage sludge with reference to coal and biomass. *Fuel*, 170: 141–160, 2016.

[116] W. Rulkens. Sewage sludge as a biomass resource for the production of energy: Overview and assessment of the various options. *Energy and Fuels*, 22:9–15, 2008.

[117] E. Guibelin. Sludge thermal oxidation processes: Mineral recycling, energy impact, and greenhouse effect gases release. *Water Science and Technology*, 49(10):209–216, 2004.

[118] A. Abusoglu, A. Tozlu, and A. Anvari-Moghaddam. A two-stage orc integration to an existing fluidized bed sewage sludge incineration plant for power production in the scope of waste-to-energy. *International Journal of Thermodynamics*, 25(1):109–121, 2022.

[119] H. Chang, Y. Zhao, S. Zhao, A. Damgaard, and T.H. Christensen. Review of inventory data for the thermal treatment of sewage sludge. *Waste Management*, 146:106–118, 2022.

[120] Q. Song, X. Wang, W. Zhang, B. Qian, Y. Ye, K. Xu, and X. Wang. Digital twin technology for sewage sludge smoldering process and CO/NOx emissions based on back propagation neural network: A laboratory experimental study. *Process Safety and Environmental Protection*, 191, Part B:1883–1895, 2024.

[121] A. Loppinet-Serani, C. Aymonier, and F. Cansell. Current and foreseeable applications of supercritical water for energy and the environment. *ChemSusChem: Chemistry & Sustainability Energy & Materials*, 1(6):486–503, 2008.

[122] P.C.A. Bergman and J.H.A. Kiel. Torrefaction for biomass upgrading. In *Proc. 14th European Biomass Conference, Paris, France*, volume 2005, pages 17–21. sn, 2005.

[123] D.L. Klass. *Biomass for renewable energy, fuels, and chemicals*. Elsevier, 1998.

[124] T. Milne. Pyrolysis: the thermal behaviour of biomass below 600 C (Chapter 5). *Encyclopedia of Biomass Thermal Conversion, 3rd ed. Biomass Energy Foundation Press, pp. II–96–131*, 2002.

[125] P. Basu. *Biomass gasification, pyrolysis and torrefaction: practical design and theory.* Academic press, 2018.

[126] K. Chandolias, T. Richards, and M.J. Taherzadeh. Combined gasification-fermentation process in waste biorefinery. In *Waste Biorefinery*, pages 157–200. Elsevier, 2018.

[127] M. Materazzi, P. Lettieri, L. Mazzei, R. Taylor, and C. Chapman. Thermodynamic modelling and evaluation of a two-stage thermal process for waste gasification. *Fuel*, 108:356–369, 2013.

[128] L. Carlos. *High temperature air/steam gasification of biomass in an updraft fixed batch type gasifier.* PhD thesis, Royal Institute of Technology, Energy Furnace and Technology, 2005.

[129] L. Helsen and A. Bosmans. Waste-to-energy through thermochemical processes: matching waste with process. In *Proceedings of the 1st International Academic Symposium on Enhanced Landfill Mining*, pages 133–180. Haletra; Houthalen-Helchteren, 2010.

[130] F. Kirnbauer, V. Wilk, H. Kitzler, S. Kern, and H. Hofbauer. The positive effects of bed material coating on tar reduction in a dual fluidized bed gasifier. *Fuel*, 95: 553–562, 2012.

[131] A. Molino, S. Chianese, and D. Musmarra. Biomass gasification technology: The state of the art overview. *Journal of Energy Chemistry*, 25(1):10–25, 2016.

[132] A. Molino, P. Iovane, A. Donatelli, G. Braccio, S. Chianese, and D. Musmarra. Steam gasification of refuse-derived fuel in a rotary kiln pilot plant: Experimental tests. *Chemical Engineering Transactions*, 32, 2013.

[133] Y. Chhiti, M. Peyrot, and S. Salvador. Soot formation and oxidation during bio-oil gasification: experiments and modeling. *Journal of Energy Chemistry*, 22(5):701–709, 2013.

[134] T.K. Patra and P.N. Sheth. Biomass gasification models for downdraft gasifier: A state-of-the-art review. *Renewable and Sustainable Energy Reviews*, 50:583–593, 2015.

[135] J.A. Ruiz, M.C. Juárez, M.P. Morales, P. Muñoz, and M.A. Mendívil. Biomass gasification for electricity generation: Review of current technology barriers. *Renewable and Sustainable Energy Reviews*, 18:174–183, 2013.

[136] A.A.P. Susastriawan, H. Saptoadi, and Purnomo. Small-scale downdraft gasifiers for biomass gasification: A review. *Renewable and Sustainable Energy Reviews*, 76: 989–1003, 2017.

[137] M. Puig-Arnavat, J.C. Bruno, and A. Coronas. Review and analysis of biomass gasification models. *Renewable and sustainable energy reviews*, 14(9):2841–2851, 2010.

[138] N.J. Vickers. Animal communication: when i'm calling you, will you answer too? *Current biology*, 27(14):R713–R715, 2017.

[139] A. Zachl, M. Buchmayr, J. Gruber, A. Anca-Couce, R. Scharler, and C. Hochenauer. Evaluation and extension of the load and fuel flexibility limits of a stratified downdraft gasifier. *Energy*, 239:122279, 2022.

[140] R. Saidur, E.A. Abdelaziz, A. Demirbas, M.S. Hossain, and S. Mekhilef. A review on biomass as a fuel for boilers. *Renewable and sustainable energy reviews*, 15(5): 2262–2289, 2011.

[141] S. Ghorbani, K. Atashkari, and M. Borji. Three-stage model-based evaluation of a downdraft biomass gasifier. *Renewable Energy*, 2022.

[142] A.E. Pütün, E. Önal, B.B. Uzun, and N. Özbay. Comparison between the "slow" and "fast" pyrolysis of tobacco residue. *Industrial Crops and Products*, 26(3):307–314, 2007.

[143] A.V. Bridgwater and G.V.C. Peacocke. Fast pyrolysis processes for biomass. *Renewable and sustainable energy reviews*, 4(1):1–73, 2000.

[144] M. Zolezzi, C. Nicolella, S. Ferrara, C. Iacobucci, and M. Rovatti. Conventional and fast pyrolysis of automobile shredder residues (asr). *Waste Management*, 24(7): 691–699, 2004.

[145] L. Fagbemi, L. Khezami, and R. Capart. Pyrolysis products from different biomasses: application to the thermal cracking of tar. *Applied energy*, 69(4):293–306, 2001.

[146] P. Kazimierski and D. Kardaś. Influence of temperature on composition of wood pyrolysis products. *Wood Industry/Drvna Industrija*, 68(4), 2017.

[147] M. Amutio, G. Lopez, M. Artetxe, G. Elordi, M. Olazar, and J. Bilbao. Influence of temperature on biomass pyrolysis in a conical spouted bed reactor. *Resources, Conservation and Recycling*, 59:23–31, 2012.

[148] A.V. Bridgwater, D. Meier, and D. Radlein. An overview of fast pyrolysis of biomass. *Organic geochemistry*, 30(12):1479–1493, 1999.

[149] A.V. Bridgwater. Principles and practice of biomass fast pyrolysis processes for liquids. *Journal of analytical and applied pyrolysis*, 51(1-2):3–22, 1999.

[150] R. Zakrzewski. Niektore aspekty termicznego rozkladu drewna i wybranych surowcow lignocelulozowych. *Roczniki Akademii Rolniczej w Poznaniu. Rozprawy Naukowe*, (324):1–109, 2001.

[151] A. Demirbaş. Mechanisms of liquefaction and pyrolysis reactions of biomass. *Energy Conversion and Management*, 41(6):633–646, 2000.

[152] A. Gani and I. Naruse. Effect of cellulose and lignin content on pyrolysis and combustion characteristics for several types of biomass. *Renewable Energy*, 32(4):649–661, 2007.

[153] H. Yang, R. Yan, H. Chen, D.H. Lee, and C. Zheng. Characteristics of hemicellulose, cellulose and lignin pyrolysis. *Fuel*, 86(12-13):1781–1788, 2007.

[154] H. Hofbauer and M. Materazzi. Waste gasification processes for SNG production. In *Substitute natural gas from waste*, pages 105–160. Elsevier, 2019.

[155] E. Catalanotti, R.T.J. Porter, M.M. Chalchooghi, and H. Mahgerefteh. Biomass gasification in a downdraft gasifier with in-situ co2 capture: A pyrolysis, oxidation and reduction staged model. *Chemical Engineering Transactions*, 80:85–90, 2020.

[156] J. Kluska. *Analysis and dynamics of physicochemical processes in a downdraft gasifier*. PhD thesis, Institute of Fluid-Flow Machinery PASci, in Polish, Gdańsk, 2013.

[157] B. Adibimanesh, S. Polesek-Karczewska, and I. Wardach-Święcicka. Dynamics of biomass conversion in a fixed bed — A comparison of different simulation methods based on the Eulerian–Lagrangian approach. *Renewable Energy*, 256:123967, 2026.

[158] S. Polesek-Karczewska and D. Kardaś. Prediction of thermal behavior of pyrolyzed wet biomass by means of model with inner wood structure. *Journal of Thermal Science*, 24(1):82–89, 2015.

[159] S. Polesek-Karczewska. Modeling of phenomena in thermal conversion processes of solid fuels. In *Scientific Journals of the Institute of Fluid-Flow Machinery PASci, Gdańsk, (in Polish)*. 2018.

[160] M. Kaviany. *Principles of heat transfer in porous media*. Springer Science & Business Media, 2012.

[161] D. Kardaś, P. Hercel, S. Polesek-Karczewska, and I. Wardach-Święcicka. Novel insight into biomass pyrolysis. the process analysis by identifying timescales of heat diffusion, heating rate and reaction rate. *Energy*, 189:116159, 2019.

[162] D. Kardaś, J. Kluska, and S. Polesek-Karczewska. *Introduction to biomass gasification, IFFM Publishers, Gdańsk*. (in Polish), 2014.

[163] S. Polesek-Karczewska. Estimation of the structure-related share of radiation heat transfer in a carbonised packed coal bed. *Fuel*, 195:243–252, 2017.

[164] H.K. Versteeg and W. Malalasekera. *An introduction to computational fluid dynamics: the finite volume method*. Pearson education, 2007.

[165] W. Simpson and A. TenWolde. Wood handbook: Wood as an engineering material. *Gen. Tech. Rep. FPL–GTR–113, Madison, WI: US Department of Agriculture, Forest Service. Forest Products Laboratory*, 1999.

[166] D.L. Pyle and C.A. Zaror. Heat transfer and kinetics in the low temperature pyrolysis of solids. *Chemical Engineering Science*, 39(1):147–158, 1984.

[167] M. Marek. Numerical modeling of random packed beds of various packing densities with a sequential deposition algorithm. In *AIP Conference Proceedings*, volume 2078. AIP Publishing, 2019.

[168] B. Peters, M. Baniasadi, M. Baniasadi, X. Besseron, A. Estupinan Donoso, M. Mohseni, and G. Pozzetti. XDEM multi-physics and multi-scale simulation technology: Review of DEM–CFD coupling, methodology and engineering applications. *Particuology*, 44:176–193, 2019.

[169] M. Baniasadi, M. Baniasadi, and B. Peters. Coupled CFD-DEM with heat and mass transfer to investigate the melting of a granular packed bed. *Chemical Engineering Science*, 178:36–45, 2018.

[170] J. Wu, L. Li, Z. Yin, Z. Li, T. Wang, Y. Tan, and D. Tan. Mass transfer mechanism of multiphase shear flows and interphase optimization solving method. *Energy*, 292: 130475, 2024.

[171] LuXDEM Research Team. Xdem tutorials. unpublished materials. *University of Luxembourg, Campus Belval, Esch-sur-Alzette, Luxembourg*.

[172] F. Bagherzadeh, M.-J. Mehrani, M. Basirifard, and J. Roostaei. Comparative study on total nitrogen prediction in wastewater treatment plant and effect of various feature selection methods on machine learning algorithms performance. *Journal of Water Process Engineering*, 41:102033, 2021.

[173] A. Natekin and A. Knoll. Gradient boosting machines, a tutorial. *Frontiers in neurorobotics*, 7:21, 2013.

[174] V. Vapnik. *The nature of statistical learning theory*. Springer science & business media, 1999.

[175] W. Zhao, J.K. Liu, and Y.Y. Chen. Material behavior modeling with multi-output support vector regression. *Applied Mathematical Modelling*, 39(17):5216–5229, 2015.

[176] M. Wang and H. Chen. Chaotic multi-swarm whale optimizer boosted support vector machine for medical diagnosis. *Applied Soft Computing*, 88:105946, 2020.

[177] Ü. Ağbulut. Forecasting of transportation-related energy demand and co2 emissions in turkey with different machine learning algorithms. *Sustainable Production and Consumption*, 29:141–157, 2022.

[178] J. Park, C.H. Chan Lee, K.H. Cho, S. Hong, Y.M. Kim, and Y. Park. Modeling trihalomethanes concentrations in water treatment plants using machine learning techniques. *Desalin. Water Treat.*, 111:125–133, 2018.

[179] H. Sun, H. Bi, C. Jiang, Z. Ni, J. Tian, W. Zhou, Z. Qiu, and Q. Lin. Experimental study of the co-pyrolysis of sewage sludge and wet waste via TG-FTIR-GC and artificial neural network model: Synergistic effect, pyrolysis kinetics and gas products. *Renewable Energy*, 184:1–14, 2022.

[180] T. Wang and J. Knap. Stochastic gradient descent for semilinear elliptic equations with uncertainties. *Journal of Computational Physics*, 426:109945, 2021.

[181] K.P. Murphy. *Probabilistic machine learning: an introduction*. MIT press, 2022.

[182] Urszula Stańczyk and Lakhmi C Jain. *Feature selection for data and pattern recognition*. Springer, 2015.

[183] EU. Directive 2000/76/EC of the European Parliament and of the Council of 4 December 2000 on the incineration of waste. Official Journal L 332 of 28.12.2000.

[184] EU. Best Available Techniques (BAT). Reference Document for Waste Incineration. Industrial Emissions Directive 2010/75/EU (Integrated Pollution Prevention and Control). EU JRC Science for Policy Report.

[185] REFPROP, NIST Standard Reference Database 23, DLL ver. 10.0, 2018.

[186] S.L. Brunton, B.R. Noack, and P. Koumoutsakos. Machine learning for fluid mechanics. *Annual Review of Fluid Mechanics*, 52:477–508, 2020.

[187] S. Li, E. Kaiser, S. Laima, H. Li, S.L. Brunton, and J.N. Kutz. Discovering time-varying aerodynamics of a prototype bridge by sparse identification of nonlinear dynamical systems. *Physical Review E*, 100(2):022220, 2019.

[188] C. Lejeune, J. Mothe, A. Soubki, and O. Teste. Data driven discovery of systems of ordinary differential equations using nonconvex multitask learning. *Machine Learning*, pages 1–27, 2023.

[189] Cambridge University Press. Steam enthalpy, Year of publication. URL `https://www.cambridge.org/br/files/9813/6697/5550/Appendix_B.pdf`. Accessed on Date accessed.

[190] F. Neuwahl, G. Cusano, J. Gomez Benavides, S. Holbrook, and S. Roudier. Best Available Techniques (BAT). Reference Document for Waste Incineration, 2019. URL `https://eippcb.jrc.ec.europa.eu/sites/default/files/2020-01/JRC118637_WI_Bref_2019_published_0.pdf`.

List of Figures

List of Tables